



Department of Computer Science and Engineering

„Development of rapid and real-time detection of pathogenic
E. coli bacteria using microcavity in-line Mach-Zehnder
interferometer (μ IMZI)”

by

Monika Janik

Thesis submitted as partial fulfillment of the requirements for the degree of
Doctor of Philosophy in Science and Information Technology

June 2019

EVALUATION COMMITTEE

Supervisor: **Prof. Wojtek J. Bock**, Department of Computer Science and Engineering; Photonics Research Center, UQO

Co-supervisor: **DSc. Ewa Brzozowska**, Ludwig Hirsfeld Institute of Immunology and Experimental Therapy, Polish Academy of Science

President of the committee: **Prof. Kamel Adi**, Department of Computer Science and Engineering, UQO

Internal member of the committee: **Prof. Tinko Eftimov**, Department of Computer Science and Engineering; Photonics Research Center, UQO

External member of the committee: **Dr. Stephen Mihailov**, National Research Council Canada

ACKNOWLEDGMENTS

This Ph. D. studies were truly life-changing time for me. It is hard to describe how grateful I am for the past four years. For all the people I have met and for all the people who are still by my side, regardless of the distance. For the experience that I have gained and the person I have become.

I would like to start by thanking my supervisors, Prof. Wojtek Bock and Dr. Ewa Brzozowska. Without you, I would not be here. Thank you for giving me the chance to be a part of the PRC group and for trusting me with such a multidisciplinary project.

Next, special thanks to my incredible mentors Dr. Marcin Koba and Prof. Mateusz Śmietana. Thank you for your support and help whenever I needed it. For introducing me to the fs laser, what completely changed my Ph. D. For your advice, constant motivation and the confidence that I have gained in a completely new field.

To Prof. Tinko Eftimov, for making me understand my field even better, for explanations of problems during our experiments and insightful discussions.

To Prof. Kamel Adi and Dr. Stephen Mihailov for your help during evaluation process, time, and comments on my research project.

To Predrag Mikulic – my Canadian father. Thank you for being there for me every single day of my journey.

To Dr. Anna Celebańska, for every experiment that we have made together, for every brainstorm but most importantly, for being my best friend.

To my family, for your questions: „Do you really need this?” „Why so far?” which made me want to do this even more! Thank you for accepting and supporting my crazy ideas so far from home.

Last but not least, to my boyfriend and friends. Thank you for your love, patience and constant support. Thank you for every single call and for making me feel that everything is possible.

ABSTRACT

Often, an early and accurate diagnosis plays a decisive role in effective treatment. Especially at the point, where an immediate decision needs to be made, such as in complex cases of, for example, sepsis. Thus, detection of target biomolecules like bacteria has attracted attention lately, mainly when label-free techniques are involved, as they can be much faster and cost-effective than label-based ones.

This Ph. D. thesis presents the first study to date on selective label-free biosensing with a microcavity in-line Mach-Zehnder interferometer (μ IMZI) induced in an optical fiber. The sensing structures were fabricated in a single-mode fiber by femtosecond laser micromachining. The fabrication process, optimization as well as the testing of the sensor are conducted and explained in this work.

To prepare the surface of the microcavity for further measurements, we applied a reactive ion etching (RIE). The RIE process aimed mainly on cleaning the microcavity and on preparing the device for further experiments. As an additional effect, the wettability of the device surface was improved, making the RI measurements faster and more repeatable.

In order to identify the response of the μ IMZI structures to a thin layers, such as biological film, and to better understand its mechanism, we deposited the Al_2O_3 films on the set of μ IMZIs using atomic layer deposition method. Thanks to this experiment we have found the device can be used for investigation of phenomena taking place at the surface, such as in case of specific label-free biosensing applications.

In contrast to other studies of this sensing scheme, where only the sensitivity to refractive index changes in the cavity was investigated, during this research, we used chemical surface treatment of the sensor to ensure detection specificity. Immobilized MS2 bacteriophages and aptamer peptides were applied as recognition elements specifically targeting live, pathogenic *E. coli* C3000 and O157:H7 bacteria, respectively. It is shown that the sensor allows for real-time monitoring of biological phenomena taking place on the surface of the microcavity. The developed biosensor with its ultrahigh refractive index sensitivity of over 15,000 nm/RIU was capable of detecting live

E. coli bacteria concentrations as low as 10 colony forming units (CFU)/mL in liquid volume as low as picoliters.

The μ IMZI sensor presents a new, innovative approach comparing to other, invented earlier fiber optical platforms. Due to a very precise fabrication, the device is small, highly reproducible, portable, and able to work outside the lab environment. The sensor can easily be integrated at large scale into portable lab-on-chips. This will pave the way of fiber optic sensors to point-of-care diagnostics and analysis of environmental samples like water and food in order to detect the presence of bacteria in a very short time.

RÉSUMÉ

Souvent, un diagnostic précoce et précis joue un rôle décisif dans le traitement efficace. Surtout à ce stade, où une décision immédiate doit être prise, comme dans les cas complexes de, par exemple, la septicémie. Ainsi, la détection des biomolécules cibles comme les bactéries a attiré l'attention dernièrement, principalement lorsque les techniques exemptes d'étiquettes sont impliquées, car elles peuvent être beaucoup plus rapides et rentables que celles basées sur les étiquettes.

Cette thèse de doctorat présente la première étude à ce jour sur la biodétection sélective sans étiquette avec un interféromètre en ligne de Mach-Zehnder (μ IMZI) de microcavité induit dans une fibre optique. Les structures de détection ont été fabriquées dans une fibre monomode par micro-usinage au laser femtoseconde. Le processus de fabrication, l'optimisation ainsi que les essais du capteur sont menées et expliqués dans ce travail.

Pour préparer la surface de la microcavité pour d'autres mesures, nous avons appliqué une gravure ionique réactive (RIE). Le processus RIE visait principalement à nettoyer la microcavité et à préparer le dispositif pour d'autres expériences. Comme effet supplémentaire, la mouillabilité de la surface de l'appareil a été améliorée, rendant les mesures RI plus rapides et plus reproductibles.

Afin d'identifier la réponse des structures μ IMZI à des couches minces, comme le film biologique, et de mieux comprendre son mécanisme, nous avons déposé les films Al_2O_3 sur l'ensemble de μ IMZIs en utilisant la méthode de déposition de couche atomique. Grâce à cette expérience, nous avons trouvé que l'appareil peut être utilisé pour l'investigation des phénomènes qui se déroulent à la surface, comme dans le cas d'applications spécifiques de biodétection sans étiquette.

Contrairement à d'autres études de ce schéma de détection, où seule la sensibilité aux changements de l'indice de réfraction dans la cavité a été étudiée, au cours de cette recherche, nous avons utilisé le traitement de surface chimique du capteur pour assurer la spécificité de détection. Des bactériophages et des peptides d'aptamère immobilisés MS2 ont été appliqués en tant qu'éléments de reconnaissance ciblant spécifiquement les bactéries *E. coli* C3000 et O157:H7 vivantes, pathogènes, respectivement. Il est démontré que le capteur permet une surveillance en temps réel des phénomènes biologiques qui se déroulent à la surface de la microcavité. Le biocapteur

développé avec sa sensibilité à l'indice de réfraction ultra-élevée de plus de 15 000 nm/RIU a été capable de détecter des concentrations de bactéries *E. coli* vivantes aussi basses que 10 unités formant des colonies (CFU)/mL dans le volume de liquide aussi faible que les picoliters.

Le capteur μ IMZI présente une nouvelle approche innovante comparée à d'autres plates-formes optiques de fibre antérieures inventées. Grâce à une fabrication très précise, l'appareil est petit, hautement reproductible, portable et capable de travailler en dehors de l'environnement de laboratoire. Le capteur peut facilement être intégré à grande échelle dans des Lab-on-Chips portables. Cela ouvrira la voie des capteurs à fibre optique au diagnostic de point de soins et à l'analyse des échantillons environnementaux comme l'eau et les aliments afin de détecter la présence de bactéries dans un temps très court.

Table of Contents

ABSTRACT	i
OBJECTIVES	1
STATE OF THE ART.....	3
2.1 IMPORTANCE OF THE RESEARCH	4
2.2 REVIEW OF AVAILABLE FIBER OPTIC SENSOR (FOS) PLATFORMS FOR BACTERIA DETECTION.....	6
2.2.1. SURFACE PLASMON RESONANCE (SPR) SENSORS.....	8
2.2.2. OPTICAL FIBER GRATINGS (OFGs).....	8
CHARACTERIZATION OF THE MICROCAVITY IN-LINE MACH-ZEHNDER INTERFEROMETER (μ IMZI)	12
3.1 FEMTOSECOND LASER TECHNOLOGY.....	13
3.2 REVIEW OF MICROCAVITY BASED SENSORS.....	15
3.3. PHYSICAL PROPERTIES OF THE INVESTIGATED μ IMZI	19
3.4. GENERAL THEORETICAL CONSIDERATIONS	21
3.5. REFRACTIVE INDEX SENSITIVITY OF THE μ IMZI.....	22
3.6. TEMPERATURE SENSITIVITY OF THE μ IMZI.....	27
3.7. CONCLUSIONS	28
CLEANING AND PREPARING THE μ IMZI FOR FURTHER FUNCTIONALIZATION	29
4.1. REACTIVE ION ETCHING OF THE SURFACE	31
4.2. CLEANING EFFECT OF SF_6/O_2 RIE	32
4.3. CLEANING EFFECT OF O_2 RIE	34
4.4. COMPARISON OF THE TWO PROCEDURES.	35
4.5. STABILITY AND DURABILITY OF THE PLASMA TREATMENT.....	37
4.6. COMPARISON OF RIE AND HF WET ETCHING EFFECTS.	39
4.7. CONCLUSIONS.....	40
DEVELOPMENT AND TESTING OF THE μ IMZI SMALL VOLUME LABEL-FREE BIOSENSING CONCEPT BY THIN Al_2O_3 FILM DEPOSITION	41
5.1. THIN-FILM LAYER DEPOSITION	42
5.2. EFFECT OF Al_2O_3 ETCHING.	43
5.3. THE INFLUENCE OF THE THICKNESS OF THE LAYER ON RI SENSITIVITY.	44
5.4. COMPARISON OF THIN-LAYER DEPOSITION EFFECT TO CONTROLLED MICROFABRICATION OF SHALLOWER CAVITIES.	45
5.5. THEORETICAL EXPLANATION OF THE THIN-LAYER EFFECT	46
5.6. CONCLUSIONS.....	47
LABEL-FREE DETECTION OF LIVE E. COLI BACTERIA USING THE μ IMZI	49

6.1. REVIEW OF BIORECEPTORS FOR BACTERIA DETECTION.....	50
6.1.1. ANTIBODIES	51
6.1.2. BACTERIOPHAGES	52
6.1.3. PHAGE RECEPTOR BINDING PROTEINS (ADHESINS)	53
6.1.4. APTAMERS.....	53
6.1.5. PHAGE DISPLAY PEPTIDE APTAMERS	54
6.1.6. CARBOHYDRATES AND LECTINS.....	55
6.2. LABEL-FREE DETECTION OF E. COLI C3000 BACTERIA WITH MS2 PHAGES.....	57
6.2.1. BACTERIA DRY-WEIGHT SENSING.	60
6.2.3. DETECTION OF LIVE E. COLI C3000.....	62
6.2.4. NEGATIVE CONTROLS.....	67
6.2.5. CONCLUSIONS.	68
6.3. LABEL-FREE DETECTION OF PATHOGENIC E. COLI O157:H7 BACTERIA WITH PEPTIDE APTAMERS	69
6.3.1. BIOPANNING OF E. COLI O157:H7 WITH PHAGE DISPLAY LIBRARY	71
6.3.2. IMMOBILIZATION OF THE PEPTIDES ON THE μ IMZI SURFACE	72
6.3.3. DETECTION OF PATHOGENIC HEAT-KILLED E. COLI O157:H7	75
6.2.5. PERFORMANCE EVALUATION OF MS2 PHAGES AND PEPTIDE APTAMERS WHEN APPLIED AS RECOGNITION ELEMENTS	80
6.2.6. NEGATIVE CONTROLS.....	81
6.2.7. CONCLUSIONS	83
CONCLUSIONS.....	84
FUTURE WORK	86
LITERATURE	87
APPENDIX A	97
Preparation of the bioreceptors	97
APPENDIX B.....	99
Preparations of bacteria	99
APPENDIX C	100
Functionalization of the μIMZI surface	100
AUTHOR’S PUBLICATIONS.....	101

LIST OF TABLES

TABLE 1

SELECTED MAJOR WATER AND FOODBORNE DISEASE OUTBREAKS CAUSED BY *E. COLI* O157:H7.. 5

TABLE 2

CHARACTERIZATION AND APPROXIMATE DIMENSIONS OF THE FOUR INVESTIGATED
STRUCTURES..... 18

TABLE 3

APPROXIMATE FREE SPECTRAL RANGES OF THE FOUR INVESTIGATED STRUCTURES..... 22

TABLE 4

COMPARISON OF PRESENTED BIORECOGNITION ELEMENTS (* depending on the type of
bacteriophage)..... 55

LIST OF FIGURES

Figure 1. Schematic representation of the fiber optic biosensor.....	6
Figure 2. Schematic drawing of the μ IMZI structure.....	15
Figure 3. Schematic drawing of the μ IMZI structure. The diameter of the micro-cavity is indicated by d and the depth by h	16
Figure 4. Scheme of the fs-laser based microfabrication setup.....	17
Figure 5. SEM visualization of one of the μ IMZI structures (structure shown here is described in the text as C).....	19
Figure 6. Profilometer scan through the μ IMZI structure.....	19
Figure 7. A comparison of results for microcavities with diameters $d = 30, 40, 54$ and $60 \mu\text{m}$ filled with water ($n = 1.3333$ RIU).....	21
Figure 8. A) Spectral response and B) sensitivity of the μ IMZI with diameter $d = 30 \mu\text{m}$ for aqueous solutions with n ranging from 1.33 to 1.38 RIU.....	23
Figure 9. A) Spectral response and B) sensitivity of the μ IMZI with diameter $d = 40 \mu\text{m}$ for aqueous solutions with n ranging from 1.33 to 1.38 RIU.....	23
Figure 10. A) Spectral response and B) sensitivity of the μ IMZI with diameter $d = 54 \mu\text{m}$ for aqueous solutions with n ranging from 1.33 to 1.38 RIU.....	23
Figure 11. A) Spectral response and B) sensitivity of the μ IMZI with diameter $d = 64 \mu\text{m}$ for aqueous solutions with n ranging from 1.33 to 1.38 RIU.....	23
Figure 12. Sensitivities of the investigated μ IMZI structures for different microcavity diameters.	25
Figure 13. Transmission spectra of μ IMZI at different H_2O temperatures in the cavity.....	26
Figure 14. Schematic representation of the μ IMZI and SiO_2/Si wafer placement in the RIE process chamber.....	30
Figure 15. The effect of five consecutive SF_6/O_2 RIE processes on the μ IMZI transmission spectrum. The measurements were made after filling the micro-cavity with water.....	31
Figure 16. Spectral response of the μ IMZI A) before and B) after all the SF_6/O_2 -based RIEs for solutions in the micro-cavity with RI ranging from 1.33 to 1.38 RIU.....	32
Figure 17. Sensitivities of the investigated μ IMZI structure before (S_{Before}) and after (S_{After}) all five SF_6/O_2 RIE processes.....	32
Figure 18. A) The effect on the μ IMZI transmission spectra of three RIE processes, two with O_2 and an additional one with SF_6/O_2 . The measurements were made after filling the micro-cavity with	

water. B) Influence of reactive gas on FWHM after each RIE process. The final etching of the O ₂ sample was done with SF ₆ /O ₂	33
Figure 19. Effect of O ₂ etching process on SiO ₂ surface properties: A) before (contact angle is equal to 64°) and B) after (contact angle is unmeasurable because of high wettability).....	37
Figure 20. Illustration of the effect of O ₂ and SF ₆ /O ₂ etching processes on SiO ₂ surface wettability for different storage times in normal conditions.....	38
Figure 21. The response of the μMZI to Al ₂ O ₃ film etching recorded for the water-filled cavity. The evolution of the transmission spectrum during the process in reference to the response before deposition.....	42
Figure 22. Effect of increase in RI of liquid in the micro-cavity for different thicknesses of the Al ₂ O ₃ film, where A) shows a spectral response at a selected stage of the etching experiment and B) gives a summary of the measurements with determined sensitivity at each stage of etching.....	44
Figure 23. Influence of the cavity depth (different amount of fs laser runs) on spectral response to RI, where A) shows initial spectra for cavity filled with water and B) shows wavelength shift of minima with RI. The diameter of the cavity was d = 50 μm.....	44
Figure 24. Schematic representation of the Gram-negative bacteria and their cell wall.....	50
Figure 25. A TEM image of pilus-associated MS2 phages. The long rod-shaped structure is the pilus. Length and thickness of pilus in this image were about 430 and 6 nm, respectively ¹ . Micrograph of an F-pilus emerging from an E. coli cell that is covered with icosahedral MS2 phage particles.....	57
Figure 26. The structure of the wild-type bacteriophage MS2 virion.....	57
Figure 27. Schematic representation of the μMZI biofunctionalization process.....	59
Figure 28. A) Transmission spectra of the μMZI at each stage of the experiment with <i>E. coli</i> C3000 (1 mg/mL) dry weight. The arrow indicates the change induced by bacteria binding. B) Transmission spectra of the μMZI with the cavity diameter d = 50 μm during the evolution of the Al ₂ O ₃ film thickness (initially t = 154 nm) with its etching process recorded for a water-filled cavity. The spectrum before the deposition was given for reference. Arrows indicate the shift of the minimum induced by each procedure.....	60
Figure 29. The response of the μMZI where the transmission spectra in PBS at each stage of the experiment with different concentrations of live <i>E. coli</i> C3000 bacteria after incubation and extensive washing.....	62
Figure 30. The response of the μMZI where A) shows a correlation between the transmission and the wavelength B) shows a linear combination between the transmission and the wavelength...	63
Figure 31. A shift of the minimum's wavelength at each stage of the experiment induced by functionalization and incubation in different concentrations of live bacteria.....	64

Figure 32. Transmission spectra of the μ IMZI at each of the stage of the experiment, showing the response A) for positive <i>E. coli</i> C3000 without phages on the sensor's surface and B) for negative <i>B. Thailandensis</i> with MS2 phages.....	65
Figure 33. Whole cell-based panning protocol.....	69
Figure 34. Sequences and 3D models of synthesized peptides.....	70
Figure 35. The response of the μ IMZI where the transmission spectra in PBS at each stage of the surface functionalization process after incubation and extensive washing.....	71
Figure 36. Photos of the water droplet deposited on the glass surface: before cleaning and after 30 min and 2 h silanization processes.....	72
Figure 37. Summary of the most relevant cellular events that occur in a vegetative bacterial cell upon exposure to heat.....	73
Figure 38. The response of the μ IMZI at each stage of the experiment with PEP-1 and different concentrations of heat-killed <i>E. coli</i> O157:H7 bacteria where A) shows the transmission spectra in PBS after incubation and extensive washing and B) shows a correlation between the transmission and the wavelength.....	75
Figure 39. The response of the μ IMZI at each stage of the experiment with PEP-2 and different concentrations of heat-killed <i>E. coli</i> O157:H7 bacteria where A) shows the transmission spectra in PBS after incubation and extensive washing and B) shows a correlation between the transmission and the wavelength.....	76
Figure 40. The response of the μ IMZI at each stage of the experiment with PEP-MIX and different concentrations of heat-killed <i>E. coli</i> O157:H7 bacteria where A) shows the transmission spectra in PBS after incubation and extensive washing and B) shows a correlation between the transmission and the wavelength.....	76
Figure 41. The juxtaposition of spectral shifts after each concentration of heat-killed <i>E. coli</i> O157:H7 bacteria for two separate peptides (PEP-1 and PEP-2) as well as for their combinations (PEP-MIX).....	77
Figure 42. A shift of the minimum's wavelength at each stage of the experiment induced by functionalization and incubation in different concentrations of heat-killed bacteria.....	78
Figure 43. Transmission spectra of the μ IMZI at each of the stage of the experiment, showing the response A) for positive <i>E. coli</i> O157:H7 without peptides on the sensor's surface and B) for negative <i>B. Thailandensis</i> with PEP-MIX.....	80

LIST OF SYMBOLS AND ABBREVIATIONS

Ab	Antibody
ALD	Atomic layer deposition
BSA	Bovine serum albumin
CA	Contact angle
CDC	Center for Diseases Control and Prevention
CFU	Colony Forming Unit
d	diameter
DNA	Deoxyribonucleic acid
DTP	Dispersion Turning Point
E. coli	Escherichia coli
EHEC	Enterohemorrhagic E. coli
FBG	Fiber Bragg Grating
FDA	the Food and Drug Administration
FOS	Fiber Optic Sensors
FO-SPR	Fiber-optic Surface Plasmon Resonance
FPI	Fabry-Perrot interferometer
Fs	Femtosecond
FSR	Free Spectral Range
FWHM	Full width at half maximum
G-	Gram-negative
h	height
Ig	Immunoglobulin
LMR	Lossy Mode Resonance
LOD	Limit of Detection
LPG	Long Period Grating
LPS	Lipopolysaccharide

MFD	Mode field diameter
MI	Michelson interferometer
NA	Numerical Aperture
OD ₆₀₀	Optical density
OMP	Outer Membrane Protein
PC	Photonic Crystals
PFU	Plaques Forming Unit
RBP	Receptor Binding Protein
R&D	Research and Development
RF	Radio Frequency
RI	Refractive Index
RIE	Reactive ion etching
RNA	Ribonucleic acid
Rpm	Rotations per minute
SELEX	Systematic Evolution of Ligands by EXponential enrichment
SEM	Scanning Electron Microscope
SiO ₂ /Si	Silicon dioxide/Silicone
SMF	Single Mode Fiber
SPR	Surface Plasmon Resonance
TEM	Transmission Electron Microscope
WHO	World Health Organization
UV	Ultraviolet
μIMZI	Microcavity in-line Mach-Zehnder interferometer
λ _c	Cut-off wavelength

LIST OF CHEMICALS

Al ₂ O ₃	Aluminum oxide
APTES	(3-Aminopropyl) triethoxysilane
BSA	Bovine serum albumine
CHCl ₃	Chloroform
EDC	N-(3-Dimethylaminopropyl)-N'-ethylcarbodiimide hydrochloride
GLU	Glutaraldehyde
GLY	Glycine
HCl	Hydrochloric acid
IPTG	Isopropyl β-D-1-thiogalactopyranoside
LB	Laura Bretani
MeOH	Methanol
NaCl	Sodium chloride
NaOH	Sodium hydroxide
O ₂	Oxygen
PBS	Phosphate-buffer saline
PEG	Polyethylene glycol
H ₂ SO ₄	Sulfuric acid
SF ₆	Sulfur Hexafluoride
TMA, Al(CH ₃) ₃	trimethylaluminum
TRIS	Tris(hydroxymethyl)aminomethane
TWEEN 20	Polyethylene glycol sorbitan monolaurate
Xgal	5-bromo-4-chloro-3-indolyl-β-D-galactopyranoside

CHAPTER 1

OBJECTIVES

Based on our recent discoveries²⁻⁶ and the unique advantages of fiber-optic sensors (FOS), the primary objective of this work is to study, develop and test a novel and improved security system for rapid, specific, direct and sensitive bacteria detection. The scope of the studies presented here is highly multidisciplinary. Therefore, to address a variety of issues, the work will have two different aspects, namely: optical and biological.

First one includes developing a novel concept and theoretical studies of the fiber optic sensor, which will present new, innovative features compared to other fiber-optic sensing platforms invented to date. The challenges in developing any sensor system are numerous, namely, selectivity, sensitivity, stability, or suitability for field operation. Therefore, the work will cover all the above issues and will overcome limitations of existing technology creating fast, simple, and cost-effective sensor.

To propose a novel device for pathogen detection via its interaction with the surrounding environment, the sensor's surface must be specifically modified. Thus, the biological aspect of the work will be research on a new bioreceptor and the way to immobilize it on a sensor's surface allowing for specific bacteria cell detection.

To successfully achieve the main objectives, the specific aims are as follows:

The first step towards achieving a specific biosensor is the development and testing of a new, miniaturized fiber-optic sensing device.

Next step includes cleaning and hydrophilization of the optical fiber's surface to make further measurements easier to perform and more repeatable.

Once a surface is prepared, the ability to label-free detection using a chosen device will be verified using thin-film layer deposition.

The fourth step covers surface functionalization. An appropriate functionalization using phages and peptide aptamers will allow detecting the pathogenic *E. coli* bacteria. Well-adjusted bioreceptor will eliminate the risk of false positive output in complex environments and will give accurate and reliable results.

Details of the device fabrication, preparation, and functionalization process, as well as results of the real-time detection and the theoretical formulation of the spectral shifts are given in details in the subsequent chapters.

CHAPTER 2

STATE OF THE ART

Chapter 2 presents state of the art including the importance of the research following by an overview of the numerous biosensing techniques that have been developed and used so far. Next, a review of the available fiber optic sensors for bacteria detection is given. The main applications of these techniques along with their advantages and limitations are also described.

2.1 IMPORTANCE OF THE RESEARCH

Escherichia coli is a very versatile microorganism. Some strains are important, harmless members of the healthy intestinal microflora of humans and animals. However, several *E. coli* clones have acquired specific virulence factors allow them to cause a broad spectrum of intestinal and extraintestinal diseases^{7,8}. Among them, Enterohemorrhagic (EHEC) *E. coli* O157:H7 is a major cause of several million infections worldwide each year. They are ubiquitous, and their presence in natural sources such as water and food (both natural and packed) is unavoidable. Consumption of contaminated products is the primary cause of microbial mediated infection in both developed & developing countries. In North America, Europe, The United Kingdom, Japan and other areas of the world, EHEC O157:H7 are most common infections, which are fatal to both children (3–10%) and elders (up to 50%).

Considering extremely low infectious dose (~ 100 cells), EHEC has also caused outbreaks associated with person-to-person transmission, petting zoo or farm visitations, recreational water, or even airborne transmission in a contaminated building^{9,10}. The incidence of EHEC in humans is difficult to determine, because cases of uncomplicated diarrhea may not be tested for these organisms. Center for Diseases Control and Prevention (CDC) estimated that EHEC O157:H7 causes approximately 73,000 illnesses, 2,000 hospitalizations, and 50-60 deaths each year. What was reported¹¹, the annual cost of illness due to *E. coli* O157:H7 infections is equal to 405 million dollars including medical care, lost of productivity and premature death.

Despite regulatory efforts to improve the safety of the food and water supplies *E. coli* O157:H7 outbreaks remain common. Just recently, in April 2018 CDC, public health and regulatory officials in several states, and the Food and Drug Administration (FDA) reported a multistate outbreak of *E. coli* O157:H7 infections. 197 people infected have been recorded from 35 states (USA), and 4 provinces (CA). 89 people have been hospitalized, including 26 people who have developed a type of kidney failure (hemolytic uremic syndrome), and 5 people died. Table 1 presents selected water and foodborne outbreaks caused by *E. coli* O157:H7.

Table 1 Selected major water and foodborne disease outbreaks caused by *E. coli* O157:H7^{12–14}.

Year	Country	Cases	Deaths	Source
1990	US	243	4	drinking water
1991	CA	521	2	beef
1992-1993	US	700	3	beef
1995	Scotland	633	0	drinking water
1996	Japan	12,680	12	radish sprouts
1996	Scotland	503	20	lunch food
1996-1997	Scotland	512	17	beef
1997	UK	332	0	beef
1999	US	1,000	2	drinking water
1999	US	329	0	beef
2000	CA	2,300	7	drinking water
2000	US	788	1	beef
2006	US/CA	204	3	spinach
2007-2008	Finland	1,000	0	drinking water
2014	CA	119	0	pork
2016	UK	158	2	salad
2018	US/CA	197	5	lettuce

Currently, bacteria detection still relies on classical microbiology methods including isolation and bacteria growth in selective media. These techniques are proven to be effective, but they require high technical skills and are time-consuming (up to 48 hours) due to the slow process of microorganism culturing. Although R&D into fiber-optic biosensors has made substantial progress during the last years, current methods of detecting bacteria are still insufficient and inadequate. Thus, accurate, fast, sensitive, precise, and direct detection techniques are crucial to achieving early recognition of such dangerous pathogens to prevent the spread of disease and find appropriate treatments as soon as possible.

2.2 REVIEW OF AVAILABLE FIBER OPTIC SENSOR (FOS) PLATFORMS FOR BACTERIA DETECTION

Often, an early and accurate diagnosis plays a decisive role for an effective treatment. Especially at the point, where an immediate decision needs to be made, such as in complex cases of, for example, sepsis¹⁵. Nowadays, the research trend in the biochemical sensors' field focuses mainly on the development of highly sensitive, selective, and fast platforms. A new device for bacteria detection is expected to offer high performance, multiplexing capability along with low system complexity. It should also provide high flexibility, low cost of fabrication, minimal sample consumption, and avoid possible cross-sensitivity with environmental factors. To cover the requirements, academic research, and product development have made a tremendous contribution in the field of biosensing during the last years.

In a typical biosensing system which converts the molecular interaction into a specific signal, the binding events can be detected without the necessity of adding any label probe. Fig. 1 illustrates a schematic representation of the fiber-based biosensor.

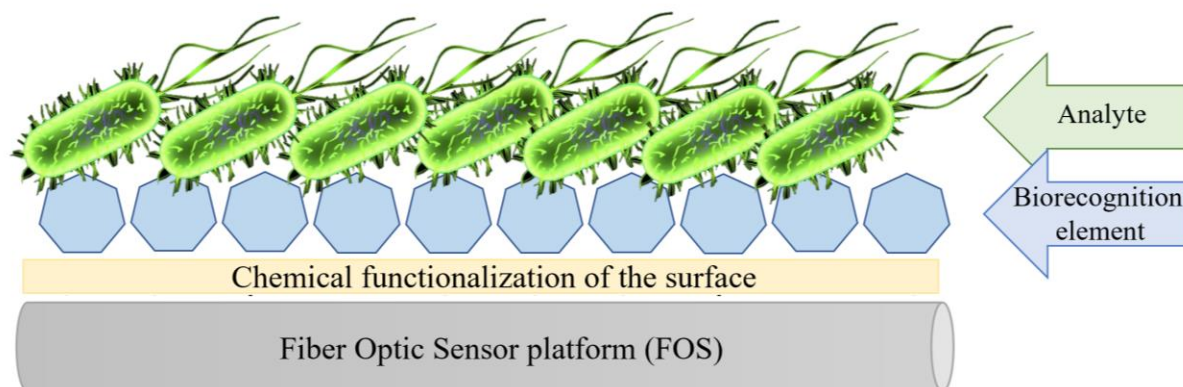


Figure 1. Schematic representation of the fiber optic biosensor

Based on Fig. 1 we can assume that each biosensing device requires the following components:

- 1) Firstly, a proper device and method for detecting and quantifying the binding events
- 2) Secondly, a component – biorecognition element, which will be immobilized on the device's surface and will selectively recognize the target of interest.

3) Thirdly, the transducing layer – chemical functionalization – which will keep the receptor close to the sensor surface. The close placement of the bioreceptor facilitates converting the biochemical binding events happening on the surface into an easily measurable signal such as a change in mass, density, or a change in optical properties like a refractive index.

In contrast to label-based methods, label-free protocol enables detection of the target molecules straight from the patient/environmental sample. Hence, it is usually cheaper, faster and easier to perform. Another advantage of this technique is the capability of tracking the ligand in the real-time and acquiring direct information about the molecule, including quantitative determination.

Optical fiber sensors are being increasingly proposed for label-free biosensing, as promising alternatives to the traditional ones using Surface Plasmon Resonance (SPR). During the last decade, the growing request in practical applications pushed the technology behind the fiber-optic sensors over its limits by means of developing high-performance and low-detection limit devices.

Although the fiber-optic devices have been demonstrated to offer comparable performance concerning traditional optical platforms, with their intrinsic benefits like:

- immunity to electromagnetic interference,
- the possibility of multiplexing,
- high resistance to harsh environmental conditions,
- the capability of remote measurement,
- high compatibility with optoelectronic devices,
- low power consumption,
- resistance to a number of chemicals,
- long-term reliability.

they are gaining an advantage over other reported devices. Excellent reviews were presented on this topic during the last years, including the ones by Wang and Wolfbeis¹⁶, and recently by Chiavaioli et al.¹⁷. According to them, the most popular optical fiber devices for biosensing are the Long-Period Gratings (LPGs), and the etched, side-polished or tilted Fiber Bragg Gratings (FBGs). Moreover, Lossy Mode Resonance (LMR) and fiber-optic SPR (FO-SPR) have demonstrated great potential in biosensing as well. The technology behind the platforms above is very mature, as evidenced by the number of numerical and experimental studies carried out in the last decades.

2.2.1. SURFACE PLASMON RESONANCE (SPR) SENSORS

Among many optical platforms, the surface plasmon resonance (SPR) based sensors have always received much attention due to their superior sensitivity, which is necessary for highly accurate bio-measurements^{18,19}. Coupling SPR to optical fiber technology has brought further tremendous advancements in the field by offering attractive advantages over the traditional prism-based SPR platforms, such as simplicity, cost-effectiveness, and miniaturization²⁰. However, drawbacks associated with the SPR based sensors still are numerous, such as the expensive and elaborated metal deposition procedures required to support the surface plasmon wave. In the case of fiber-SPR sensors, adhesion of the metal layer to the fiber is very crucial also, thereby often representing a major limiting factor, and the need for special surface treatment²¹. Moreover, a number of investigated liquids, including the buffer and bacteria solutions used in some experiments, may contain a certain amount of salt, which can accelerate corrosion of metal layer²². While some SPR systems have proven high sensitivity in detecting small targets such as proteins and viruses, these sensors have trouble detecting larger targets such as bacteria, since this requires greater penetration of the evanescent field into the analyte²³. This is why they often detect bacterial toxins instead of the whole microorganisms.

2.2.2. OPTICAL FIBER GRATINGS (OFGs)

Optical Fiber Gratings (OFGs) are diffraction structures that involve periodic modulations of the RI in the core of an optical fiber. Depending on the RI modulation period, OFGs can be classified as short-period gratings – called Fiber Bragg Gratings (FBG) – and as long-period gratings (LPG)²⁴. In both, under specific conditions, part of the optical field from the fiber core region (core mode) is redirected to the cladding region (the cladding mode) of the optical fiber. A small fraction

of the cladding mode field travels outside the optical fiber (evanescent field), interacting with the outer region. The sensing principle of the OFGs relies mainly on the evanescent field interactions at the boundary between the fiber and the surrounding medium. Thus, the resonance wavelength depends on the RI of the external environment, as well as on the thickness and on optical properties of the film/overlay formed on the OFGs surface. Due to its high RI sensitivity, OFG platforms can perform real-time monitoring of interactions between bio-molecules at the surface of the grating.

The RI sensitivity, which refers to label-free biosensing capabilities of the OFGs, may also be further improved and transformed. In the case of FBGs, etched, side-polished or tilted structures were introduced. While LPGs were modified by optimizing the working point of the device up to the dispersion turning point (DTP) of the cladding modes⁶ or/and by deposition of high RI nano-overlays²⁵. Although both types of the platform can be used for the label-free monitoring, the LPGs^{3,6} were employed for bacteria detection more often than FBGs.

What must be emphasized, the pioneer studies for using the LPG for *E. coli* detection were performed in Photonics Research Center at UQO. Our significant expertise in the area of photonic sensing systems for biochemical hazards and availability of unique technologies including femtosecond and excimer lasers enable us to develop, manufacture and optimize the LPG-based transducers for biosensing.

LPGs were tested throughout the years also for the detection of many other different bio-applications including bacterial toxins²⁶, nucleic acids²⁷, proteins²⁸, and triacylglycerides²⁹. Although such a device appeared effective and reached very low limits of detection, many challenges remain valid and urgent for the creation of the successful biosensing systems. Common limiting factors of the LPGs' are their capability for multiplexing or reproducibility. This type of sensor having 5 – 6 cm length of the fiber usually requires at least 500 μ L of the examined sample, which can be problematic when only small volumes of analyte are available. Most of the LPG sensors are also sensitive towards temperature, which is an essential disadvantage since temperature is one of the most disrupting factors in RI measurements.

Despite generally good performance achieved using the aforementioned fiber-optic devices, there are still drawbacks and open questions about most precise and reliable detection. Identification of

small molecules in pL volumes – possibly up to single molecule – undisturbed by external factors, along with miniaturization of the device is still a challenge. Therefore, the constant attention is paid to developing new, cutting-edge devices which will be capable of solving these challenges.

THE OPTICAL PART

CHAPTER 3

CHARACTERIZATION OF THE MICROCAVITY IN-LINE MACH-ZEHNDER INTERFEROMETER (μ IMZI)

Chapter 3 is devoted to the realization of the first objective of the thesis – development, and characterization of the μ IMZI device. The first part of the chapter gives an overview of microcavity-based sensors and their working mechanism. Next, femtosecond laser technology and our optimized microfabrication process are detailed along with the optical characterization setup used to carry out the experiments. Then, we present the results of the micromachining process such as physical properties of the fabricated μ IMZIs, RI sensitivity, followed by the discussion on the influence of the microcavity size on its RI sensitivity. Last part of the chapter covers the temperature sensitivity of the μ IMZI.

The work described in this section was partially presented in:

1. M. Janik, A. K. Myśliwiec, M. Koba, A. Celebańska, W. J. Bock and M. Śmietana, “Sensitivity Pattern of Femtosecond Laser Micromachined and Plasma-Processed In-Fiber Mach-Zehnder Interferometers, as Applied to Small-Scale Refractive Index Sensing,” *IEEE Sens. J.* 17, 11, 3316-3322 (2017);
2. M. Janik, M. Koba, W. J. Bock, M. Śmietana, "Influence of the size of a micro-cavity fabricated in an optical fiber using the femtosecond laser in the form of in-line Mach-Zehnder interferometer on its refractive index sensitivity," Proc. SPIE 10175, Electron Technology Conference 2016, 101750P (2016).

3.1 FEMTOSECOND LASER TECHNOLOGY

The rapid development of femtosecond lasers over the last decades has opened up a wide range of new applications in industry, material science, and medicine³⁰. D. Du et al. first reported femtosecond laser micromachining in 1994, demonstrating ablation of microfeatures on silica and silver surface³¹. Since then, the fs laser system has been improved, gaining nanometer-scale precision.

One of the most common laser systems used for microstructures fabrication is the Ti: sapphire laser which uses a Ti-doped sapphire crystal as the gain medium. Thanks to its remarkable properties – very broad emission from 680 to 1080 nm, peaking at 800 nm, and very high thermal conductivity ($34 \text{ W K}^{-1}\text{m}^{-1}$) – Ti:Al₂O₃ was the perfect candidate to replace the femtosecond dye lasers. Described lasing medium generates the shortest pulses ever produced from a laser oscillator. Ti:Sapphire technology allows the production of very intense pulse generation up to the petawatt level, preserving the very high quality of the beam. In contrast to other tunable solid-state lasers, Ti:Al₂O₃ exhibits large pick cross-section ($3.8 \times 10^{-19} \text{ cm}^2$). Thanks to its simple $3d^1$ configuration, and entirely separated absorption and emission spectrum, there is no expected excited-state absorption or up-conversion. The hexagonal rhombohedric crystal structure of the Al₂O₃ matrix ensures high efficiency of the laser by increasing the population inversion and prevents the system from heat generation through non-radiative transitions³².

Femtosecond laser micromachining is a process by which laser pulses are employed to induce micrometer-size structures on the surface of the chosen material. During the laser-induced optical breakdown, the energy is transferred from an optical field to a material causing ionization of a large number of electrons which in turn transfer the energy to the lattice. As a result of the irradiation, localized, permanent structural modifications or damages can occur. The process by which a material absorbs energy from the laser and the mechanisms by which material respond are the key to understanding the laser micromachining.

In transparent to the laser wavelength samples, a single photon of light does not have enough energy to excite the electron from the valence to the conduction band. Thus the absorption of the laser energy can occur only through nonlinear processes. There are two classes of nonlinear excitation mechanisms, photoionization, and avalanche ionization^{33,34}.

Photoionization refers to direct excitation of the electron from the valence to the conduction band by the laser field. Depending on the laser frequency and intensity, we can distinguish the multiphoton ionization regime and the tunneling ionization regime. They were shown by Keldysh to be two limits of the same process, yet retaining very different conceptual pictures³⁵.

In tunneling ionization, the electric field of the laser suppresses the potential that binds a valence electron to its parent atom. If the electric field is strong enough, the electron tunnels out and becomes free. This regime dominates for strong laser fields and low frequency. At higher laser frequencies, photoionization occurs through the absorption of multiple photons by an electron. In this mechanism, the sum of energy of all the absorbed photons must be equal or greater than the bandgap energy. There are also situations when the photoionization is a mix between tunneling and multiphoton ionization^{33,34}.

Avalanche ionization involves free carrier absorption by an electron already in the conduction band followed by impact ionization. This electron sequentially absorbs several laser photons moving to higher energy states until its energy exceeds the conduction band minimum by more than the bandgap energy. Next, to conserve both energy and momentum collisionally ionizes another electron from the valence band, leaving two electrons at the conduction band minimum as a result. As long as the laser field is present, the process repeats, and the electron density in the conduction band grows exponentially.

It is worth to mention that avalanche ionization requires ‘seed’ electrons in the conduction band of the material. These are provided either by thermal excitation, by the easily ionized impurity of the material, or – as in case of femtosecond duration laser pulses – by carriers directly photoexcited. Such avalanche ionization produces a highly absorptive and dense plasma, facilitating the transfer of energy from the laser to the glass. At sufficiently high energy, this process causes non-thermal ionic motion leading to material removal with extremely precise edges. The ultrashort pulses deliver energy before the thermal diffusion occurs^{33,34}. Thus, it is possible to achieve a highly precise and efficient process without thermal degradation in the surrounding area. The damage to the material, as well as the quality of the micromachining strongly depends on the process parameters such as pulse duration and energy, repetition rate, and scanning speed. This is why

these parameters have to be highly optimized and well-adjusted to the processed material and the final application of the sample.

3.2 REVIEW OF MICROCAVITY BASED SENSORS

Thanks to the development of surface micromachining technology – *such as femtosecond laser processing* – novel approaches to sensing appears. One of the relatively new classes of sensing devices with a promise to become viable technologies are structures based on in-fiber microcavities³⁶. The presence of the microcavity with diameters in the order of tens of micrometers micromachined in the fiber is the defining feature of these platforms.

Although the microcavity-based platforms are known for almost a decade and have been reported by few groups in different shapes and for different applications³⁶, the subject of using the microcavity for specific biosensing has never been addressed or studied in the literature reported so far. For this reason, the results of this Ph. D. present cutting edge pioneer studies covering the above subject.

Considering novel and miniature design, superior sensitivity, unique feature to measure volumes as low as picoliters, temperature insensitivity, significant potential in bio- and chemosensing, and availability of the state-of-the-art microfabrication facility, a in-fiber microcavity structure was selected as a primary fiber-optic sensing platform in this work.

Many microchannels and microholes have been fabricated in optical fibers using fs laser micromachining³⁷. Some of them operate as in-line fiber interferometers such as Fabry-Perot^{38–41} or Michaelson interferometers⁴². The majority of the microcavities are fabricated in multistep processes that besides fs laser technology include hard to control wet etching (in hydrofluoric acid (HF) or other acids etchants)³⁸, as well as fusion splicing⁴³. Nevertheless, the obtained RI sensitivity of these devices rarely exceeds 1000 nm/RIU^{39,44}.

One of the reported configurations is also a microcavity in-line Mach-Zehnder interferometer (μ IMZI)⁴⁵. The structure is formed by a well-controlled fiber cladding and partially core ablation up to a hundred micrometers. The cavity splits incoming light into two beams, where one beam remains in the fiber core, while the other propagates through the cavity. The two beams interfere

at the far side wall of the cavity (Figure 2). The optical properties of these devices are determined mostly by the size, shape, and position of the microcavity.

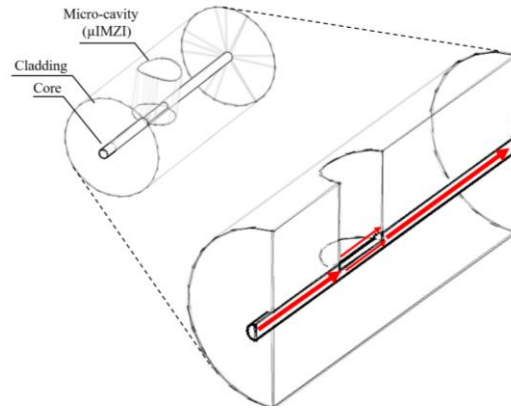


Figure 2. Schematic drawing of the μ IMZI structure

Thanks to the micrometer size, the sensor has a unique capability for investigating sub-nanoliter volumes of liquids. A remarkable and unique feature of this sensor is that the external media can directly interact with the fiber core. The light-analyte coupling makes the cavity-based devices much more sensitive in comparison to evanescent sensors. The μ IMZI device offers RI sensitivity reaching over 20,000 nm/RIU, making it one of the most RI-sensitive devices to date². Due to very precise fabrication, the device is small, highly reproducible, portable, and in contrast to, e.g. the LPG, it is temperature-insensitive⁴⁶.

One of the first presented μ IMZIs made solely using fs laser ablation was based on a V-shape microcavity. The sensitivity of this sensor reached 9370.84 nm/RIU within the range 1.31-1.335 RIU⁴⁵. Then Jiang et al. developed a μ IMZI sensor with a U-shape structure which exhibited RI sensitivity reaching 12,000 nm/RIU in the RI range from 1.3330 to 1.3381 RIU for investigation of sucrose solutions⁴⁷. A μ IMZI sensor based on a D-shape cavity was also reported⁴⁸. For RI measurements purposes, the structure exhibited sensitivity as high as 10,000 nm/RIU for acetone vapor.

Some other μ IMZI structures needed additional post-processing, for example, fusion splicing⁴⁸. They were micromachined inside a fiber and used mostly for RI and strain monitoring. Moreover, some structures were fine-tuned by wet etching in hydrofluoric acid (HF). Sun et al. shown U⁴⁹ and V-shape⁵⁰ μ IMZIs structures, which exhibited sensitivity as high as 10,000 and 17,197 nm/RIU, within the RI range 1.332-1.352, and 1.3371-1.3407 respectively.

In this work, we developed a highly optimized protocol which allows us to explore the properties of the in-fiber device and prepare the sensor for further investigation. The fs fabrication protocol aiming to create precise, repeatable microcavities is as follows:

All cavities presented in the thesis were fabricated in standard Corning SMF28 fibers. All of them have a circular cross-section, flat bottom (diameter, d), while their walls (height, h) with good approximation are perpendicular to the fiber's long axis (Fig. 3).

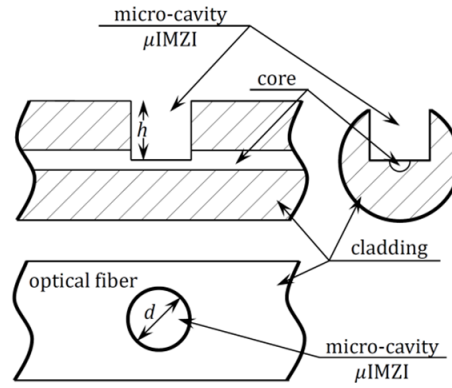


Figure 3. Schematic drawing of the μ IMZI structure. The diameter of the micro-cavity is indicated by d and the depth by h .

The micromachining process was done using a Solstice Ti:Sapphire fs laser operating at $\lambda = 795$ nm. The fiber was irradiated by 82 fs pulses. The system worked with a repetition rate of 10 kHz. In order to make the microcavity, the laser beam was directed into a suitably designed micromachining setup based on the Newport μ Fab system. The system was equipped with a 20x lens, with NA = 0.30. The laser pulse energy was equal to 6 nJ. Fiber transmission was monitored during the process with an NKT Photonics SuperK COMPACT supercontinuum white light source and a Yokogawa AQ6370C optical spectrum analyzer. The fabrication process was controlled with our in-house developed software, while the motion of the beam relative to the fiber was adjusted and managed by the software supplied by Newport with the μ Fab system. The fabrication setup is schematically shown in Fig. 4.

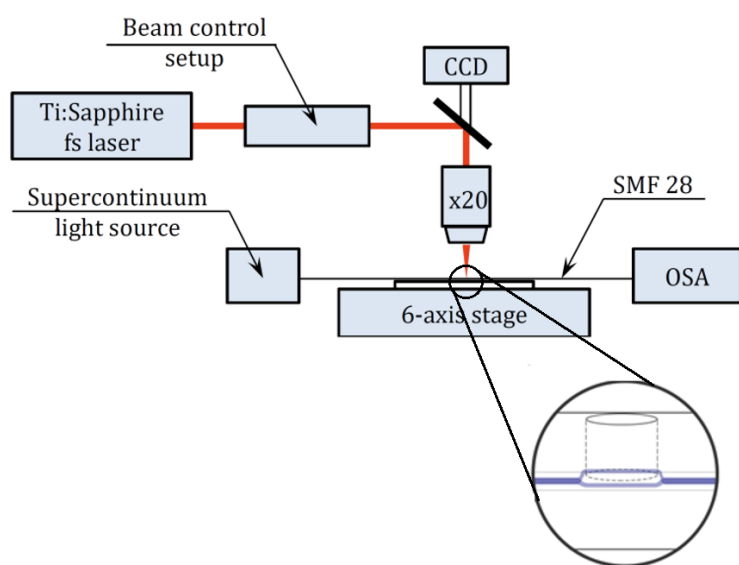


Figure 4. Scheme of the fs-laser based microfabrication setup.

3.3. PHYSICAL PROPERTIES OF THE INVESTIGATED μ IMZI

We choose four μ IMZIs with different diameters to illustrate their exceptionally high sensitivity and their potential for bio- and chemical measurements. Their dimensions are shown in Table 2. An investigated volume of liquid in the microcavity can be as small as 177 pL depending on the structure.

TABLE 2
CHARACTERIZATION AND APPROXIMATE DIMENSIONS OF THE FOUR INVESTIGATED STRUCTURES

Sample	A	B	C	D
diameter [μm]	30	40	54	64
depth [μm]		62.5		
volume [pL]	177	314	572	804
Cut-off wavelength λ_c [nm]		1260		
Mode Field Diameter MFD [μm]		8.2		
Numerical aperture NA		0.14		

To make the above structures comparable, to obtain well-defined interference patterns on the fiber output and to get a good quality of the microcavity surface, each μ IMZI was precisely micromachined following the optimized parameters described in the previous section. Especially a depth of the cavity had to be very well adjusted since it determines the light splitting rate. Figures 5 and 6 present SEM visualization and profilometer scan through one of the μ IMZI, which proves that the depth reaches exactly half of the fiber core (62.5 μm). It is important to underline that the whole surface of the structure is smooth, well-defined, the bottom is flat and precisely micromachined, and that no additional damages are introduced to the cavity or to the working area.

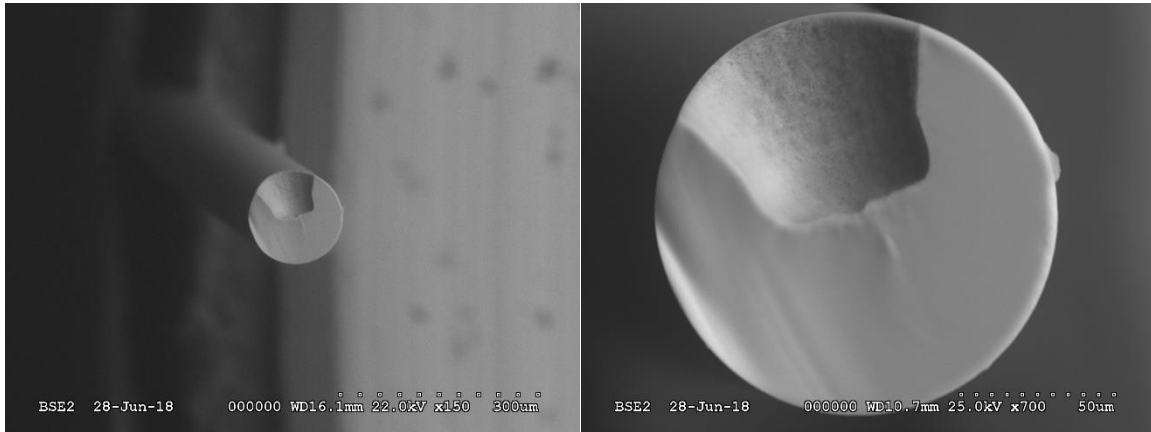


Figure 5. SEM visualization of one of the μ IMZI structures (structure shown here is described in the Table 2 as C)

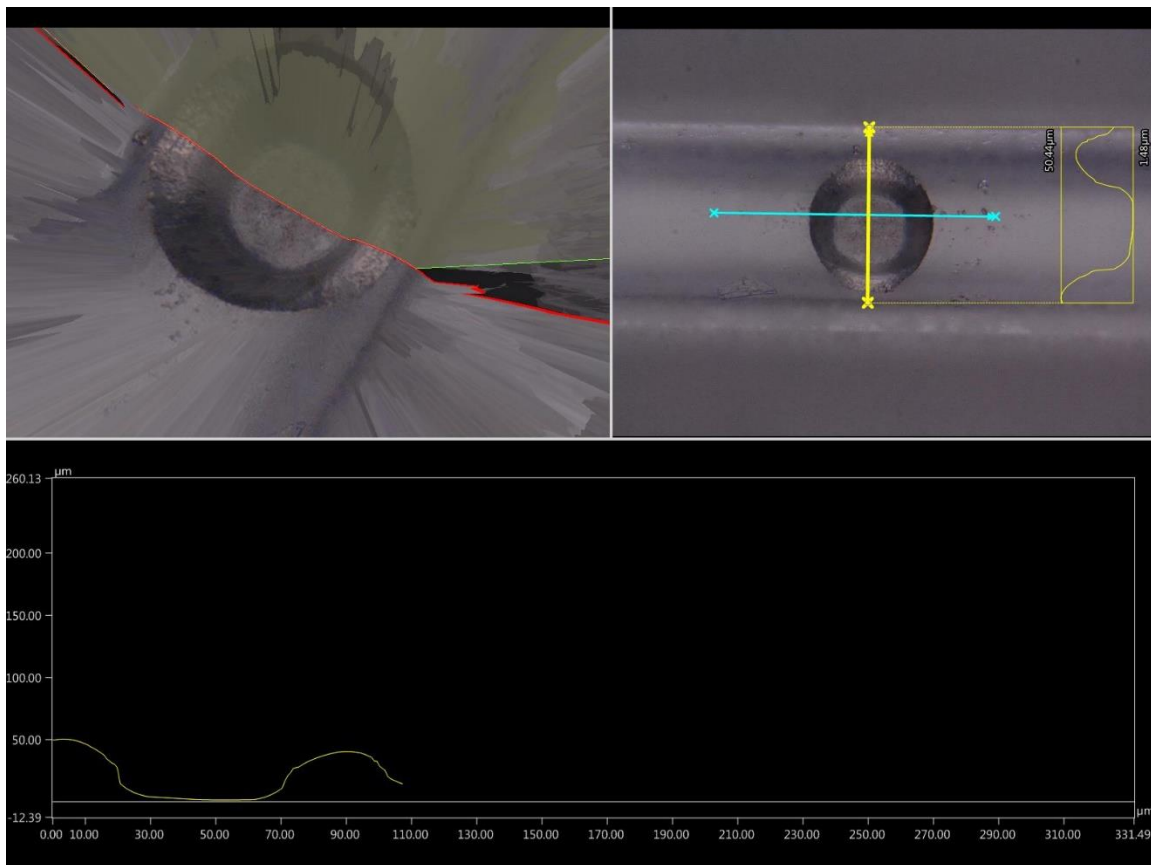


Figure 6. Profilometer scan through the μ IMZI structure.

3.4. GENERAL THEORETICAL CONSIDERATIONS

We can describe the effect occurring at μ IMZI by general interferometric Equation (1), where I is the resultant intensity, while I_1 and I_2 are the intensity of the field in the core and the cavity respectively. In Equation (2) ϕ is the accumulated phase difference in the interferometer at wavelength λ . The effective refractive index difference between the core mode effective refractive index and that of the medium inside the cavity is $\Delta n_{eff} = n_{core} - n_{cavity}$. L represents the effective length of the interferometer, while ϕ_0 is the initial phase difference.

$$I = I_1 + I_2 + 2\sqrt{I_1 I_2} \cos \phi \quad (1)$$

$$\phi = \frac{2\pi}{\lambda} \Delta n_{eff} L + \phi_0 \quad (2)$$

The interference fringe pattern has minima for every odd multiple of π , thus based on Equations (1) and (2):

$$\frac{2\pi L \Delta n}{\lambda_m} + \phi_0 = (2m + 1)\pi \quad (3)$$

Here λ_m is the wavelength of the m th-order interference dip and m is an integer. After a rearrangement the Equation (3) takes the form:

$$\lambda_m = \frac{2\pi L \Delta n_{eff}}{(2m+1)\pi - \phi_0}, \quad (4)$$

which defines λ for every minimum. When the Δn_{eff} of the μ IMZI changes, the minimum shifts by an amount $\partial \lambda$. Assuming that the length (L) of the cavity is kept constant, the sensitivity of the μ IMZI can be expressed as:

$$S_m = \frac{\partial \lambda}{\partial (\Delta n)} = \frac{\lambda}{\Delta n}, \quad (5)$$

According to the Equation (3), the free spectral range (FSR), determined by the cavity length, is described as the wavelength difference between two consecutive resonances, and can be written as:

$$FSR = \frac{\lambda^2}{\Delta n L} \quad (6)$$

3.5. REFRACTIVE INDEX SENSITIVITY OF THE μ IMZI

We performed the RI sensitivity measurements of the μ IMZIs on specially prepared testing surfaces which allowed for the precise control of the amount of dosed liquid and filling of the microcavity. The optical transmission of the μ IMZI was monitored in the spectral range of 1100-1700 nm using the same light source and spectrum analyzer as during the micromachining (Section 3.2). A set of water/glycerin solutions, where RI varied in the range from 1.3330 to 1.3900 RIU was used to perform the measurements. The RI of the reference solutions was measured using an automatic digital refractometer VEE GEE PDX-95. Temperature and strain were kept constant during all the RI measurements.

At first, we compared four structures with diameters equal to 30, 40, 54, and 64 μ m to examine the properties of the μ IMZI and study the influence of the μ IMZIs diameter on the RI sensitivity. To make them comparable, we fabricated the microcavities in the way that the obtained resonances were present in the range of 1250-1350 nm. A comparison of measurement results for selected samples in water is presented in Fig. 7.

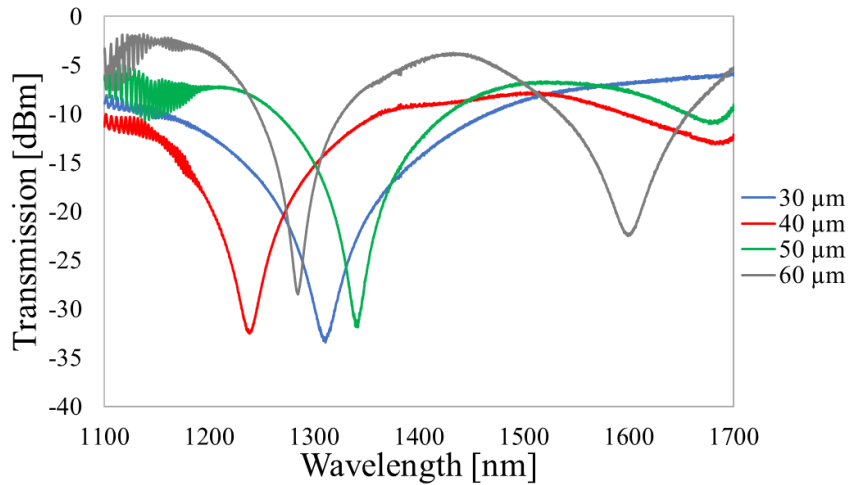


Figure 7. A comparison of results for microcavities with diameters $d = 30, 40, 54$ and $60 \mu\text{m}$ filled with water ($n = 1.3333$ RIU).

It can be observed that the interference response is periodic and with an increasing diameter, the distance between the minima becomes smaller. The μ IMZI structures display multiple minima with free spectral range (FSR) ranging from 293 to 563 nm (Table 3).

TABLE 3
APPROXIMATE FREE SPECTRAL RANGES OF THE FOUR INVESTIGATED STRUCTURES

Sample	A	B	C	D
diameter [μm]	30	40	54	64
Free spectral range [nm]	563	498	392	293

This property makes μ IMZIs convenient for sensing purposes and allows for adjusting the specific location of the minimum, depending on, e.g., the wavelength range of the interrogating system. What has to be taken into account, the microcavities were made in standard SM fibers where the cut off wavelength was $\lambda_c = 1260$ nm (Table 2). Below this value, the fiber supports multimode operation, and because of that, the high-frequency oscillations may be observed in the spectrum at shorter wavelengths.

Figs. 8A-11A show the transmission spectra of the samples A-D for the RI in the microcavities varying from 1.3333 to 1.3815 RIU. In Figs. 8B-11B, the corresponding spectral locations of the minima are plotted as a function of RI for microcavity samples with different diameters. The points corresponding to each sample are linearly approximated with the least square method, and the values of sensitivity in different RI regions are obtained.

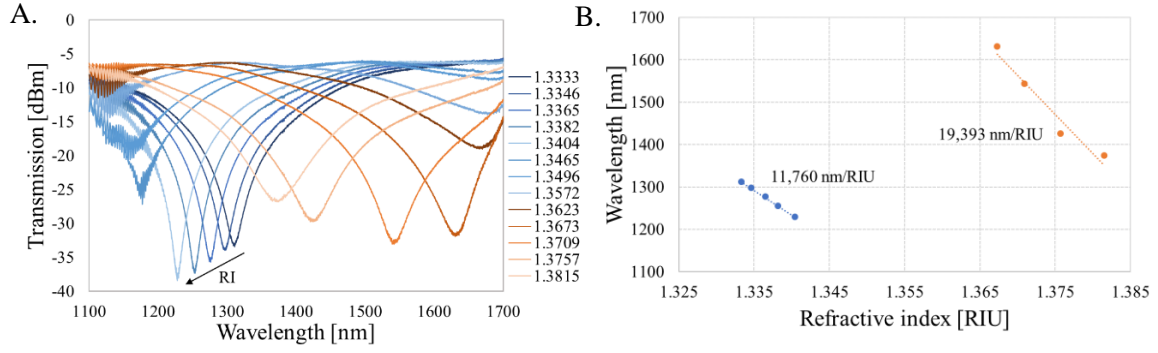


Figure 8. A) Spectral response and B) sensitivity of the μ IMZI with microcavity diameter $d = 30 \mu\text{m}$ for aqueous solutions with n ranging from 1.33 to 1.38 RIU.

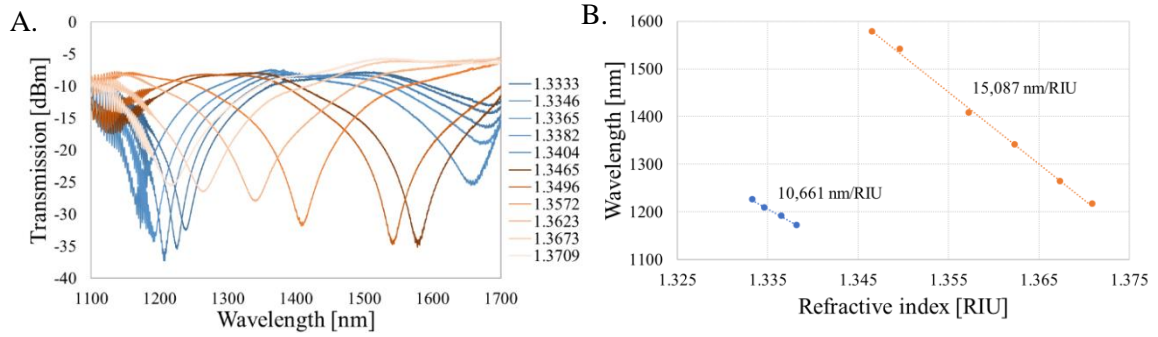


Figure 9. A) Spectral response and B) sensitivity of the μ IMZI with microcavity diameter $d = 40 \mu\text{m}$ for aqueous solutions with n ranging from 1.33 to 1.37 RIU.

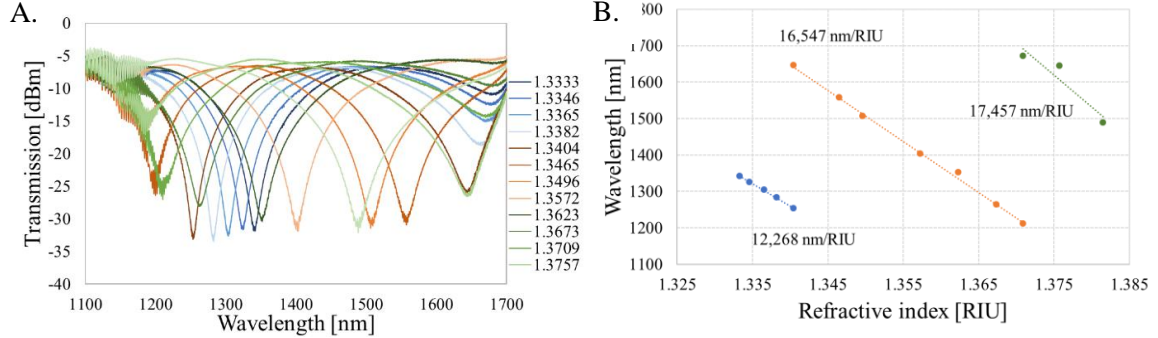


Figure 10. A) Spectral response and B) sensitivity of the μ IMZI with microcavity diameter $d = 54 \mu\text{m}$ for aqueous solutions with n ranging from 1.33 to 1.38 RIU.

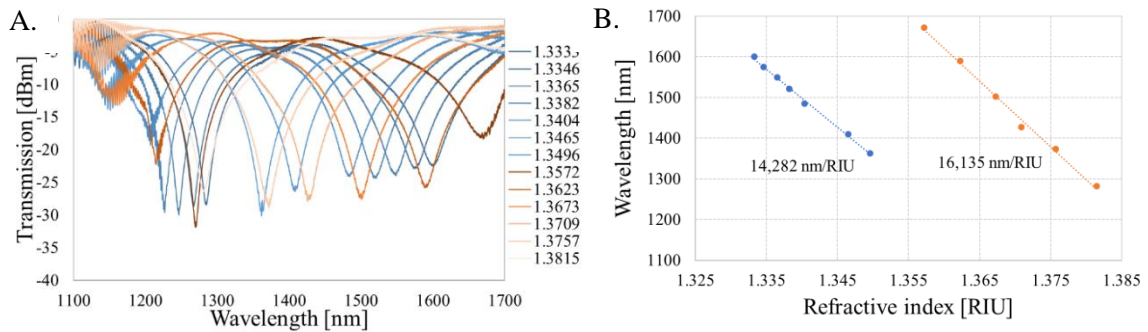


Figure 11. A) Spectral response and B) sensitivity of the μ IMZI with microcavity diameter $d = 64 \mu\text{m}$ for aqueous solutions with n ranging from 1.33 to 1.38 RIU.

Both the transmitted power and the central wavelength of the minima change with increasing RI. The minimum shifts towards shorter wavelengths in all cases. In the case of the structures with diameters 30, 40 and 54 μm , two minima can be observed when the RI increases, and both of them experience similar shifts. With a greater diameter of the microcavity – $d=64 \mu\text{m}$, the second minimum occurs at lower RI, and at higher RI even a third minimum appears. Due to the smaller free spectral range, the number of the observed minima in the analyzed RI range increases with the diameter of the microcavity.

The μIMZIs described in this section display the sensitivities ranging from approximately 11,000 nm/RIU (RI between 1.3333 – 1.3400 RIU) up to almost 20,000 nm/RIU for the smallest cavity (RI between 1.3575 – 1.3715 RIU). We can notice that in all cases overall sensitivity increases along with the increasing RI. All the fabricated interferometric structures have a small or negligible deviation of points from approximation lines which reveals high linearity of the μIMZIs ' RI sensitivity.

The sensitivity of the microcavity-based structure may be expressed by extending the Eq. 5 from Section 3.4. λ denotes the wavelength of a minimum, n_{ext} is the value of the RI of the examined liquid solution, d is the diameter of the cavity, and ϕ_0 is an initial phase. $n_{\text{eff}}^{\text{co}}$ represents the effective RI of the remaining part of the fiber core and n^{cl} is the RI of the cavity.

$$S_m = \frac{\partial \lambda}{\partial (\Delta n)} = \frac{\lambda}{\Delta n} = \frac{2\pi d}{(2m+1)\pi - \phi_0} \left(\frac{dn_{\text{eff}}^{\text{co}}}{dn_{\text{ext}}} - \frac{dn^{\text{cl}}}{dn_{\text{ext}}} \right)$$

We can assume that $n_{\text{ext}} = n^{\text{cl}}$ since the liquid covers the whole cavity. In our case the most critical and meaningful term is $\frac{dn_{\text{eff}}^{\text{co}}}{dn_{\text{ext}}}$. With increasing $dn_{\text{eff}}^{\text{co}}$ the overall value of the term in the parenthesis becomes dominant and implies the increase of the sensitivity.

The above equation shows that the sensitivity also depends on the diameter of the cavity, however changing the size of the μIMZI does not have a significant influence on overall sensitivity, what is experimentally confirmed in this section. In Figure 12, the spectral locations of minima are plotted vs. RI in the cavity for all described samples. The points corresponding to each sample are linearly approximated with the least squares method, which allows obtaining the values of sensitivity in different RI regions. The comparison reveals that, in the range of

$n = 1.3333$ to 1.3400 RIU, the sensitivity barely depends on the cavity diameter. Its values are comparable and range from $10,661$ to $12,268$ nm/RIU. The next minima, occurring with the increasing RI, seem to show similar tendency as the previous one, where the values of sensitivity reached from $14,008$ to $15,087$ nm/RIU. The highest sensitivity exceeding $19\,393$ nm/RIU has been obtained for the smallest microcavity.

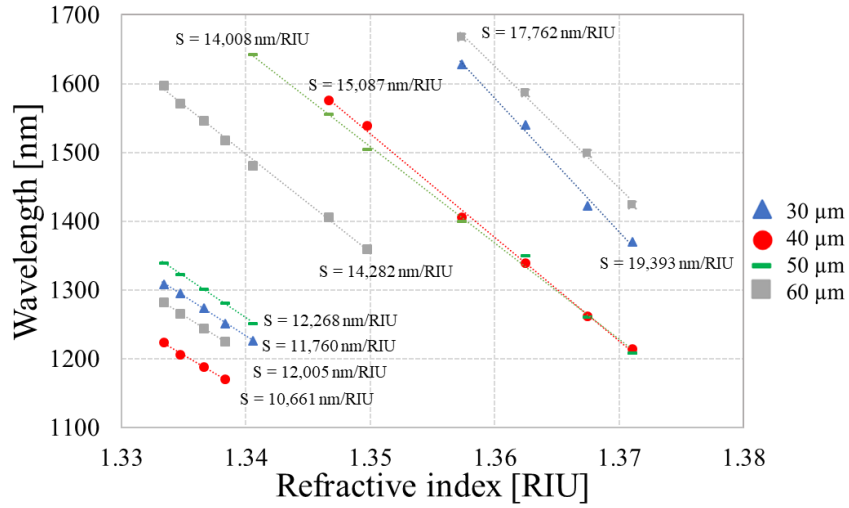


Figure 12. Sensitivities of the investigated μ IMZI structures for different microcavity diameters.

3.6. TEMPERATURE SENSITIVITY OF THE μ IMZI

Having an ultra-high RI sensitivity is a big advantage in terms of bio and chemosensing; however, it can be easily disturbed by some factors such as temperature. Many reported fiber-optic sensing devices suffer from large temperature cross-sensitivity drawbacks.

In order to demonstrate the T-insensitive RI sensing effect of the μ IMZI structure, the reference μ IMZI was placed in a temperature-controlled cell and immersed in water. A home-made aluminum flow-cell where the bottom part was temperature-controlled, was used for this experiment. The transmission spectrum was monitored while we gradually increased the temperature from 10 to 45°C with a 5°C step.

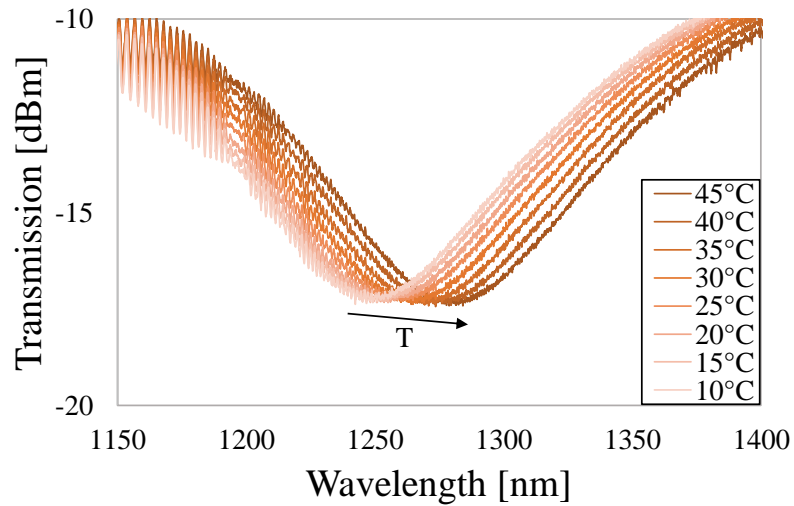


Figure 13. Transmission spectra of μ IMZI at different H₂O temperatures in the cavity.

The spectra obtained during these measurements presented in Fig. 13 show that with the increase of temperature, the minimum moves towards longer wavelengths. Over the range of the temperature applied during the described experiment (10 - 45 °C) the thermo-optic coefficient ($6.3 \times 10^{-6} / ^\circ\text{C}$) and thermal expansion coefficient ($0.55 \times 10^{-6} / ^\circ\text{C}$) of the fiber materials can be considered as constant⁴⁰. This is why we treated the RI of the fiber core, as well as the diameter of the microcavity, as invariable values.

The obtained temperature sensitivity of the μ IMZI in water was 1.2 nm/°C at a wavelength of about 1250 nm . This effect was induced mainly by the RI sensitivity of the structure which is $\sim 15,000$ nm/RIU. Since the thermo-optic coefficient of water reaches -1×10^{-4} RIU/°C and is two orders of magnitude larger than that of the fused silica (6.3×10^{-6} /°C), we can conclude that the observed shift of the minimum is induced almost exclusively by the change of the RI of water caused by the variation of temperature.

3.7. CONCLUSIONS

In this chapter, we presented the overall characteristics of the μ IMZI device, including the physical properties of a cylindrically-shaped microcavities in-fiber MZI fabricated solely with a femtosecond laser. Experimental results showed excellent repeatability of the micromachining process. Furthermore, all of the tested optical fiber structures exhibit high and linear RI sensitivities in a wide range of the investigated RIs, where the sensitivity is practically independent on the cavity diameter. Also, we proved the fact, that the μ IMZI is temperature insensitive.

CHAPTER 4

CLEANING AND PREPARING THE μ IMZI FOR FURTHER FUNCTIONALIZATION

Chapter 4 presents preparation of the μ IMZI device for further measurements and for the surface functionalization processes. To clean the microcavity and increase the hydrophilicity of its surface we make use of Reactive Ion Etching (RIE). The results of the experiments exposing the μ IMZI-based structure to RIE are given at the beginning of the chapter. Next, two RIE processes, where SF_6/O_2 and O_2 are used as reactive gases are compared. The comparison includes the properties of reactive gases, the influence of the RIE process on the spectrum, the μ IMZI behavior, the wettability of the surface and stability of the surface's properties after the RIE treatment. The RIE process is also compared with widely used HF wet etching.

The work introduced in this section was presented in:

1. M. Janik, A. K. Myśliwiec, M. Koba, A. Celebańska, W. J. Bock and M. Śmietana, “Sensitivity Pattern of Femtosecond Laser Micromachined and Plasma-Processed In-Fiber Mach-Zehnder Interferometers, as Applied to Small-Scale Refractive Index Sensing,” *IEEE Sens. J.* 17, 11, 3316-3322 (2017);
2. M. Janik, M. Koba, A. Celebańska, W. J. Bock and M. Śmietana, “Sensing properties of micro-cavity in-line Mach-Zehnder interferometer enhanced by reactive ion etching.” *Journal of Optics and Laser Technology* 103, 260-266 (2018).

Besides the certain advantages of the μ IMZI structure, some challenges remain to be solved to improve this sensing concept. The small size of the cavity makes it difficult to clean. Even tiny pieces of glass remaining in the cavity after the fabrication process can reduce its volume while also reducing the sensing area. Such residues can affect the sensitivity of the device and most importantly, the repeatability of the measurements. Additionally, the glass residues can cause light scattering and optical signal distortion, which in turn increase the insertion loss of the μ IMZI.

Filling the cavity with a liquid may trigger further problems, especially in the case of high-density liquids with high viscosity. All of these issues indicate that a high degree of control over the cavity depth is required to achieve faster, more repeatable, and more accurate measurements. The majority of the mentioned problems can be solved by the μ IMZI etching – a process which can be a part of the fabrication post-processing. Etching of optical fibers has already been applied as a means of enhancing the sensing properties of optical fiber sensors. However, this technique has never been used before to prepare the surface for biosensing. Two techniques are widely employed, namely, those using liquid etchants, e.g., wet etching in hydrofluoric (HF) acid^{49,51}, or those based on dry etching, i.e., plasma-based etching^{25,52}, which includes reactive ion etching (RIE).

In general, when RIE is applied, in addition to the chemical etching by plasma-activated ions, the ions are also accelerated towards the surface of the sample, and physically remove the material at nanometers level by a high-energy bombardment of the surface⁵³. Fluorides such as SF₆ or carbon tetrafluoride (CF₄), are typically used as etching reagents of silicon-based materials. In fluorine plasma, the F ions are the principal etchant, but the addition of O₂ might be used to increase the etching rate⁵⁴. The application of O₂ has a dual role in this process: it enhances the production of the etchant, i.e., F ions, and it also occupies the active silicon etching sites, not only delaying the etching reaction but also significantly increasing the wettability of the etched surface⁵⁴. It is worth mentioning that plasma processing is highly accurate (at nanometers level) and more precise than any other wet etching process, especially when narrow trenches are processed. In contrast to most of the wet chemical reagents, plasma is relatively nontoxic and noncorrosive⁵⁵. Thus, the RIE processes were found to be far superior to the wet etching for achieving the modification of small cavities.

4.1. REACTIVE ION ETCHING OF THE SURFACE

We performed the RIE process using the Oxford PlasmaPro NGP80 system. During the experiment, the plasma was obtained at a pressure of 100 mTorr and at RF power of 250 W. The flows of the SF_6 and O_2 gases were set to 30 and 100 sccm, respectively. The O_2 RIE process was conducted with an O_2 flow of 50 sccm, pressure 100 mTorr and power 100 W. Each RIE process was 3 min. long. The temperature during all the processes was stabilized at 20°C . The μIMZI samples were placed in the plasma chamber together with an oxidized silicon wafer (SiO_2/Si), used as a process control reference. Changes to the thickness of the reference wafer induced by the RIE process were investigated using a Horiba Jobin-Yvon UVSEL spectroscopic ellipsometer following the procedure reported in⁵⁶.

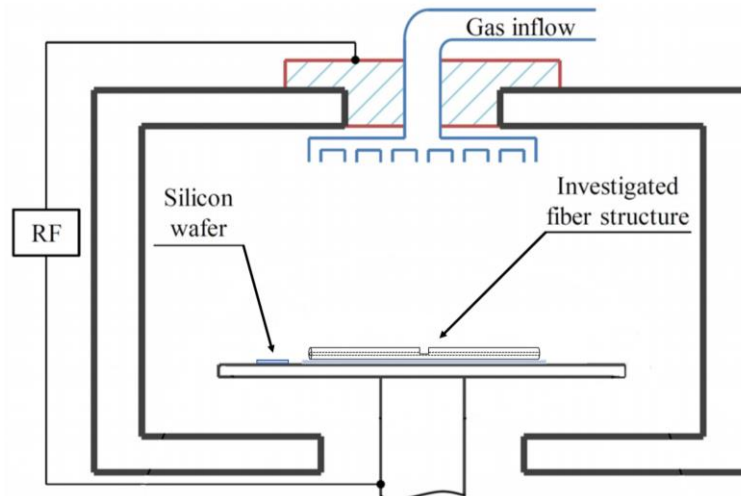


Figure 14. Schematic representation of the μIMZI and SiO_2/Si wafer placement in the RIE process chamber.

4.2. CLEANING EFFECT OF SF₆/O₂ RIE

A structure with $d = 54 \mu\text{m}$ was chosen to illustrate the effect of SF₆/O₂ RIE on the properties of the μIMZI . Following the process detailed in Section 4.1. the sample underwent five consecutive 3-min.-long etching processes. The transmission spectra before and after each process, measured after filling the cavity with deionized water, are shown in Fig. 15.

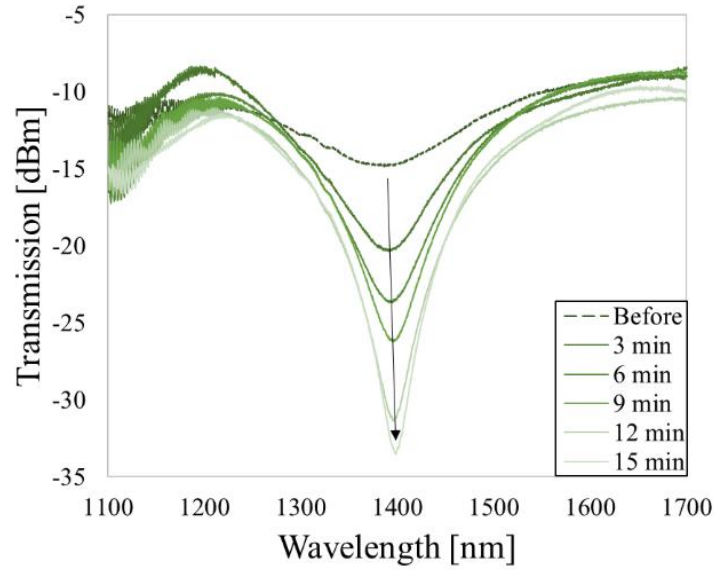


Figure 15. The effect of five consecutive SF₆/O₂ RIE processes on the μIMZI transmission spectrum. The measurements were made after filling the microcavity with water.

Comparison of the spectra reveals that the etching effect is evidenced by an increase (by nearly 20 dB) in the depth of a minimum. The effect is distinguishable in the spectrum transmission, while barely noticeable in the wavelength domain. The evolution of the transmission spectra with the RI in the micro-cavity varying from RI = 1.3333 to 1.3809 RIU before and after all the RIE processes is shown in Fig. 16A and B, respectively. It can also be seen that the etching process strongly affected these results. The traced minima of the μIMZI spectrum are smoother and more pronounced.

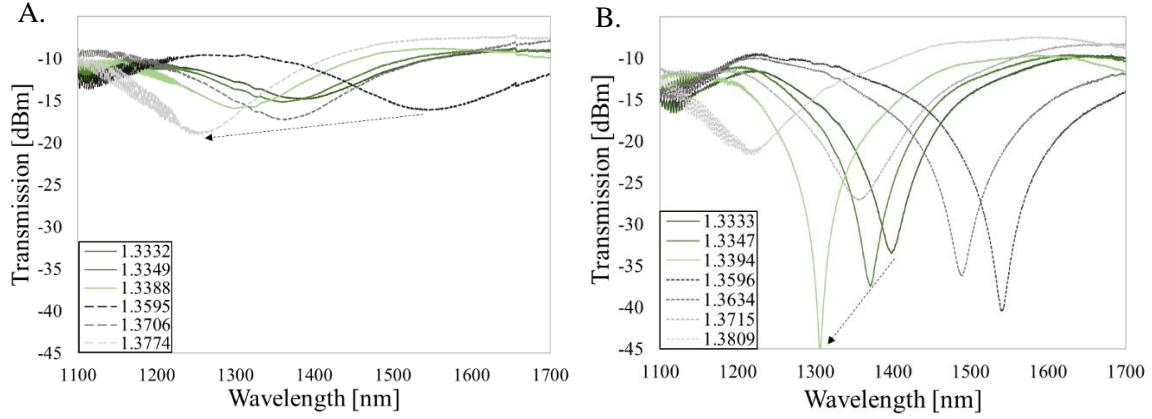


Figure 16. Spectral response of the μ IMZI A) before and B) after all the SF_6/O_2 -based RIEs for solutions in the microcavity with RI ranging from 1.33 to 1.38 RIU.

The corresponding spectral locations of the minima are plotted vs. RI in Fig. 17. The points representing each minimum are linearly approximated with the least square method, and the values of sensitivity in different RI ranges are given. The SF_6 RIE also had a small, but noticeable impact on the overall RI sensitivity. As depicted in Fig. 17, the sensitivities after RIE post-processing in both RI ranges, namely 1.3333 to 1.3500 RIU and 1.3600 to 1.3900 RIU, are more than 1,000 nm/RIU higher than before the etching.

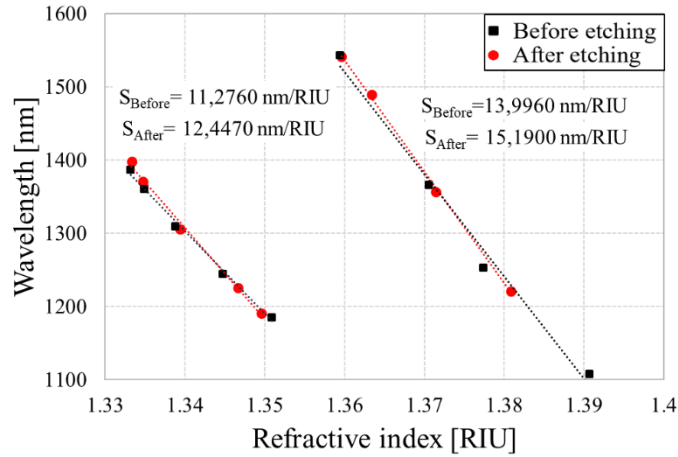


Figure 17. Sensitivities of the investigated μ IMZI structure before (S_{Before}) and after (S_{After}) all five SF_6/O_2 RIE processes.

4.3. CLEANING EFFECT OF O₂ RIE

The results of the study presented in the previous section are now compared to the results of experiments using O₂ RIE solely. For the sake of comparison, we used the same structure with diameter $d = 54 \mu\text{m}$. A single sample underwent three consecutive etching processes, detailed in Section 4.1, two in O₂ and an additional one in SF₆/O₂. The transmission spectra before and after each process measured after filling the cavity with water are shown in Fig. 18A.

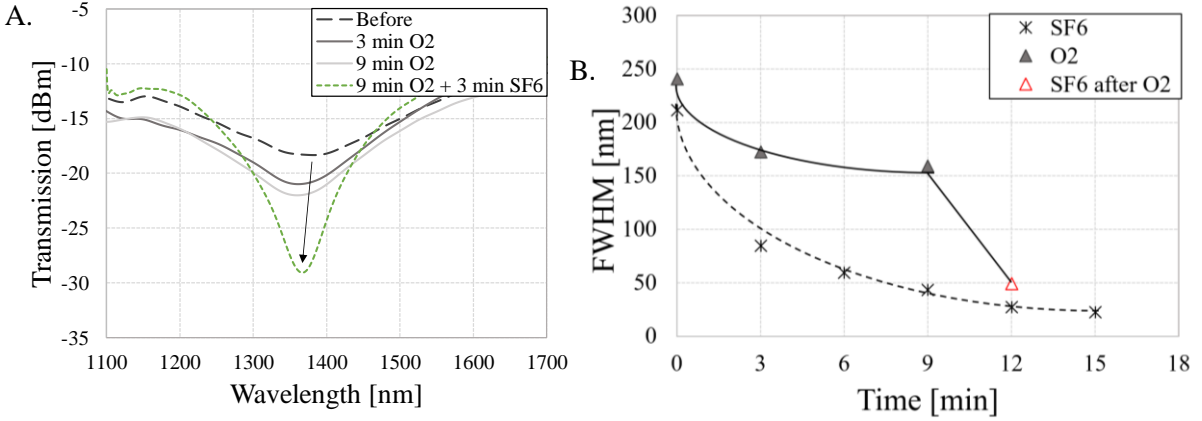


Figure 18. A) The effect on the μIMZI transmission spectra of three RIE processes, two with O₂ and an additional one with SF₆/O₂. The measurements were made after filling the micro-cavity with water. B) Influence of reactive gas on FWHM after each RIE process. The final etching of the O₂ sample was done with SF₆/O₂.

Analysis of the O₂-based etching effects vs. SF₆/O₂ RIE effects indicates that O₂ RIE has very little influence on the spectrum. As shown in Fig. 18A, the O₂-based processes improved smoothness and depth of the minimum (in total by about 3 dB), but much less than the SF₆/O₂ RIE (by about 7 dB). The additional SF₆/O₂ etching of the sample shows a substantial difference in the effectiveness of the two processes. This can be seen when we compare full width at half maximum (FWHM) after each RIE process (Fig. 18B). The first SF₆/O₂ RIE process reduced the FWHM by approx. 130 nm, while the corresponding O₂ RIE decreased its value by only approx. 60 nm. During the next 6 min. of etching the FWHM value decreased by 41 for the SF₆/O₂ RIE and only by 13 nm for the O₂-based RIE process. Taking into account the very low efficiency of the O₂ etching, i.e., a saturation effect, the process was followed by SF₆/O₂ RIE, and it reduced the FWHM by approx. 100 nm.

Before and after the O₂ RIE processes, the values of the wavelength minima for both analyzed cases were similar, so even though the process slightly affected the spectra, it had no impact on the overall sensitivity².

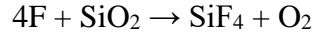
4.4. COMPARISON OF THE TWO PROCEDURES.

It can be stated that both types of etching influenced the depth of the resonance minimum of the sensors. This influence is intensified under the SF₆/O₂ RIE process. As already shown in⁵⁷, even after 10 minutes of O₂-based RIE processes with different values of RF power, the effects obtained on the SiO₂/Si substrate were negligible. In contrast, SF₆/O₂ is a more powerful etchant and even after a short period has a significant influence on the SiO₂ surface. Despite all advantages of the RIE processes, SF₆/O₂ RIE may potentially cause significant reduction of the fiber cladding, affecting any further measurements of post-processed samples, e.g., when other sensors are also made in the same fiber.

Plasma treatment also changes the surface wettability due to the two processes⁵⁸. The first one includes plasma cleaning of the organic contaminants (mostly from ubiquitous hydrocarbons) which are adsorbed at the silicon dioxide from the environment⁵⁹. The second process includes the generation of hydrophilic oxygen-based polar groups, like hydroxide groups, which can also regulate the hydrophilic properties of the surface⁶⁰. The O₂ RIE increases surface wettability and makes the surface hydrophilic. This is why the O₂ RIE treatment is one of the most popular methods used for instance for:

- gentle surface cleaning (mainly from ubiquitous hydrocarbons but also other contaminations, even biological)^{61,62}
- surface activation (such as silicon converting to an oxidized state or densification of hydroxyl functional groups at a silica surface)^{62,63}
- and also as an adhesion promotion⁶⁴

When we combine the oxygen with a fluorine-containing gas (SF₆), the properties of the reactive gas are different, and instead of just cleaning, etching of a surface is possible^{60,65–68}. Typically, RIE combines both chemical and physical processes. Highly reactive fluorine radicals play the primary role in the etching by SF₆/O₂ plasma, according to the reaction:



It explains why the mentioned treatment is more drastic in comparison with O₂ plasma cleaning. Furthermore, the addition of O₂ to SF₆ RIE leads to a net increase of F atoms and thus to a higher etching rate⁶⁹. Their interaction with the sample results in formation of volatile products like SiF₄⁶⁵. The etching rate can be tuned from 6.5 to even 103 nm/min merely by adjusting the power of an RF generator from 50 to 250 W, and by altering the distance between the sample and the electrode⁵².

Structural changes, such as, smoothing the surface^{70–72} can affect the contaminants adsorption process or its rate, because of the decreased number of available adsorption centers. It can be further stated that SF₆/O₂ RIE post-processing mainly cleans and evens the cavity surface. The latter issue might have a crucial impact on the accuracy and repeatability of the measurements. A flat and clean bottom surface is impossible to obtain exclusively with micromachining. Moreover, the etching rate determined on reference wafers (~100 nm/min) suggests that, along with the reduction of the fiber cladding, the cavity's bottom is also deepened by as much as 1.5 μm which may increase the RI sensitivity of the device. The RIE applied to the microcavities allows for highly-precise post-processing.

Considering the results shown above, we can conclude that both types of etching, SF₆/O₂, and O₂ RIE, improved the smoothness of the spectrum and visibility of the transmission minima. Importantly, our work revealed the basic differences between these two RIE processes. Compared to laser micromachining, SF₆/O₂ RIE is a very gentle process and can be very well controlled. On the other hand, the process is strong enough to tune the sensing properties of the microcavity precisely. Such accurate tuning cannot be achieved during microfabrication or as a result of O₂ RIE post-processing.

4.5. STABILITY AND DURABILITY OF THE PLASMA TREATMENT

Due to the very small size of the microcavity, conventional cleaning methods may not be effective. The process of filling the cavity with liquid solutions is not trivial, especially when liquids of high RI and viscosity are applied. That is why a high wettability of the cavity inner surface is required. As a result of our previous experiments, we have found that an adequately designed RIE process may increase the surface wettability more than any other post-processing procedure. We perform series of contact angle measurements to follow changes in wettability of the RIE treated surfaces.

We measured the water contact angle on the wafer using a Celestron 5 MP Handheld Digital Microscope Pro with a 1 μ l water droplet (10 seconds after deposition) by averaging five consecutive measurements. We repeated the measurements after 24, 48, 72 hours, 1 week, and 2 weeks of storage of the samples in the air. In order to compare the impact on the wettability of the oxygen-plasma and HF post-processing, evaluation measurements were performed for the samples etched for 2 minutes in 5% aqueous solution of HF acid. Finally, possible changes in thickness of the SiO₂ layer induced by the RIE process were investigated using a Horiba Jobin-Yvon UVSEL spectroscopic ellipsometer following the procedure reported in⁵⁶.

Figure 19 shows the changes in the water contact angle before and after the O₂ etching process. As a result of the etching process, the contact angle was unmeasurable due to very high hydrophilicity of the surface (Fig. 19). This made it possible to easily introduce the liquid sample into the microcavity, facilitating measurement of liquids with higher RI or high viscosity. The time which takes the liquid to fill the cavity fully is strongly dependent on its properties, such as size and shape. Before the plasma processing, it usually took around 12-15 minutes for the high-viscosity liquids to fill the cavity. After plasma treatment, the filling the cavity was immediate, independently of the cavity size and liquid viscosity.

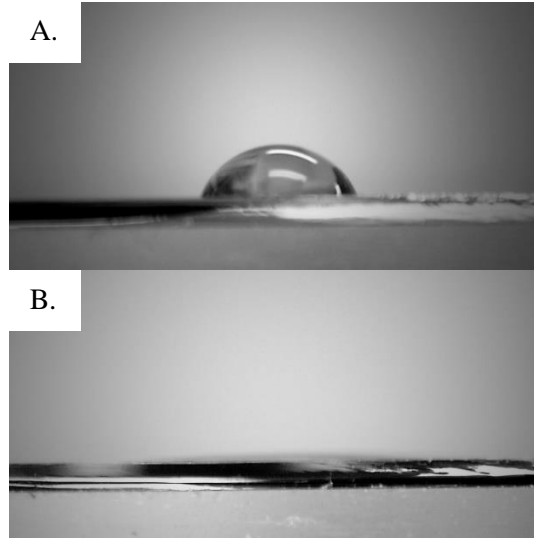


Figure 19. Effect of O_2 etching process on SiO_2 surface properties: A) before (contact angle is equal to 64°) and B) after (contact angle is unmeasurable because of high wettability).

Next, we investigated the effect of RIE with different gases on the wettability characteristics. Taking into account that some samples are preprepared and RIE treated in advance we checked the durability of the plasma treatment. We observed the so-called, aging process describes the hydrophobicity recovery of the surface after wettability improvement by the RIE treatment. The phenomenon was described for a variety of materials. The wettability degradation depends on the sample storage environment and is affected by many factors such as humidity and temperature⁷³.

In order to mimic our typical experimental setup and the $\mu IMZI$ storage conditions the reference wafers used for contact angle (CA) measurements were constantly exposed to the air. In general, the aging process is mainly caused by carbon contaminations adsorbed from the air as well as by transformation and decreases in the number of hydrophilic groups at the surface^{73,74}. The initial CA for the samples reached 64° . Fig. 20 showed the impact of the SF_6/O_2 and O_2 RIE processes on the CA for the sample stored in the ambient atmosphere and measured 10 minutes, 24 hours, one week, and two weeks after the processing. It is clear that 10 minutes after the etching, the wettability was comparable, and the CA was unmeasurable due to the very high wettability of the surface. However, after 24 hours it was noticeable that the effect of SF_6/O_2 etching was more stable and stayed unchanged. For the O_2 -etched sample, the shadow of the water drop (CA $\approx 11^\circ$) can be seen, which indicates a slightly lower surface wettability for O_2 processing than for SF_6/O_2 . Within one week from etching, the CA of the

SF₆/O₂ RIE sample was still unmeasurable, while the O₂ sample was already close to 34°. After two weeks from etching, the wettability of the SF₆/O₂ processed sample started to decrease but remained higher than for the sample treated with O₂ after one week. It can be then concluded that the effect of SF₆/O₂-based RIE treatment is more stable than that of the O₂ RIE and its surface preserves high wettability for over two weeks.

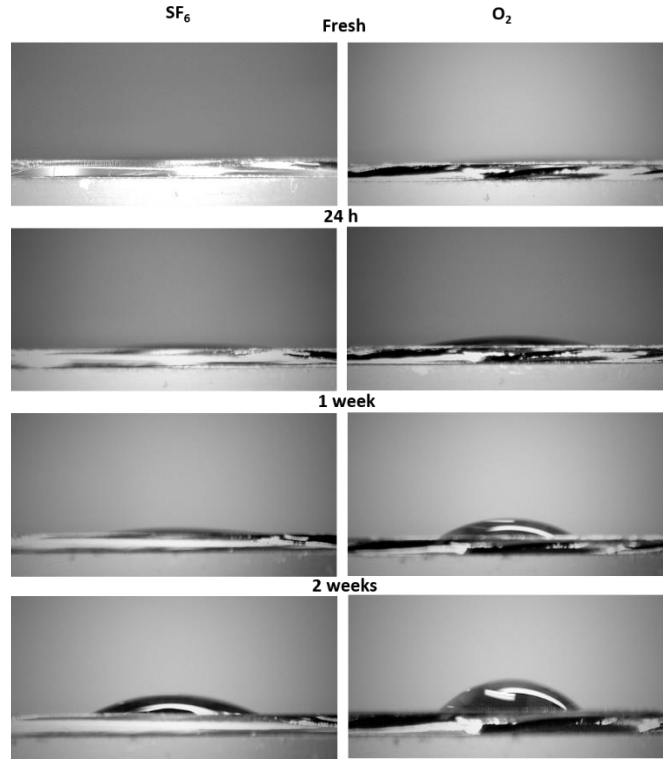


Figure 20. Illustration of the effect of O₂ and SF₆/O₂ etching processes on SiO₂ surface wettability for different storage times in normal conditions.

4.6. COMPARISON OF RIE AND HF WET ETCHING EFFECTS.

The RIE used for microcavity processing can be a more accurate alternative for earlier reported wet etching with HF acid^{48,50}. X. Sun et al. reported two experiments^{49,50} using HF acid to control the transmission spectra after micromachining process. However, in such small cavities (e.g., 50 µm length) this type of the post-processing is very hard to control. In⁴⁹ authors admitted that immersion in 5% HF caused unexpected etching, what resulted in unwanted elongation along with deepening of the presented cavity. In contrast, the RIE is strictly controlled by process parameters, in our case, process time. Above all, the wet etching is also very time-consuming. Comparing to maximum 15 min of RIE postprocessing, wet etching took

from 20 to even 85 minutes⁵⁰. Interestingly, the acid treatment introduces no changes regarding the quality of the spectrum and sensitivity what was noticeable after RIE. On top of cleaning of the cavity from glass shards and tuning the spectrum, RIE allows also for better control on the flat bottom of the micro-cavity. It is also worth to mention that RIE post-processing can play just an additional role, while wet etching in above cited cases is a necessary technological step for continuation of the fabrication process.

4.7. CONCLUSIONS.

In this chapter, the cleaning effects of the reactive ion etching process on a μ IMZI were discussed. The sensors fabricated with a femtosecond laser were post-processed by SF_6/O_2 and O_2 RIE treatment. Even though both types of processing resulted in a visible increase in the spectral depth of the interference minima, the SF_6/O_2 etching had a more significant effect. The process defined the wavelength minima more clearly and thus increased the measurement accuracy. Moreover, the FWHM decreases after each RIE process, but the magnitude of the decrement was significantly higher for SF_6/O_2 RIE than for O_2 RIE.

In contrast to the O_2 RIE, where the main effect was cleaning of the cavity, the SF_6/O_2 RIE not only cleaned the cavity but also evened its surface with a slight but noticeable improvement of the RI sensitivity. What is the most important, the application of RIE increased the wettability of the cavity's surface and preserved this state for even over two weeks (in the case of SF_6/O_2). This in turn significantly facilitated the introduction of liquids into the microcavity. The presented improvements in the functional properties of μ IMZI structures allowed us to proceed with our next objectives.

CHAPTER 5

DEVELOPMENT AND TESTING OF THE μ IMZI SMALL VOLUME LABEL-FREE BIOSENSING CONCEPT BY THIN Al_2O_3 FILM DEPOSITION

This chapter presents the sensor response to thin high-refractive-index (high-RI) Al_2O_3 layer deposition. The experiments allows us to check the capability of the sensor to detect changes on its surface. At first, we present an estimation of the surface RI sensitivity of the device vs. thickness of the high-RI film. Next, we compare the thin-layer deposition effect to controlled microfabrication of shallower cavities. At the end of the experimental part, we provide the theoretical explanation of the obtained results.

The work described in this section was presented in:

1. M. Śmietana, M. Janik, M. Koba, and W. J. Bock, "Transition between bulk and surface refractive index sensitivity of micro-cavity in-line Mach-Zehnder interferometer induced by thin film deposition," *Optics Express* 25, 26118-26123 (2017)
2. M. Janik, M. Koba, A. Celebańska, W. J. Bock and M. Śmietana, "Label-free detection of live *E. coli* bacteria using a microcavity in-line Mach-Zehnder interferometer." *Scientific Reports* 8, 17176 (2018)

Although some highly sensitive sensors based on μ IMZIs have been proposed for sensing strain⁷⁵, pressure⁷⁶ and RI², this platform was never used for specific label-free biosensing (including bacteria detection) before. The μ IMZI exhibits very high RI sensitivity, what corresponds to the liquid filling the cavity (bulk sensitivity). However, it does not determine the sensitivity towards changes occurring on the surface of the sensor, which is crucial for the label-free biosensing (surface sensitivity). Therefore, before applying the μ IMZI for bacteria detection, we studied the response of the sensor to the different RI filling of the cavity and, in a form of a simulation of biolayer formation – the response to the thicknesses of the film deposited at the microcavity's surface. We chose atomic layer deposition (ALD) to evenly deposit ultrathin layer inside such a small structure. This method is capable of angstrom-resolution, layer-by-layer growth of compound films, and therefore allows for outstanding control over the properties of the deposited film regardless of the underlying topography. Moreover, each deposition cycle ensures 100% reproducibility, because of self-saturation occurring when the binding sites on the surface are already occupied⁷⁷.

To show the capabilities of the approach, high-RI Al_2O_3 was applied as a coating material. Al_2O_3 often serves as a protective coating because of its high resistance to mechanical damages, what guarantees the stability of the created thin-film after the deposition. What also makes the Al_2O_3 suitable for this application is the ability to being dissolved in both highly concentrated acids and alkalis⁷⁸. The Al_2O_3 etching allows for decreasing the thickness of the thin layer and for monitoring changes in the spectrum in real time. Since the RI of Al_2O_3 is higher than that of either the fiber core or the cladding⁵⁶, the coating simulates the real device by increasing the RI at the cavity surface, as is the case with biological film formation⁴.

5.1. THIN-FILM LAYER DEPOSITION

We deposited the Al_2O_3 films on the set of μ IMZIs and the reference silicon wafers in order to identify the response of the structures to a thin high-RI film on the cavity surface. We chose the ALD method to cover the microcavity evenly. We performed the deposition process using the Cambridge NanoTech Savannah S100 system according to the procedure described in⁵⁶. For the deposition process, water and trimethylaluminum (TMA, $\text{Al}(\text{CH}_3)_3$) precursors were used. The thickness of the Al_2O_3 film was controlled by the number of ALD cycles which reached approximately 1500 ($t \approx 150$ nm). The thickness and optical properties of the films

deposited on the reference silica wafers were determined using spectroscopic ellipsometry with a procedure described in⁵⁶. The deposition was followed by slow chemical etching of the film using 10 mM and 1M sodium hydroxide (NaOH) (Sigma-Aldrich) at 20°C for a specific time, and the optical response was verified after extensive washing of the cavity with deionized water. During the entire process, the μ IMZI transmission was monitored and analyzed following the procedure described in section 3.5. Before any NaOH processing, the cavity underwent 30 s long oxygen plasma processing (as described in section 4.1), that increased wettability of the surface of the highly hydrophobic film and made possible filling the cavity with the liquids⁷⁹.

5.2. EFFECT OF Al_2O_3 ETCHING.

Fig. 21 presents the influence of the etching process on the spectral response of the μ IMZI ($d = 40 \mu\text{m}$), coated with a film having a thickness of $t = 397 \text{ nm}$. Using spectroscopic ellipsometry on the reference sample, we determined that the deposition and etching rates of Al_2O_3 in 10 mM NaOH reach $\sim 0.1 \text{ nm/cycle}$ and $\sim 0.65 \text{ nm/min}$, respectively. In general, during the entire experiment, the transmission minima shift towards shorter wavelengths with a decrease in thickness of the thin film. The shift intensifies after $\sim 50 \text{ min}$ of etching and reaches 2 and 4.7 nm/min respectively for minima (I) appearing below 1220 and (II) above 1300 nm. It must be noted that the shift of minimum (II) is the highest there but because of its initial placement could not be monitored in the applied spectral range from the beginning of the experiment.

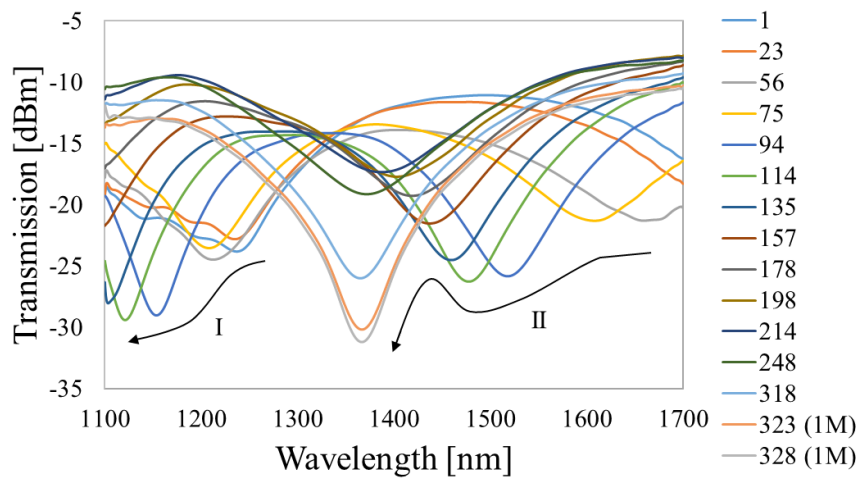


Figure 21. The response of the μ IMZI to Al_2O_3 film etching recorded for the water-filled cavity. The evolution of the transmission spectrum during the process in reference to the response before deposition

After ~120 min of etching, minimum (I) is no longer visible in the investigated spectral range, while minimum (II) slows down its wavelength shift and starts to significantly change its transmission curve. When the etching process exceeds ~180 min up to about 320 min, the spectral response changes very little. Hardly any etching effect was observable from the moment we increased the NaOH etching concentration to 1 M. That corresponds to an etching rate of more than 4 nm/min according to ellipsometric measurements made on the reference Si samples. For etching in this range there was no noticeable shift in wavelength, only a decrease in transmission by 10 dB towards the spectral response recorded before the deposition. In summary, the surface sensitivity is the highest for Al₂O₃ film thicknesses between 300 and 350 nm, where 1 nm decrease in the thickness corresponds to ~3 nm shift of the transmission minimum. The effect potentially allows for sub-nm monitoring of changes in thickness at the sensor surface.

5.3. THE INFLUENCE OF THE THICKNESS OF THE LAYER ON RI SENSITIVITY.

To estimate the influence of the thickness of the layer on bulk RI sensitivity, we measured the response of the structure to variations of RI at selected stages of the etching process. In general, the transmission minima shift towards shorter wavelengths during the measurements with different RI in (Fig. 22A) as it was in Section 3.5. Minimum (II) is observed in the RI range from 1.3330 up to 1.37 RIU, where for higher RI it shifts below the interrogated spectral range. Next, a minimum (III) appears at a longer wavelength and can be traced for RI above 1.37 RIU.

Based on these results we can see the significant influence of a thin film deposited inside the cavity on both the surface and the bulk RI sensitivity of the investigated μ IMZI (Fig. 22B). The thicker the Al₂O₃ film, the lower the bulk RI sensitivity, which varies from about 5,730 to 12,390 nm/RIU and 9,090 to 18,000 nm/RIU for transmission minima (II) and (III), respectively.

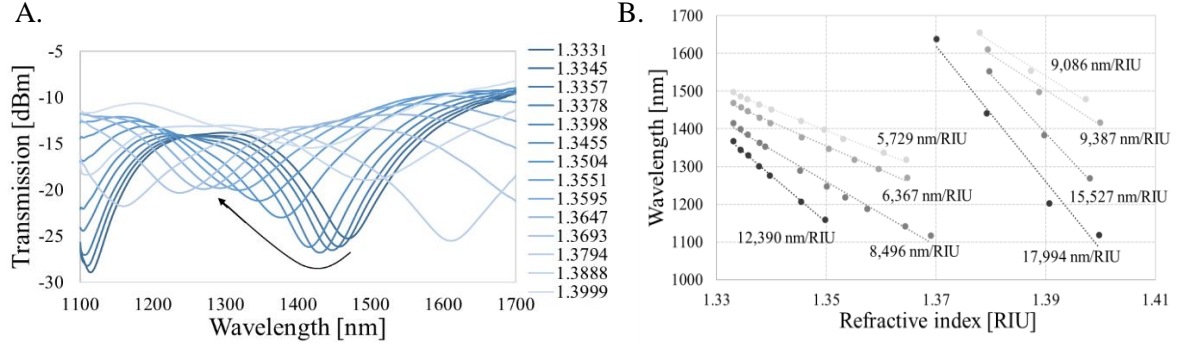


Figure 22. Effect of increase in RI of liquid in the micro-cavity for different thicknesses of the Al₂O₃ film, where A) shows a spectral response at a selected stage of the etching experiment and B) gives a summary of the measurements with determined sensitivity at each stage of etching.

5.4. COMPARISON OF THIN-LAYER DEPOSITION EFFECT TO CONTROLLED MICROFABRICATION OF SHALLOWER CAVITIES.

In order to verify whether the cavity depth induces the same effect as depositing a high-RI thin film, we made four μ IMZI structures ($d = 50 \mu\text{m}$) with spectral responses to water as shown in Fig. 23A. The only difference between them was their depth, where the deepest had the highest insertion losses.

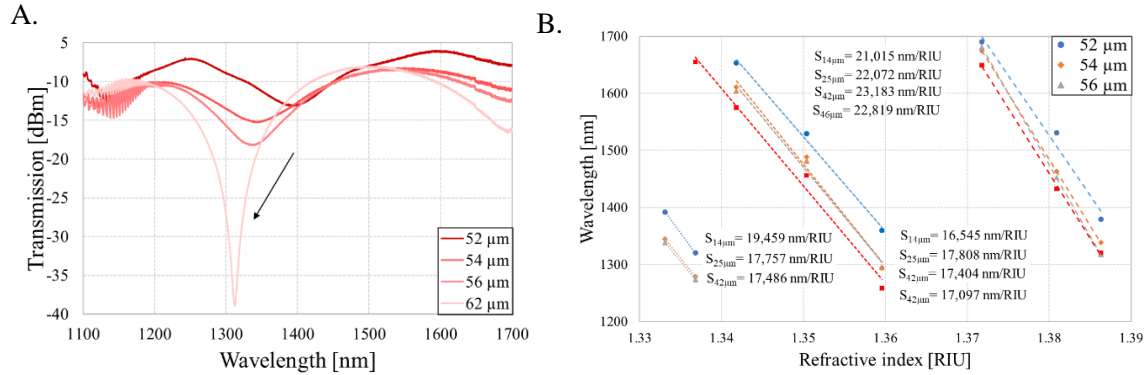


Figure 23. Influence of the cavity depth (different amount of fs laser runs) on spectral response to RI, where A) shows initial spectra for cavity filled with water and B) shows wavelength shift of minima with RI. The diameter of the cavity was $d = 50 \mu\text{m}$.

Increasing the cavity depth induces a spectral shift of the minimum towards shorter wavelengths. The effect regarding the direction of the shift corresponds to the decrease in the thin layer thickness. However, fabrication of more shallow cavities, which may correspond to a higher thickness of the deposited film, resulted in the complete absence of any transmission minimum, so obtaining results such as these shown in Fig. 21 was impossible when the cavity

had no film coating. Moreover, the depth of the cavity did not influence the bulk RI response as shown in Fig. 23B.

5.5. THEORETICAL EXPLANATION OF THE THIN-LAYER EFFECT

Based on the results we can conclude that increasing the RI in the cavity either by adding the a high-RI coating, or a liquid sample, produces opposite response, i.e., shift the spectrum towards longer, or shorter wavelengths, respectively. Following the analysis presented in Chapter 3, in particular the Eq. (4) describing the spectral location of the transmission minimum (λ_m):

$$\lambda_m = \frac{2\pi d \Delta n_{eff}}{(2m+1)\pi - \varphi_0}, \quad (4)$$

Where the difference between the effective RI of the two interfering modes can be presented as $\Delta n_{eff} = n_{co} - n_{cl}$, where n_{co} corresponds to the remaining part of the fiber core and n_{cl} to micromachined circular cavity. The diameter of the microcavity is described as d , and φ_0 represents the initial phase. The Δn_{eff} is the main component responsible for the spectral shift of the pattern (i.e., transmission minimum) and RI sensitivity. Two different effects can induce the changes in n_{eff} , though each of them affects Δn_{eff} differently.

When the liquid RI is increased, the propagation conditions are mainly affected by n_{cl} , and the characteristic minimum then shifts towards shorter wavelengths. In turn, when a high-RI film is deposited on the core surface, the n_{co} is affected while the n_{cl} generally stays unchanged, and the minima shift towards longer wavelengths. These circumstances explain why the measured responses to the surface and bulk RI are opposite and allow us to conduct further biosensing experiments and interpret their results.

Moreover, there is a certain range of the thickness of the thin-film where the sensitivity of the μ IMZI to the changes in the overlay is high. Within this range, any surface change, especially any change of the thickness, strongly impacts n_{co} yet has a negligible influence on propagation in the cavity. This unique range of thicknesses should be applied when high surface sensitivity is needed to detect sub-nm changes at the surface, like the presence of antibodies or peptides for instance.

5.6. CONCLUSIONS.

In this chapter, we show the capability of the μ IMZI for label-free detection and the first time the possibility of transition between bulk and surface RI sensitivity of the μ IMZI by application of thin high-RI film in the cavity. When there is no film in the cavity, the sensor is highly sensitive to the RI of liquid inside, and as already reported, can be used to investigate small volumes of liquids². In such working conditions, the sensor may only slightly react, mainly by a change in transmission, to the formation of the thin film on the cavity surface.

However, when a thin high-RI film of a certain thickness is deposited in the cavity, the device significantly responds with a wavelength shift to any variation of the thin film thickness. This response can be used to identify the presence of biological film growth. For these conditions, the bulk RI sensitivity is lower than for the uncoated μ IMZI. It is also to be expected that for thick biological films, such as bacteria-based films, change in the biolayer thickness can be investigated with no interfacial film.

THE BIOLOGICAL PART

CHAPTER 6

LABEL-FREE DETECTION OF LIVE *E. COLI* BACTERIA USING THE μ IMZI

This chapter presents the first study to date on selective label-free biosensing with the μ IMZI fabricated within an optical fiber. In contrast to studies of this sensing scheme, where only the sensitivity to refractive index changes in the cavity was investigated, this research used chemical surface treatment of the surface of the sensor to ensure detection specificity.

The work introduced in this section was partially presented in:

1. M. Janik, M. Koba, A. Celebańska, W. J. Bock and M. Śmietana, “Label-free detection of live *E. coli* bacteria using a microcavity in-line Mach-Zehnder interferometer.” *Scientific Reports* 8, 17176 (2018)

6.1. REVIEW OF BIORECEPTORS FOR BACTERIA DETECTION

Once the optimal device, sensitive enough to be applied for biosensing has been chosen, the next step is the choice of proper functionalization. While designing a functionalization of the device, the choice of the type of the bioreceptor remains a key element as it drives the efficiency and sensitivity of the assay. Ideal attributes of any recognition element are:

- high stability;
- low cost and availability;
- ease of design and reproducibility;
- ease of immobilization of the bioreceptor on the sensor surface and its stability;
- specificity towards the chosen target with minimum cross-reactivity towards different pathogens;
- proper orientation of the bioreceptor on the sensors' surface;
- covalent bond with bacteria surface;
- durability to external factors (e.g., Temperature, pH);
- long shelf-life;
- robust structure;

E. coli is a Gram-negative (G-) microorganism. These type of bacteria are characterized by their cell envelope (Fig. 24) which consists of three essential layers, namely the cytoplasmic (or inner) membrane, the periplasm, and the outer membrane. The outer membrane is a unique asymmetric lipid bilayer composed of phospholipids in the inner leaflet and lipopolysaccharides (LPS) and outer membrane protein (Omp) in the outer leaflet. Moreover, the appendices like flagella, fimbriae, and pili are anchored in the cell envelope. Except being a selective barrier crucial for the survival in many distinct environments, the outer membrane of bacteria is the host of a great variety of molecules acting as receptors in the interactions with

the external environment. Knowing the structure of outer membrane allows choosing the best suitable and specific biorecognition element.

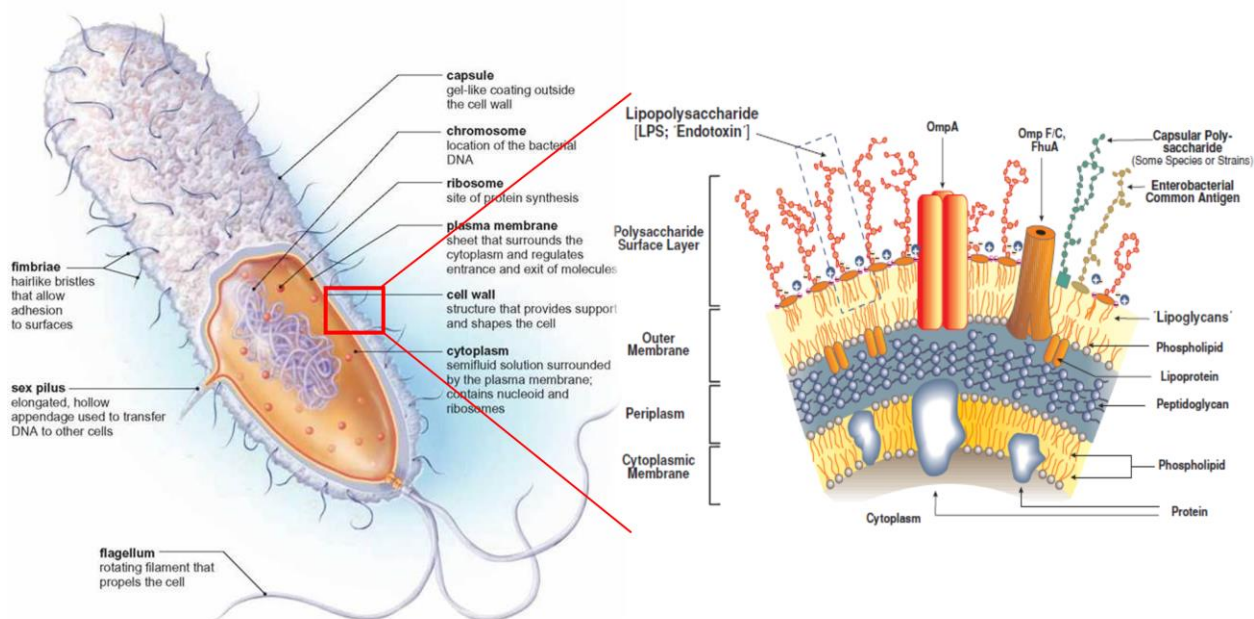


Figure 24. Schematic representation of the Gram-negative bacteria and their cell wall.

To date, a broad spectrum of bioreceptors has been used for bacterial detection including antibodies, sugars/lectins, proteins, aptamers, and phages.

6.1.1. ANTIBODIES

Immunosensors using antibodies as bioreceptors have been regarded as a gold-standard technique in clinical diagnostics and environmental monitoring⁸⁰. Antibodies (Ab), also known as immunoglobulins (Ig), are large, “Y-shape” proteins of ~150 kDa molecular mass and with dimensions approximately $14 \times 10 \times 4$ nm⁸¹. They are produced by the host immune system to identify and to neutralize pathogens such as bacteria or viruses or prepare them for uptake and destruction by phagocytes. Each antibody molecule has a unique structure that enables it to bind specifically to its corresponding antigen. Their popularity arises from several advantages such as high specificity, and versatility. Since they are soluble and secreted in large quantities, antibodies became key affinity ligands for pathogens detection in food and clinical samples. Thanks to the ease of integration into different systems, Abs were combined with numerous sensor formats including electrochemical, optical, and mass-based biosensors⁸².

Abs production is based on the injection of the inactivated pathogen into a suitable animal host, e.g., mouse, rabbit, goat or sheep. Once they are synthesized, the immobilization process becomes crucial for system efficiency. The control over the position and orientation of Abs during the covalent binding is challenging, and it affects efficiency and sensitivity of the sensor. In an ideal scenario, antibodies should be immobilized in their native form, without the need for introducing functional groups or special tags/labeling, and should be oriented to maximize complementary binding. To date, no method genuinely provides the ideal scenario⁸³. Antibodies suffer from few more drawbacks, which limit their utilization as biorecognition elements. Though antibodies are produced to be specific to a bacterial membrane, nonspecific binding of the antibodies is indeed always present⁸⁴. Depending on the target, antibodies can provide different immobilization efficiency of the detected pathogen⁸⁵. Moreover, they are prone to physical, chemical, and enzymatic damages, therefore they have to be stored and manipulated with extra care⁸⁶.

6.1.2. BACTERIOPHAGES

Bacteriophages are viruses that infect a bacterial host and regarding the lack of their metabolic machinery, replicate only within the bacteria. As obligate bacterial parasites, phages can be found in all reservoirs populated by bacterial hosts, for example in soil⁸⁷, in aquatic environments⁸⁸, and even in the human gut⁸⁹, what makes them easy to isolate and cost-effective. Most phages possess a highly specific mechanism to recognize the strain level of the bacterial host. To initiate infection, the phages need to adsorb to the host surfaces, to penetrate cell walls and to inject genetic materials into the host using their special tail structure. Tail proteins of these phages are diverse and capable of recognizing almost every host surface component, e.g., surface proteins, polysaccharides, and LPS⁹⁰.

Bacteriophages may replicate within a lytic (T4 phage) or a lysogenic (MS2 phage) cycle. For lytic phages, after their attachment to the surface of the host cell and its infection (injection of the phage's DNA/RNA), the phage genome remains separate from the host DNA and immediately replicates. As soon as new phage proteins are made, and new phage particles are assembled, the bacterial cells are lysed (destroyed) releasing new virions. In contrast, the lysogenic cycle does not result in the immediate destruction of the host cell. The viral genome integrates with the host DNA and replicates along with it harmlessly.

The bacteriophage remains dormant until host conditions deteriorate, for instance due to depletion of nutrients, temperature increase, or UV radiation. Under these circumstances phages become active and initiate the reproductive cycle, resulting in lysis of the host cell.

Bacteriophages are stable, have a long shelf-life, and can detect their hosts in a wide range of pH and temperatures. Nonetheless, they may lose their viability if they are drying after immobilization on a surface⁹¹. Moreover, utilization of the whole phages as biorecognition elements can result in the unstable measured signal as phages retain their lytic activity.

6.1.3. PHAGE RECEPTOR BINDING PROTEINS (ADHESINS)

The relatively large size of bacteriophages can be a problem for some biosensing applications. Their fragile and complex structure makes well-oriented immobilization of the phages on the sensors' surface difficult, as it is in case of the T4 phage. Therefore, instead of using the whole phages, just the phage receptor binding proteins (RBPs) located on the tail fibers can be applied. RBPs are responsible for the unique host-specific recognition, and for triggering the transfer of the phage' genetic material into the host⁹². One of the biggest advantages of the RBPs is the possibility of introducing changes to their sequence. Suitable tags can be added at an appropriate position without altering and disturbing their binding affinity and can also be exploited for better orientation of RBPs on the sensor surface⁹¹. One of the reported RBPs for label-free bacteria and bacterial LPS detection is adhesin gp37^{4,5} obtained from phage T4.

In comparison to antibodies, the RBPs offer better stability; however despite many advantages, phage proteins are not yet often used in biosensing applications. One of the reasons is that just a few of them are well characterized. Although in contrast to the phages, the RBPs can be obtained in large quantities with no bacterial contaminations, their preparation includes many time-consuming and complicated steps.

6.1.4. APTAMERS

An aptamer is a short (from 25 to 90 bases⁹³), single-stranded nucleic acid sequence (DNA or RNA), which can attach to a variety of targets like proteins, viruses, cells, nucleotides, drugs, or even heavy metal ions. They can be selected by an in vitro method "Systematic Evolution of Ligands by EXponential enrichment" (SELEX)^{94,95}. Thanks to their three-dimensional

structure, the aptamers can bind the target with high efficacy and specificity. Since their discovery, aptamers gained attention and have been regarded as the nucleic acid analogs of antibodies⁹⁶. However, the affinity of aptamers to their targets is comparable to, or even higher than monoclonal antibodies, what may be caused by aptamer's capability of folding upon binding target⁹⁷. Further improvement of binding efficiency can result from higher surface density and diminished spatial blocking⁹⁶. In addition to the advantages mentioned above, some unique attributes of aptamers make them competitive tools over natural antibodies in a variety of biosensing assays.

First of all, once the sequence is obtained, aptamers can be easily chemically synthesized with high reproducibility and purity from commercial sources. There is no need for complicated and expensive purification steps⁹⁸, and, they provide exceptional flexibility and convenience regarding the engineering of their structure. The structural modifications have led to the development of aptamers with enhanced affinity, specificity, and stability⁹⁹. That allows creating a molecule with additional properties such as nuclease resistance, which is crucial for applications in media like blood.

Nonetheless, if additional features and changes were introduced after the selection, it is crucial to ensure that affinity to the target has not been interrupted. In contrast to antibodies, aptamers are structurally stable across a wide range of temperatures and storage conditions. They can be exposed to high ranges of temperatures without being denaturated and degraded. They can simply refold when the temperature goes down¹⁰⁰.

Due to their outstanding binding characteristics, stability and possibility for easy modifications, aptamers have all the necessary qualities to be used as the basis of detection elements. They were used to detect pathogens like *E. coli*, *L. monocytogenes*, *S. enterica*, or *S. aureus*^{94,95,101}. Surprisingly, despite the availability of aptamers recognizing a wide range of pathogens, a relatively low number of them have yet been used in biosensing.

6.1.5. PHAGE DISPLAY PEPTIDE APTAMERS

Peptide aptamer is a term created by analogy to DNA/RNA. Unlike DNA/RNA aptamers, peptide aptamers are combinatorial protein reagents instead of nucleotides. They are formed by natural or synthetic short polymers composed of 6 – 20 amino acids which are linked by

peptide bonds¹⁰². Considering that peptides with short chains of amino acids generally have better chemical and conformational stability than proteins, they can be an excellent substitution for adhesins. Peptide aptamers show similar molecular recognition properties to antibodies. They can specifically recognize a variety of both biological objects (proteins, pathogens, cancer cells) and a wide range of nonorganic substances (metals and alloys, semiconductors, toxins)¹⁰³.

Based on their characteristics, in particular high stability and solubility, the possibility of chemical synthesis, easy structural modifications, large chemical versatility, they certainly have the advantage over the antibodies¹⁰³. Thanks to features such as small size, rapid folding properties, and high yield of bacterial expression the peptides outstand other types of the receptors. The absence of disulfide bonds and intramolecular cysteine residues enables intracellular applications and gives a possibility of labeling or performing other chemical modifications, what, in turn, provides their proper orientation on the sensors' surface¹⁰⁴.

Although the advantages of peptides over antibodies are evident, it is hard to compare peptides with oligonucleotide aptamers. Few things are particularly remarkable about the peptides. They possess a variety of functional groups (not present in the nucleic acids), which can enhance interactions and thus the affinity with the target. One of the examples is the formation of hydrogen or electrostatic bonds and different base-acid behavior. The more rigid backbone of the peptide aptamers compared to DNA/RNA aptamer may also be an important advantage¹⁰⁴. Peptides can be obtained by screening and optimizing of the artificial peptide libraries. Phage display is currently one of the most common techniques to search for peptide ligands¹⁰⁵.

Peptide-based sensors have been developed at a rapid pace particularly in the last two decades and have shown great potential to be applied in various fields. One of the first examples of phage display application for bacteria detection was published in 2006¹⁰⁶.

6.1.6. CARBOHYDRATES AND LECTINS






The detection of pathogenic bacteria can also be carried out via protein-carbohydrate interactions, which are similar to the antibody-antigen, or to enzyme–substrate reactions. This recognition pattern is involved in a wide variety of processes including the immune response, adhesion, and viral or bacterial infections. For instance, to accomplish adhesion and

to initiate infection process bacteria have to bind complementary carbohydrates on the surface of the host tissues. To bind the target bacteria utilize cellular lectins located on slender hair-like appendages called pili/fimbriae, which can be considered as bacterial virulence factors. To emphasize the importance of the lectin-carbohydrate interaction it is worth to mention that the lectin-deficient mutant bacteria very often fail to initiate infection¹⁰⁷.

Due to the presence of hydroxyl, amine, and carboxyl groups, carbohydrates are mostly only capable of forming hydrogen bonds and hydrophobic interactions. Since the lectins possess shallow binding pockets, the individual interaction of carbohydrates-protein are generally very weak¹⁰⁸. To overcome their weak affinity, lectins bind multiple oligosaccharide epitopes. It seems evident then that carbohydrate-protein recognition has low specificity and many other proteins can recognize the carbohydrate ligands giving false positive results¹⁰⁹. Without proper conditions, e.g., due to the lack of the magnesium and calcium ions, the lectin-based systems lack stability and have short lifetimes, thus requiring a replenishment.

Despite these disadvantages this model has been combined with numerous sensor formats. Mainly due to the ease of integration into different systems and availability of the carbohydrates, they were integrated with electrochemical, optical, and mass-based biosensors for bacteria detection¹¹⁰.

TABLE 4
COMPARISON OF ANALYZED BIORECOGNITION ELEMENTS (* depending on the type of bacteriophage)

Attributes of an ideal recognition element	    				
	Phages	RBPs	Antibodies	Aptamers	Peptides
Specificity towards the chosen target with minimum cross-reactivity towards different pathogens	✓	✓	✓	✓	✓
Ease of design and reproducibility	✱	✓	✗	✓	✓
Low cost and availability	✓	✗	✗	✓	✓
Proper orientation of the bioreceptor on the sensors' surface	✱	✓	✗	✓	✓
Ease of immobilization of the bioreceptor on the sensor surface	✓	✓	✓	✓	✓
Covalently binding the bio-receptor on the bacteria surface	✓	✓	✗	✗	✓
Durability to the external factors (e.g., Temperature, pH)	✓	✓	✗	✓	✓
Robust structure	✱	✓	✗	✓	✓
Long shelf life	✓	✓	✗	✓	✓
Immobilization doesn't affect on working/activity	✱	✓	✗	✓	✓
The undisturbed structure after immobilization on the sensors' surface	✓	✓	✗	✓	✓

Considering all the pros and cons of the bioreceptors above (Tab. 4), two types were chosen for further experiments: MS2 lysogenic phages and peptide aptamers.

6.2. LABEL-FREE DETECTION OF E. COLI C3000 BACTERIA WITH MS2 PHAGES

When early and fast diagnosis is required, the best way to identify the pathogenic strain of bacteria is direct detection of the whole bacteria cells, rather than of the isolated biological components like enzymes¹¹¹, LPS⁵, or OMP¹¹².

This approach has several advantages:

- whole cells are more tolerant of environmental changes such as temperature, pH, than the isolated structures;
- isolation of whole microorganisms from natural sources is very easy;
- there is no need for extensive preparation of the sample before measurements.

As discussed in section 6.1, to adopt a device for pathogen detection, the sensor's surface must be specially modified. From a broad spectrum of bioreceptors, based on our research and

presented comparison (Table 4), we decided to work with MS2 bacteriophages as the first choice of a recognition element.

MS2 phage is a member of the Leviviridae family, which infects male *E. coli* cells via attachment to their F-pilus, as shown in Fig. 25. The infective MS2 virion is composed of a coat protein, a maturation (or A) protein, and a single-stranded molecule of RNA¹¹³. The coat protein is a major component of the MS2 protein shell, and in conjunction with protein A the molecule forms the 275 Å (~27.5 nm) MS2 virus (Fig. 26)¹¹⁴. Its simple structure assures that the phage is well-oriented on the fiber surface, what is very challenging to achieve in the case of the T4 application. Due to the lysogenic cycle of MS2¹¹⁵- which does not result in immediate destruction of the host cell in comparison to the action of the T4 phage – the stability of measurements is assured at controlled conditions. Through protein-A which is a receptor binding with bacteria pilis, MS2 does not have to reach for the bacterial cell surface, facilitating a quick bacterial capture and reducing the time of the detection¹¹⁶.

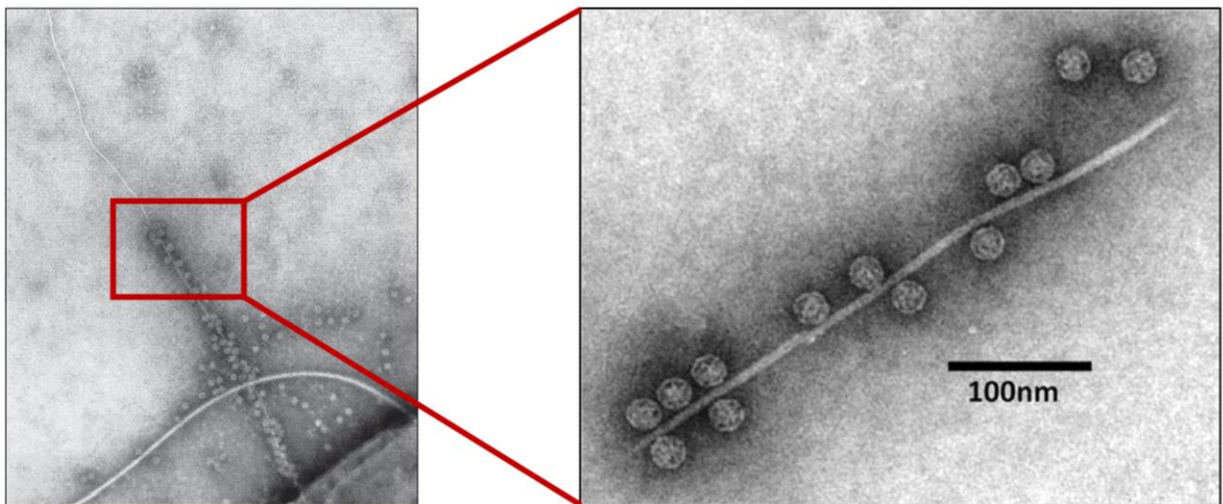


Figure 25. A TEM image of pilus-associated MS2 phages. The long rod-shaped structure is the pilus. The length and thickness of pilus in this image were about 430 and 6 nm, respectively¹. Micrograph of an F-pilus emerging from an *E. coli* cell that is covered with icosahedral MS2 phage particles.

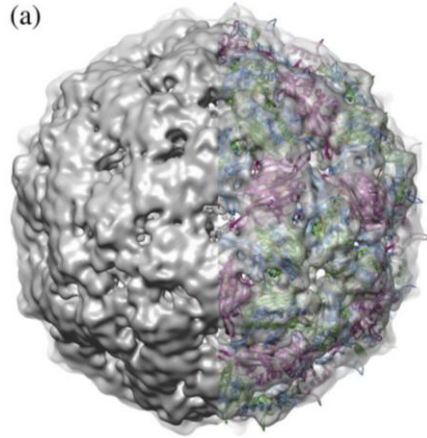


Figure 26. The structure of the wild-type bacteriophage MS2 virion¹¹⁷

6.2.1. BACTERIA DRY-WEIGHT SENSING.

To facilitate the detection process and to check the efficiency of the chosen bioreceptor we perform preliminary experiments with lyophilized (dry-weight) *E. coli* C3000. One of the most significant differences between live bacteria and bacteria dry weight is that the lyophilized cells have no motility. During measurements, along with the incubation the cells simply sediment and aggregate on the sensor surface. Thus, it makes it easier to detect them than the live, motile pathogens.

As shown in Section 3.5, the spectral response of the μ IMZI strongly depends on the RI filling the microcavity. That is why the measurements in PBS (after extensive washing of the cavity) followed each step of the biofunctionalization. The purpose of washing was to remove the biological residues which were only physically attached to the functionalized surface and could have a disturbing impact on the measurement. To achieve the comparative shift of the transmission minima, only the measurements performed in the same solution (here PBS) were compared.

Fig. 28 presents the transmission spectra obtained for each stage of the experiment, namely:

1. Functionalization of the surface – silanization with APTES (gas phase, blue curve), where the process was controlled by its exposure time and the amount of the precursor, followed by activation of the deposited amine groups by glutaraldehyde (GLU, grey curve);
2. Immobilization of bioreceptor – MS2 phages – and blocking the surface with BSA solution (red curve);
3. *E. Coli* C3000 bacteria detection: incubation of the sensor in bacteria solution (green, double curve) and bacteria attached to the surface (blue, dashed curve).

For the cavity filled with PBS the stage (1) can be considered as a baseline.

A schematic representation of the biofunctionalization process is shown in Fig. 27. Further details about this functionalization process can be found in Appendix C.

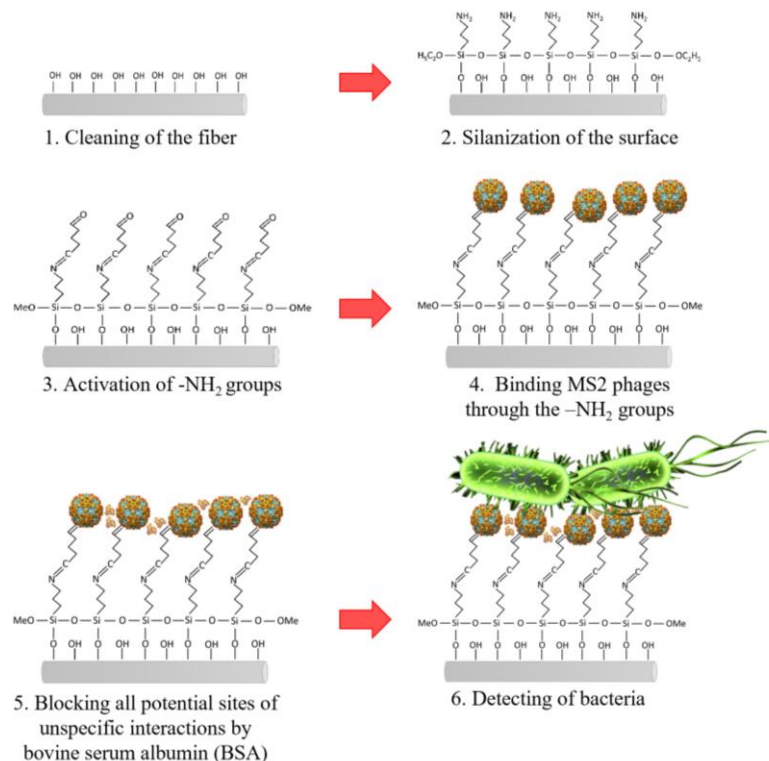


Figure 27. Schematic representation of the μIMZI biofunctionalization process.

The thick layers of silane are very fragile and may be washed away either in the presence of a buffer or during various washing steps in an assay process what has been reported in¹¹⁸. Therefore, the functionalization process was optimized to obtain a thin and stable silane/GLU layer, that could not change the working conditions of the μIMZI (no spectral shift of the pattern after the functionalization was noticed). On the other hand, the introduction of the highly concentrated phages (10^9 plaque forming units (PFU)/mL) (stage 2) with an average RI equal to 1.217 RIU¹¹⁹ changed the working conditions of the μIMZI through the formation of low RI adlayer, and thus significantly affected the n_{co} . The presence of tens of nm thick layer had a significant influence on the spectrum. The minimum (λ_m) strongly shifted towards lower wavelengths and decreased in depth from -23 dB before phages immobilization to -17 dB after the process. A similar effect can be observed in Fig. 28B, which shows how an additional layer caused a decrease in the intensity of the transmission.

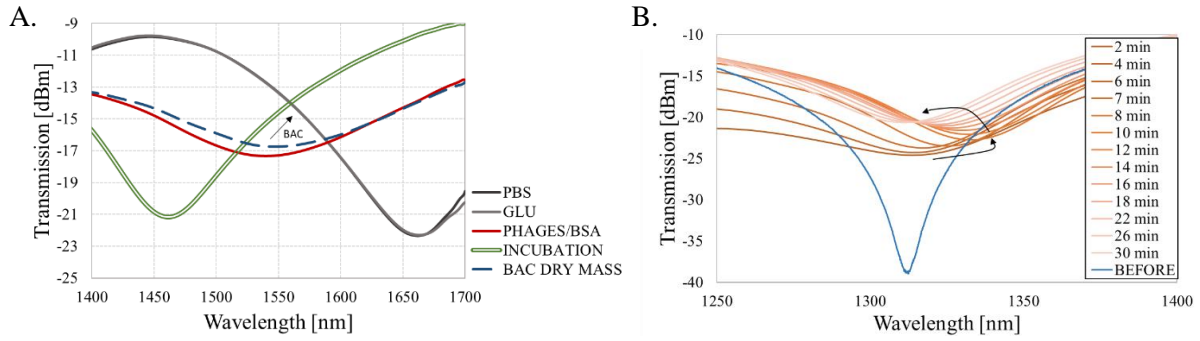


Figure 28. A) Transmission spectra of the μ IMZI at each stage of the experiment with *E. coli* C3000 (1 mg/mL) dry weight. The arrow indicates the change induced by bacteria binding. B) Transmission spectra of the μ IMZI with the cavity diameter $d = 50 \mu\text{m}$ during the evolution of the Al_2O_3 film thickness (initially $t = 154 \text{ nm}$) with its etching process recorded for a water-filled cavity. The spectrum before the deposition is given for reference. Arrows indicate the shift of the minimum induced by each procedure.

During the blocking step, the introduction of dense blocking solution (2 mg/mL) filled empty spaces and prevented an unspecific binding from happening, but did not introduce any further changes to λ_m . This may be caused by the very small size of the BSA molecules and an already uniform (dense) layer of phages. After the sensor surface functionalization, the device has been exposed to bacteria dry weight (1 mg/mL) (stage 3). As can be seen in Fig. 28A, the minimum shifts 7 nm towards longer wavelengths (the shift is designated by a blue, dashed line).

The observed change induced by bacteria cells was obtained after extensive washing with PBS. We concluded therefore that the shift must have been influenced by the growth of the specific adlayer on the microcavity surface, not by a change in the RI of the solution as observed during incubation of the sensor in the bacteria solution (designated by the double green line).

6.2.3. DETECTION OF LIVE *E. COLI* C3000.

On the top of the lack of mobility, there are also some other differences between the dead and live microbes which can have an impact on performance of the measurement. After lyophilization, heat treatment or ultrasonication, the structural properties of bacteria cells are changed. Together with dehydration, changes may occur in the shape of the bacteria cell and in some of the surface structures, especially pili or fimbria, which are very important in the case of MS2-based detection. As a result, it is impossible to determine what in fact has bonded to the surface – the whole bacteria cells or some detached elements. Furthermore, during the sample preparation of dead microorganisms, bacteria cells can be destroyed, causing the release of their internal structures such as proteins. This can also affect the optical responses.

To imitate bacteria detection in their natural environment, we experimented with the live bacteria. Vivid bacteria are motile, in their proper shape and equipped with all the usual surface structures, what makes the measurements even more challenging. A biolayer formed by the live cells typically has different properties than the layer created by bacteria dry-weight, including those optical. For example, it may contain air gaps due to the presence of fimbria/pili on the surface which may hold the surface of the cells at a distance from the μ IMZI bottom. Since the immobilized MS2 are bound to the pili, this causes no problems when capturing bacteria and keeping them on the μ IMZI surface. However, the layer can never be as dense and uniform as a layer formed by the immobilized, dead bacteria or bacteriophages. Also, the layer can scatter the light through the extremely rough surface of bacteria, what can lead to the additional losses.

The experiments were carried out according to the following procedure.

The μ IMZI sensor with the MS2 phages immobilized on the surface was used to detect some different concentrations of live *E. coli* C3000 strain. Bacteria dilutions having concentrations of 10^2 , 10^4 , 10^6 , 10^7 and 10^8 CFU/mL in PBS were prepared. For selectivity measurements, a negative sample containing *B. Thailandensis* was prepared with a concentration of 10^8 CFU/mL. The description of the detailed bacteria preparation procedure can be found in Appendix B.

During the experiments, the sensor was immersed in the solutions of increasing concentrations of specific *E. coli* strain for 30 minutes for each concentration. After the bacteria incubation, the sensor has been extensively washed and measured in PBS to obtain its reference results. The difference between the wavelengths corresponding to the transmission minima after BSA binding and after each exposition to bacteria was defined as the sensor response. The spectra obtained at each stage of the experiment are shown in Fig. 29.

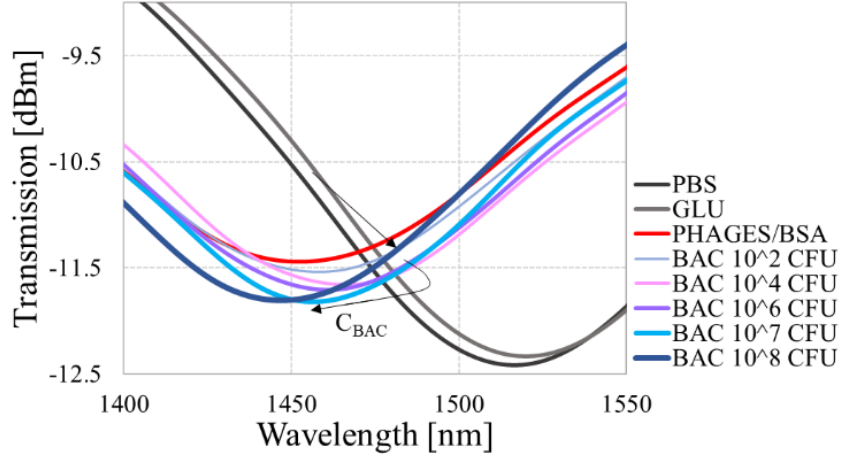


Figure 29. The response of the μ IMZI where the transmission spectra in PBS at each stage of the experiment with different concentrations of live *E. coli* C3000 bacteria after incubation and extensive washing.

Even for the concentration of bacteria as low as 100 CFU/mL, a 5.9 nm spectral shift can be observed. Especially noticeable is the fact that the spectrum shifts differently than during the experiment with dead bacteria, what could be expected due to the differences in the biolayer properties.

Subsequent additions of the solutions with a higher concentration of *E. coli* C3000 caused further changes to the wavelength of the transmission minimum. It is worth reminding that the depth of the micromachined cavity is $\sim 62 \mu\text{m}$, so it is $\sim 4 \mu\text{m}$ inside the core. Hence, a layer with the thickness of 4-5 μm will affect n_{co} the most, creating new conditions for the light propagation inside the core. Further growth of the layer exceeding the 4 μm thickness negligibly changes n_{co} , but, in contrast, affects n_{cl} . Considering that the size of bacteria spans is equal to $\sim 2 \mu\text{m}^{115}$ and the length of the fimbriae is $1 \mu\text{m}^{120}$ – the bacteria layer is the thickest one in the system. Adding the bacterial solutions with a concentration of up to 10^4 CFU/mL shifted the spectrum towards the longer wavelengths. Knowing that the RI of bacterial solution stays equal to 1.388 RIU¹²¹ we therefore expected at this stage of the experiment that the n_{co} is mainly affected.

According to the MS2 infection cycle and its attachment to the bacterium, we need to take into account that the layer of *E. coli* formed on the sensor surface can increase its density and thickness. Further growth of the adlayer, especially after incubation at a higher concentration of bacteria, affects mainly n_{cl} . Under these conditions and according to the Eq. (4), the

minimum's shift changes its direction towards shorter wavelengths. It is in agreement with the previously presented response of the sensor to the increase in Al_2O_3 film thickness (Fig. 28B), where the response followed the same non-monotonic pattern.

Despite the non-monotoneous response and the initial position of the minimum, several trials revealed the same trend of the shift of the minimum. For concentrations as small as 10^2 - 10^5 CFU/ml we observed a gradual shift of the minimum towards longer wavelengths and an increase of its depth. For higher concentrations - 10^6 - 10^8 CFU/ml - the direction of the shift has changed towards shorter wavelengths, but its depth kept increasing. With a combination of these two parameters, i.e., the minimum's wavelength and the transmission, the distinction between different concentrations of bacteria is possible (Fig. 30A). Furthermore, if we integrate the transmission and the wavelength in the way to get a monotonic function, it is possible to obtain an unambiguous mapping of the two values to specific bacteria concentration. An example of such a linear combination can be Eq. 7:

$$f = A \cdot \text{Wavelength} + B \cdot \text{Transmission}, (7)$$

where A and B are scaling factors expressed in $[\text{nm}^{-1}]$ and $[\text{dBm}^{-1}]$, respectively. These factors transform the wavelength and transmission into the same range and guarantee consistency of the units. The function given in Eq. 7 with appropriate coefficients simplifies recognition of the bacteria concentration. As an example, if we substitute $A = 0.005$ and $B = 1$, the outcome is shown in Fig. 30B.

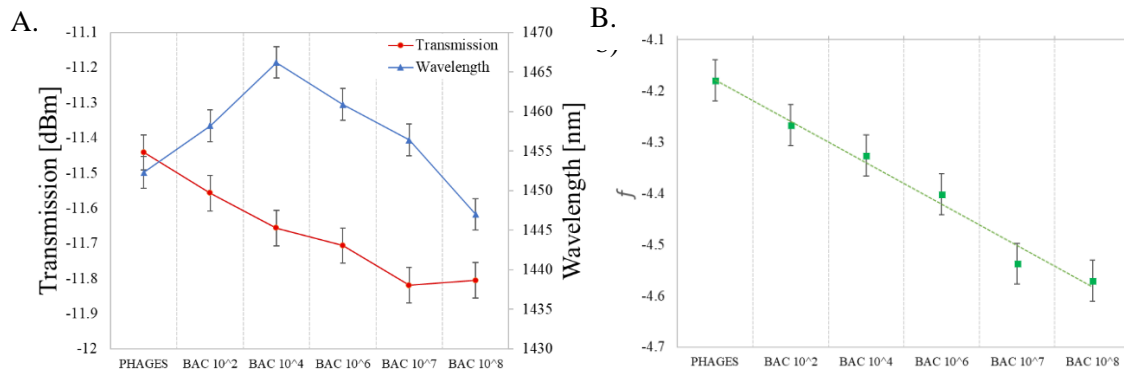


Figure 30. The response of the μIMZI where A) shows a correlation between the transmission and the wavelength; B) shows a linear combination between the transmission and the wavelength.

To assure that the obtained effects come from the formation of the biological layer and not from the changes of the RI of the solution, the wavelength of the minimum after each stage of the biofunctionalization is plotted in Fig. 31. Due to higher n_{cl} present in the cavity during the functionalization process, such as during an incubation with GLU, the spectrum temporary experiences a shift towards a lower wavelength. We can observe the same effect during the incubation using phages, or higher concentrations of bacteria (10^7 and 10^8 CFU/mL). After an extensive washing of the surface with PBS, the signal is changed, revealing the influence of the adlayer.

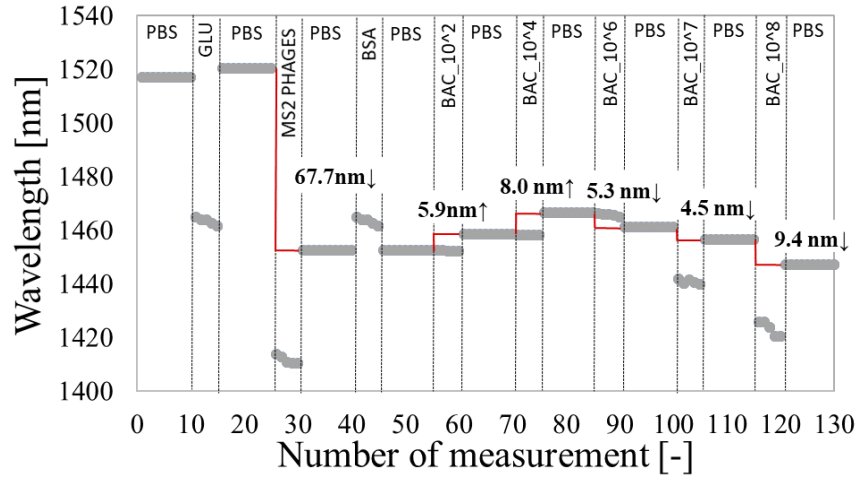


Figure 31. A shift of the minimum's wavelength at each stage of the experiment induced by functionalization and incubation in different concentrations of live bacteria.

The described sensor has shown superiority over the other fiber-optic platforms regarding sensitivity, easiness of fabrication, and the volume of the sample required to conduct the measurements. Similar assay strategies using APTES/GLU surface functionalization and phages were used for detection of other *E. coli* strains by employing LPFG^{3,6}, FBG¹²², and multimode microfiber probe¹²³. Although the detection limit of these probes reached 10^3 CFU/mL, the sensitivities of those platforms were lower. A similar strategy using antibodies as a biorecognition element was used to detect other *E. coli* strains by employing a plastic optical fiber¹²⁴. It resulted in a LOD of 10^3 CFU/mL with a detection time of 10 minutes per sample, but a sample volume required for the measurements was equal to 5-6 ml. The U-bent fiber optic probe¹²⁵ using immobilized antibodies was also developed for *E. coli* detection and resulted in

a LOD of 10^3 CFU/ml, using 500 μ l of the sample per measurement, whereas our method was capable of detecting 100 CFU/ml in over ten times smaller volumes.

6.2.4. NEGATIVE CONTROLS.

During the adsorption-based measurement, one might expect the *E. coli* bacteria to be easily wiped off the surface by the subsequent PBS buffer washes. In the described experiments, however, they remained firmly attached to the fiber surface due to the well oriented, immobilized phages. The spectral shift was therefore influenced mostly by the change of the thickness of the specific biolayer on the μ IMZI surface. To prove this point, two negative control experiments were performed. First, to verify the selectivity of the bioreceptor, we used the *B. Thailandensis* strain, which shows no affinity to MS2. The second control experiment was performed with no MS2 phages but using the host C3000 solely. This second experiment aimed to show that without a specific biorecognition element on the surface it is impossible to detect live bacteria just by exposing the biosample to the functionalized surface.

It is clear that the spectral minimum during the bacteria incubation significantly shifts towards shorter wavelengths (green double curves) in both experiments. This is attributed to the high RI of the highly concentrated bacteria solution (10^8 CFU/mL). However, after several washes in PBS, and despite a very high concentration of the bacteria samples, no wavelength shift was observed, indicating that no interaction and no specific binding occurs on the surface.

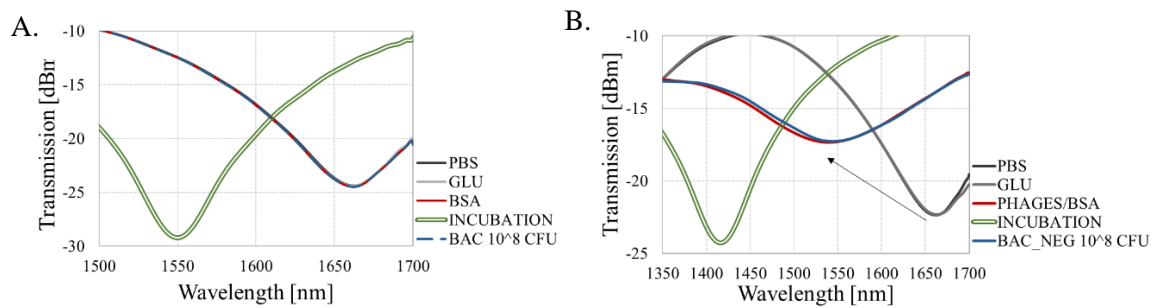


Figure 32. Transmission spectra of the μ IMZI at each stage of the experiment, showing the response A) for positive *E. coli* C3000 without phages on the sensor's surface and B) for negative *B. Thailandensis* with MS2 phages.

6.2.5. CONCLUSIONS.

In this section, we show for the first time the capability of biofilm growth monitoring using a μ IMZI-based biosensor. The effect has been shown as a result of exposing the functionalized biosensor to different concentrations of live bacteria. When using MS2 bacteriophages as recognition elements, the reported device allows for stable and specific label-free detection of alive *E. coli* C3000, in addition to its high RI sensitivity (over 15,000 nm/RIU). The limit of detection for these real-time measurements is as low as 100 CFU/mL. The reliability of the functionalized sensor was confirmed with two negative control experiments.

Based on these results, it can be concluded that the spectral response occurs due to the phenomena taking place on the surface of the sensor, and not due to the changes of the RI of the analyte. During the experiments, we observed the effects of the transitions between surface- and volume-related effects. We believe that the non-monotonic trend in the spectral responses was a result of the investigated working point of the μ IMZI as well as the thickness of the biolayer. Due to its high RI sensitivity, low-temperature sensitivity and to its ability to investigate small sub-nanoliter volumes, the sensor is well suited for biological and chemical analysis.

6.3. LABEL-FREE DETECTION OF PATHOGENIC E. COLI O157:H7 BACTERIA WITH PEPTIDE APTAMERS

Cell surface recognition as well as new scaffold that recognizes a chosen structure like bacteria, is an important topic in biosensors' research. Such compounds can also be used in therapeutic and diagnostic applications. One of the methods which allow a new ligand to interact with the cell surface, or any other ligand directly is Phage Display. For the past 28 years, phage display technology has been valuable tool for a myriad of applications, including mapping of epitopes and of protein-protein interactions.

With the increasing number of phage display collections, numerous new applications have emerged. Also, the phage display libraries have been used along these lines to discover:

- anti-microbial/viral peptides,
- material-specific peptides,
- small molecule binders,
- novel enzyme substrates,
- bioactive peptides through in vitro and in vivo panning approaches.

Phage display is currently one of the most common techniques to search for peptide ligands¹⁰⁵. This technology described in 1985 by G.P. Smith¹²⁶ is based on the fusion of the gene encoding the peptide with the phage surface protein-encoding gene. The molecule corresponding to the gene sequence is displayed on the surface of a phage virion. A phage library composed of 10^9 elements, where each one displays a different peptide on the coat, can be identified by affinity selection – called biopanning¹⁰⁰ (Fig. 33). Three to five rounds of biopanning are usually performed, where a display library is incubated with the target, and followed by extensive washing to remove the unbound phages. The tightly bound phages are eluted and enriched by amplification in the host cell. Then, the sequence of the peptide can be determined by sequencing the DNA of individual clones¹²⁷.

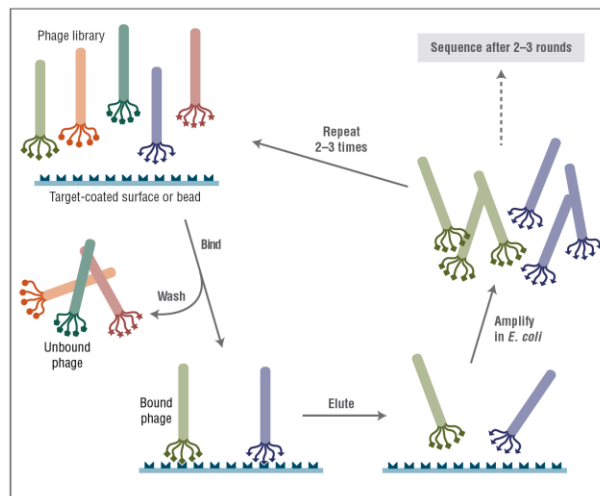


Figure 33. Whole cell-based panning protocol.

Even though the phage display has great potential as a peptide selection method, it is still a newcomer in the detection area, and until nowadays was focused mostly on the development of medicinal preparations and on studying molecular recognition in the biological systems. The peptides selected through this method have been successfully used for the detection of toxins^{128,129} and identification of *Bacillus anthracis*¹³⁰, *Pseudomonas aeruginosa*¹³¹, *Salmonella Typhimurium*¹³², *Staphylococcus aureus*^{133,134}. Although the specific and high-affinity peptides have been demonstrated to be superior over the antibodies, up to our knowledge they were never applied as a bioreceptors for bacteria detection on a fiber optic platform.

6.3.1. BIOPANNING OF *E. coli* O157:H7 WITH PHAGE DISPLAY LIBRARY

The bacteria strains: *E. coli* O157:H7 and *B. Thailandensis* used in the experiments were obtained from the INRS-Institute Armand-Frappier.

E. coli ER2738 and M13 phages were part of Phage Display Peptide Library Kit (New England BioLabs Inc.) Peptide aptamers were selected at Ludwik Hirszweld Institute of Immunology and Experimental Therapy, Polish Academy of Science in Wrocław under the supervision of dr. Ewa Brzozowska. The sequencing of the chosen peptides was performed by the Genomed company. The synthesis of the chosen peptides was performed by Bio Basic Inc.

To identify the peptides that bind to *E. coli* O157:H7, we screened the Ph.D-7 Phage Display Peptides Library. After three rounds of biopanning, amino acid sequences encoded by the inserts revealed two *E. coli*-binding peptides. They were the result of consensus sequences represented by nine and four clones for PEP-1 (ISTTLFP) and PEP-2 (DNDLSLS), respectively. Figure 34 presents sequences and 3D visualizations of the obtained heptapeptides. Further details about the biopanning of *E. coli* O157:H7 with phage display library can be found in Appendix.A.

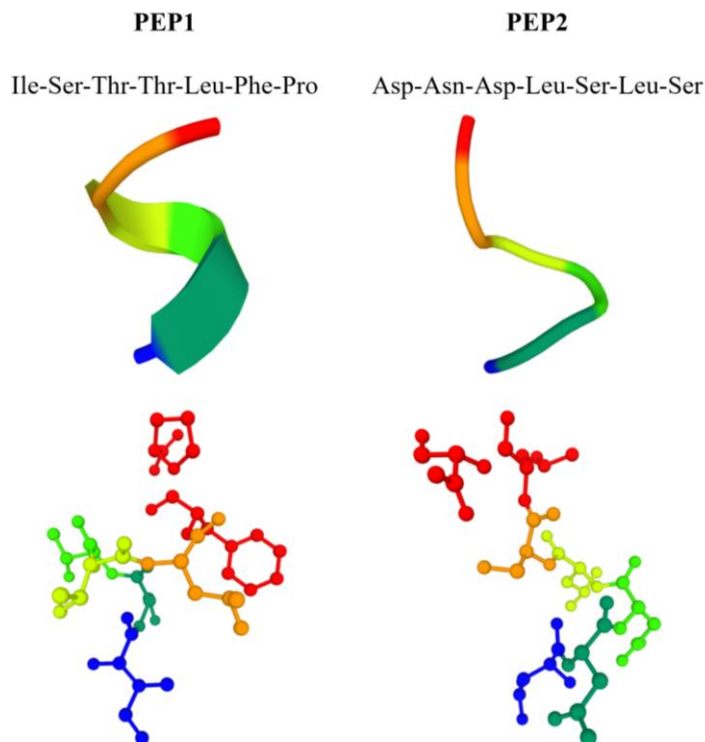


Figure 34. Sequences and 3D models of synthesized peptides¹³⁵

6.3.2. IMMOBILIZATION OF THE PEPTIDES ON THE μ IMZI SURFACE

In case of any label-free biosensor, the key technological step is the implementation of a uniform functionalization layer on the surface, which contains a bioreceptor selective to the biological target. On the other hand, the most important requirement for the optical transducer is to reach the highest sensitivity to the biochemical interactions between receptor and target and to convert this into a shift of the spectral minimum.

In the case of microcavity-based sensors, surface functionalization is not responsible just for the selectivity of the sensor. When highly optimized, it can also enhance the surface sensitivity of the platform leading to lower detection limits. When there is no thin film (or when the functionalization layer is very thin), the sensor is highly sensitive towards bulk RI, what may not correspond to the surface sensitivity – as we discussed in Chapter 5.

While optimizing the functionalization process, we have to consider also the properties of the chosen bioreceptor (the size, RI) as it can change working conditions of the μ IMZI through the

formation of an adlayer. The functionalization process presented in 6.2 section is the perfect example. The deposition there was conducted in the way to obtain as thin layer of the APTES as possible. We wanted to avoid changing the properties of the surface because further immobilization of the MS2 phages strongly affected the spectral response with ~ 30 nm layer.

In an experiment presented in this section, the synthesized peptide aptamers, with ~ 3 nm size and RI approximate to PBS buffer will not affect the surface the way the phages did. Thus, we extended the silanization process with APTES from 30 min to 2 h achieving thicker functionalization layer and higher surface sensitivity.

Fig. 35 presents the transmission spectra obtained for each stage of the optimized functionalization process (detailed in Appendix C), namely:

1. Functionalization of the surface – 2 h silanization with APTES (gas phase, black curve);
2. Activation of the deposited amine groups by glutaraldehyde (GLU, green curve);
3. Immobilization of bioreceptor – peptide aptamers – followed by blocking the surface of the microcavity with glycine solution (GLY, red curve);

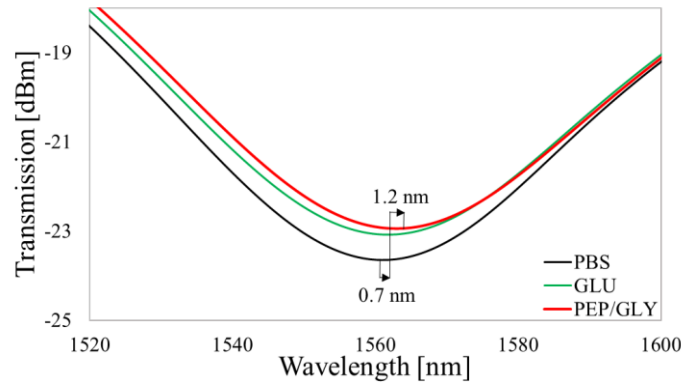


Figure 35. The response of the μ IMZI where the transmission spectra in PBS at each stage of the surface functionalization process after incubation and extensive washing.

Such a modification allows us to follow every single step of the functionalization process. Even the nanometer changes such as deposition of GLU, before unrecognizable, now become visualized in the spectrum.

In addition, the water contact angle measurements allowed monitoring the impact of increasing the time of silanization on the surface wettability (Fig. 36). The cleaning of the glass surface decreased contact angle to the immeasurable value. Next, 30 min of silanization process re-increased it to 57° making surface hydrophobic. Then, 2 h silanization process further increased the hydrophobicity of the surface changing the contact angle to 72° . The value obtained for APTES modification is similar to the previously reported¹¹⁸, but the comparison can be problematic due to the different experimental conditions and to the methodology applied by the authors¹³⁶.

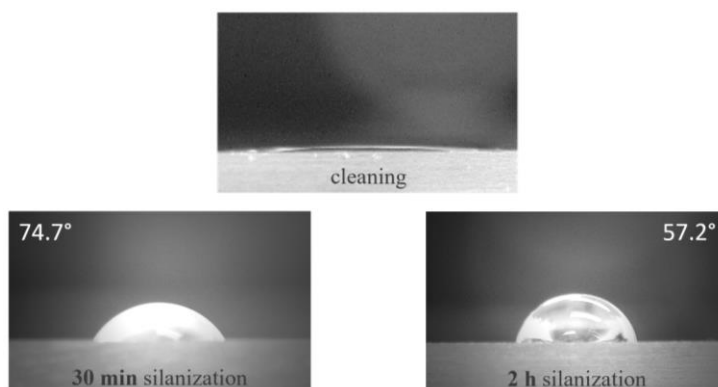


Figure 36. Photos of the water droplet deposited on the glass surface: before cleaning and after 30 min and 2 h silanization processes.

The last modification that we have introduced to the surface functionalization process was the change of the blocking solution. Considering the size of the current bioreceptor, we decided to block the unreacted active groups on the sensor surface by glycine – the smallest, optically inactive amino acid (~ 0.42 nm) instead of previously used BSA. Knowing the dimensions of BSA it could easily cover immobilized peptides, thereby affect further measurements with bacteria. Such modified functionalization allowed us to prepare the surface of μ IMZI for the next step – bacteria detection.

Safety considerations

E. coli O157:H7 is a harmful bacterium that should be handled with care. Heat-killed *E. coli* O157:H7 used during our experiments were handled in a laminar-flow hood. All *E. coli* O157:H7-contaminated labware was autoclaved before being discarded. All details including bacteria culturing and quantification are described in Appendix B.

6.3.3. DETECTION OF PATHOGENIC HEAT-KILLED *E. COLI* O157:H7

Due to safety reasons only heat-treated and therefore inactivated cells of *E. coli* O157:H7 were used during the experiments. This type of inactivation of microorganisms affects bacteria cells differently than the lyophilization process described in Section 6.2.1. Dry-mass preparation is based on cell dehydration, while exposure to heat consists of the simultaneous alteration of one or more cellular structures or functions – so-called cellular targets. Fig. 37 illustrates the most relevant cellular events that occur under such treatment.

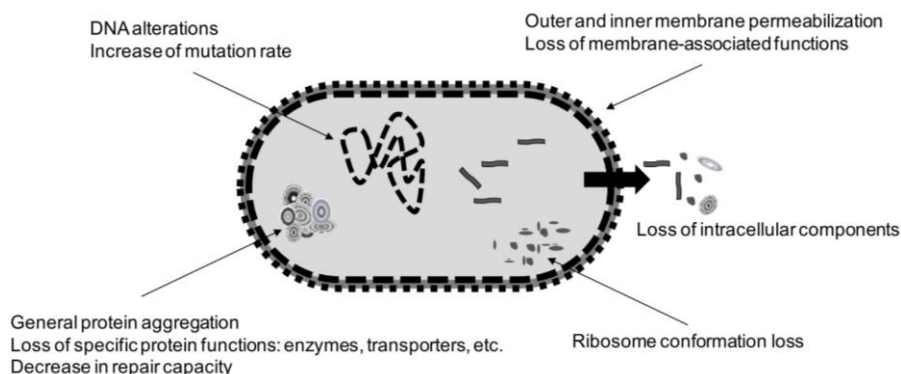


Figure 37. Summary of the most relevant cellular events that occur in a vegetative bacterial cell upon exposure to heat.

Many attempts have failed to identify the particular structures and processes whose alteration under exposure to heat leads to cell death. The cellular structures that have been considered as primarily affected by cell inactivation through heat are the outer and inner membrane, the peptidoglycan cell walls, the nucleoids, the cells RNA, the ribosomes, and several enzymes. Given the close and multiple interrelationships between the various structures and their functions, it can be stated that microbial inactivation by heat is a multi-factor phenomenon¹³⁷.

The structural properties of bacteria cells can be changed during the inactivation methods as was explained in section 6.2. The most critical part that should be stable and preserved to provide stable and reliable results is an outer membrane/cell wall and fimbria/pili. These are potential binding targets for synthesized peptide aptamers. Damages inflicted to the outer membrane of G- bacteria have been evidenced, among other things, through the sensitization of cells to bile salts, lysozyme or hydrophobic antibiotics as reported in¹³⁸. The release of LPS molecules and vesicles to the treatment medium has also been described before¹³⁹. Even though the occurrence of membrane alterations has been well established, a clear relationship with cell inactivation has not been proven. Various recent studies indicate that cell death takes place before the membrane becomes permeable to propidium iodide^{140,141}. It is possible therefore to inactivate bacteria without destroying the cell wall and its outer structures. This keeps bacteria in proper shape enabling mimicking the live microorganism and eventually allows the selected peptides to recognize the bacteria surface.

To analyze and to compare the binding abilities of peptides, they were used either separately (PEP-1 and PEP-2) or as a mixture of both (PEP-MIX), with their final concentration always equal to 1mg/ml. Given that the functionalization process introduced the same changes in the spectrum for all three samples (Fig. 35), from now on the signal after incubation with PEP/GLY (red curve) will be considered as a baseline.

The μ IMZI sensor with peptide aptamers immobilized on the surface was used to detect different concentrations of heat-killed *E. coli* O157:H7 strain in solution. Bacteria dilutions were prepared with concentrations of 10, 10^3 , 10^5 , and 10^7 CFU/mL in PBS. For selectivity measurements, negative samples containing *B. Thailandensis* were prepared with a concentration of 10^8 CFU/mL. During the experiments, the sensor was immersed in solutions of increasing concentrations of specific *E. coli* strain for 30 minutes for each concentration. After the bacteria incubation, the sensor has been extensively washed and measured in PBS to obtain its reference results. The difference between the wavelengths corresponding to the transmission minima after GLY binding and after each exposition to bacteria was defined as the sensor response.

Fig. 38 illustrates the spectra obtained at each stage of the experiment with PEP-1 in PBS after extensive washing of the cavity.

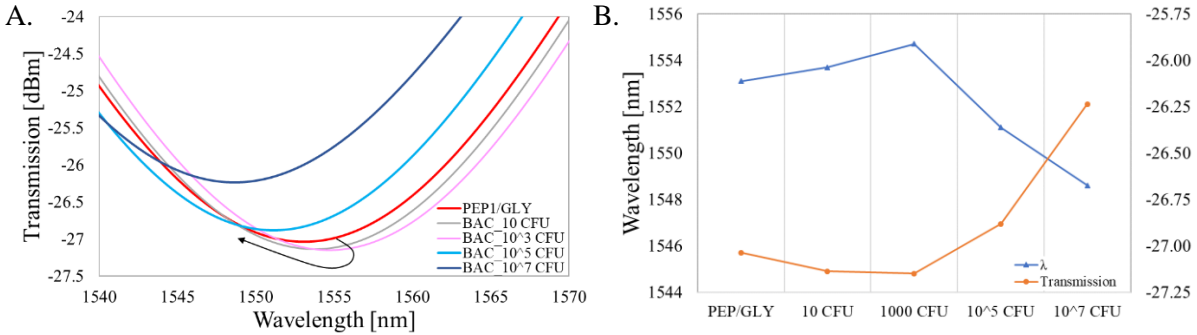


Figure 38. The response of the μ IMZI at each stage of the experiment with PEP-1 and different concentrations of heat-killed *E. coli* O157:H7 bacteria where A) shows the transmission spectra in PBS after incubation and extensive washing and B) shows a correlation between the transmission and the wavelength.

For concentration as low as 10 CFU of *E. coli* bacteria (grey curve) we observe a small, but noticeable 0.6 nm shift towards longer wavelengths. The addition of bacterial solutions with a concentration of up to 10³ CFU/mL (pink curve) keeps shifting the spectrum towards longer wavelengths and increasing its depth. For higher concentrations – 10⁵-10⁷ CFU/ml (blue and navy-blue curves) – the direction of the shift has changed towards shorter wavelengths, and the depth of the minimum started decreasing. The obtained results are in agreement with the previous explanation provided in Section 6.2, where the response followed the same non-monotonic pattern.

The ability to detect such a small amount of bacteria highlights the exceptional sensitivity of the sensor, but also may indicate that the peptide immobilized at the sensors' surface had excellent access to its target. The parts of bacteria which are the most likely to reach the μ IMZI surface first are hair-like structures, namely: the flagella or fimbriae/pili. One of the essential roles of these cellular structures is to initiate the attachment, what leads to a biofilm formation. What also has been proven, the more pathogenic bacteria have more hair-like structures on the surface, what in this case could facilitate bacteria detection. Through heat-inactivation bacteria losses motility, what also could improve the measurements. However, the obtained results and a pattern similar to the experiment with live bacteria (Section 6.2.3) showed that a well-chosen method of heat-inactivation did not affect the shape of bacteria or the cell surface structures.

Fig. 39 presents the spectra obtained using the second peptide (PEP-2).

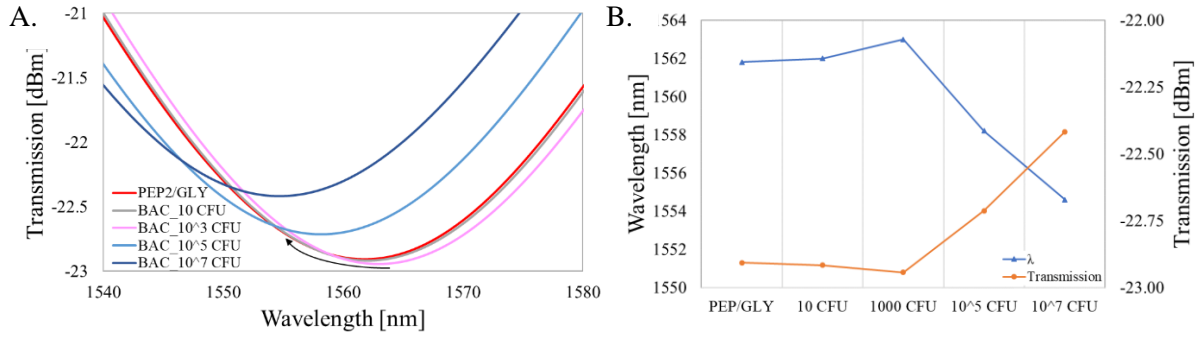


Figure 39. The response of the μ IMZI at each stage of the experiment with PEP-2 and different concentrations of heat-killed *E. coli* O157:H7 bacteria where A) shows the transmission spectra in PBS after incubation and extensive washing and B) shows a correlation between the transmission and the wavelength.

In general, despite the slightly different initial position of the minima, the sample revealed the same trend as far as the shift and the depth of the minimum are concerned. The smallest concentration of bacteria (grey curve) induced a minimal 0.2 nm shift, which is very close to the error value, and for this reason, it will not be treated as a positive response. However, the subsequent additions of the solutions with a higher concentration of *E. coli* O157:H7 intensify the shift and cause further changes in the wavelength of the transmission minimum.

The shift for concentrations higher than 10³ CFU is more significant than this observed for the PEP-1 sample, what also may provide additional information about the binding site of the bioreceptor. The higher the concentration, the more bacteria are inside the cavity. Then the probability that *E. coli* cells are getting closer to the functionalized surface increases, and the targets placed on the bacteria surface are more accessible to peptides.

Fig. 40 illustrates the set of results for a mix of peptides.

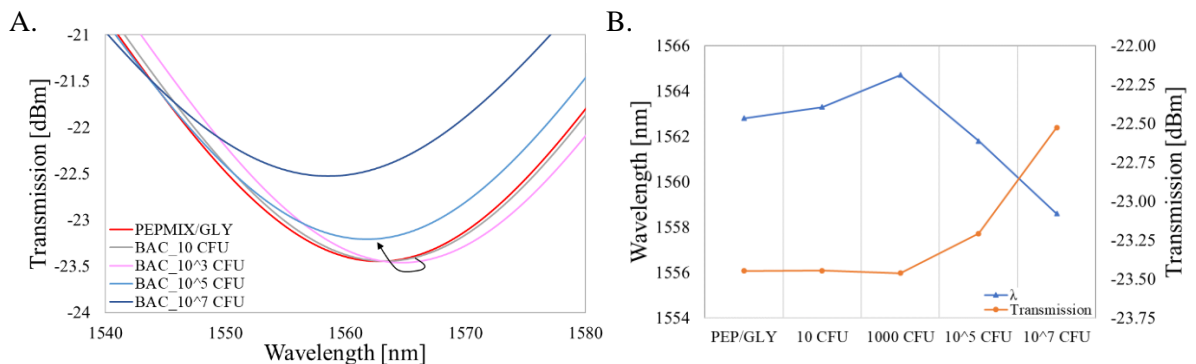


Figure 40. The response of the μ IMZI at each stage of the experiment with PEP-MIX and different concentrations of heat-killed *E. coli* O157:H7 bacteria where A) shows the transmission spectra in PBS after incubation and extensive washing and B) shows a correlation between the transmission and the wavelength.

Considering that previous samples revealed a similar trend in the shift and depth of the minimum, it would not be surprising if the combination of both will give us similar results. As can be seen, the PEP-MIX was able to detect even the smallest concentration of bacteria (grey curve) shifting the spectrum by 0.5 nm towards the longer wavelengths. We can assume that the presence of the PEP-1 contributed the most to the detection of 10 CFU bacteria. Second concentration - 10^3 CFU (pink curve) induced 1.4 nm shift, which is almost 50% more in comparison to the signal measured for separated peptides. It can be justified by the detection of two different targets occurring simultaneously in this case.

Fig. 41 presents a comparison of spectral shifts caused by each concentration of bacteria for all three samples, where negative values correspond to the shift towards longer wavelengths, and positive values – towards shorter wavelengths.

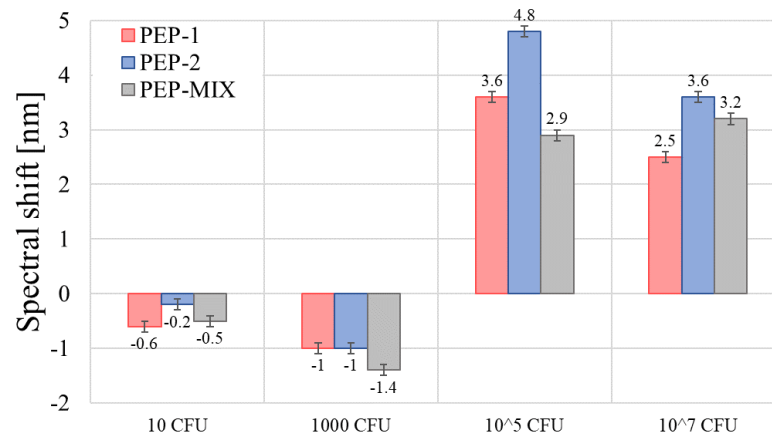


Figure 41. The juxtaposition of spectral shifts after each concentration of heat-killed *E. coli* O157:H7 bacteria for two separate peptides (PEP-1 and PEP-2) as well as for their combinations (PEP-MIX).

Bearing in mind the infectious dose of a detected strain of bacteria, which is ~100 cells, the choice of PEP-1 or PEP-MIX for future applications will be well justified.

Fig. 42 shows the minimum's wavelength after each stage of the biofunctionalization with PEP-MIX to assure that the obtained shifts come from the formation of the biological layer at the sensors' surface, not from the changing of RI of the solution. The spectrum experienced a temporary shift towards the lower wavelengths during each incubation with high-RI liquid, e.g., GLU, or high concentration of bacteria (10^7 CFU/mL). Only after an extensive washing of the microcavity with PBS, the signal begins to change as a function of the real influence of the adlayer.

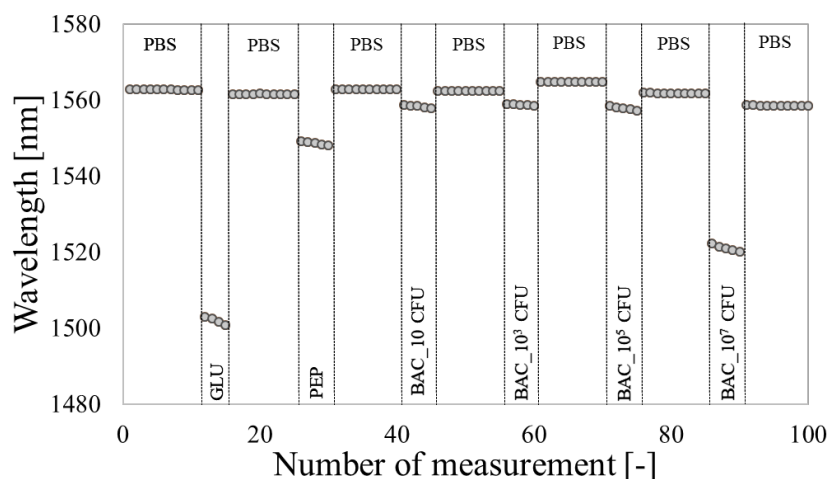


Figure 42. A shift of the minimum's wavelength at each stage of the experiment induced by functionalization and incubation in different concentrations of heat-killed bacteria.

6.2.5. PERFORMANCE EVALUATION OF MS2 PHAGES AND PEPTIDE APTAMERS WHEN APPLIED AS RECOGNITION ELEMENTS

Despite all the differences between the two chosen types of bioreceptors, we could notice similarities of the results obtained in both cases. Along with the increasing concentration of bacteria, the same trend regarding the wavelength shift of the minimum could be observed. Both strains of bacteria, namely *E. coli* C3000 and O157:H7 have similar size and RI. Therefore the biolayers formed during both experiments had similar properties and covered an equal part of the cavity. However, we could also observe some differences, therein two the most apparent: the values of the shift for the small concentrations, and different pattern regarding the depth of the minimum. Based on the knowledge we acquired after evaluating the process of thin-layer deposition inside the microcavity it can be stated that the different working conditions of the μ IMZI after bioreceptor immobilization caused both of them. In section 6.2 the spectrum revealed that after incubation with MS2, the created 30 nm adlayer, with RI equal to ~ 1.217 RIU, strongly affected the working conditions of the μ IMZI. The effect is equivalent to the thin-layer deposition, and it is very likely that it affected the sensitivity of the sensor.

From the other hand, the immobilization of ~ 3 nm thick layer of peptides, with RI approximately equal to that of the buffer, was barely noticeable. For this reason, a similar shift was observable only after incubation with a higher concentration of bacteria (10^5 CFU) when

the biolayer got thicker and started affecting the n_{cl} . This comparison shows how important is the choice of the bioreceptor, why it is the key element in label-free biosensing, how it can influence the whole experiment and affect the obtained results.

6.2.6. NEGATIVE CONTROLS

To confirm that even the smallest spectral shift was influenced mostly by the change in the thickness of the specific biolayer on the μ IMZI surface, two negative control experiments were performed. First one was designed to verify selectivity of the bioreceptor using the *B. Thailandensis* strain, which shows no affinity to both combined peptides. The second control experiment was performed with no receptor at all using specific O157:H7 strain solely. The second experiment aimed at showing that without a specific biorecognition element on the surface, it is impossible to detect bacteria just by exposing the biosample to the functionalized surface.

Both experiments (Figs. 43A&B) clearly show that during bacteria incubation the minimum significantly shifts towards shorter wavelengths (green double curves). This is attributed to the high RI of the highly concentrated bacteria solution (10^8 CFU/mL). In Fig. 43B, the blue curve presents the spectrum after single cleaning of the μ IMZI with PBS. It shows how important is extensive washing of the cavity after each incubation to avoid “false-positive” signals. Despite the very high concentration of the bacteria samples (10^8 CFU/mL), after three washes with PBS, no wavelength shift was observed, indicating that there is no interaction and no specific binding on the surface (blue-dashed curve). These results confirm our previous findings on the selectivity and reliability of the developed sensor.

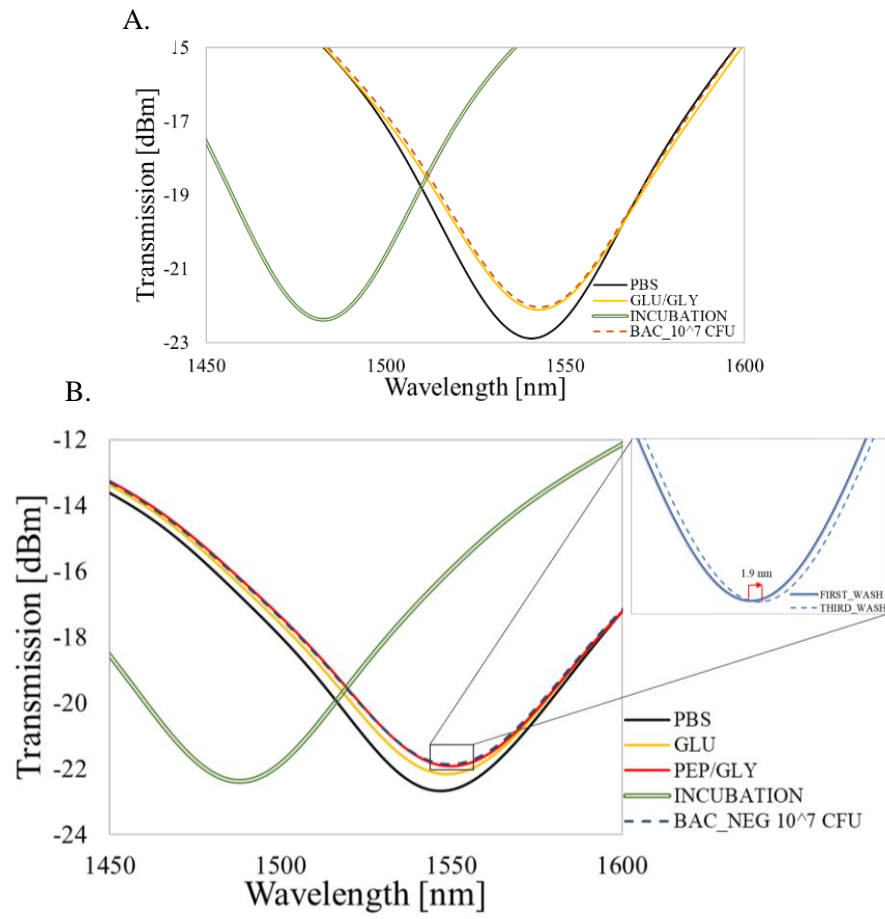


Figure 43. Transmission spectra of the μ MZI at each of the stage of the experiment, showing the response A) for positive *E. coli* O157:H7 without peptides on the sensor's surface and B) for negative *B. Thailandensis* with PEP-MIX.

6.2.7. CONCLUSIONS

Two specific peptide aptamers were selected using the Phage Display method and were successfully used as biorecognition elements immobilized on the μ IMZI surface. Up to our best knowledge, this is the first study to date where the peptide aptamers were employed as bioreceptors on the fiber-optic sensor. Due to the optimized surface functionalization process, the reported device allowed for detecting even nm changes in the biolayer thickness. It also provided stable and specific label-free detection of different concentrations of heat-killed pathogenic *E. coli* O157:H7. The limit of detection of the demonstrated real-time measurements reached 10 CFU which is better than reported for other FOS platforms. Two negative controls confirmed the reliability of the functionalized sensor. Based on the presented results, we prove once again that the spectral response is caused by the phenomena taking place on the surface of the sensor, and not by the RI changes of the analyte. Due to its very high RI sensitivity, easiness of fabrication, very low-temperature sensitivity and ability to work with sub-nanoliter volumes, the described sensor has shown superiority over the other fiber-optic platforms.

CHAPTER 7

CONCLUSIONS

The main objective of this project was to develop rapid and real-time detection of pathogenic *E. coli* bacteria using microcavity in-line Mach-Zehnder interferometer (μ IMZI). Considering the highly multidisciplinary scope of the work we divided the work for two main parts namely: optical and biological.

The first step towards achieving a specific biosensor was the development and testing of a new, miniaturized fiber-optic sensing device. During this Ph. D project we have mastered one step fs-laser fabrication of the microcavities. Experimental results proved excellent repeatability of the micromachining process. Furthermore, all of the tested optical fiber structures exhibit high and linear RI sensitivities in a wide range of the investigated RIs, where the sensitivity barely depends on the cavity diameter. Also, the measurements revealed that the μ IMZI is temperature insensitive, what makes it an even better choice for bio- and chemosensing since temperature is one of the most disrupting factors in the RI measurements.

Next step included cleaning and hydrophilization of the optical fiber's surface to make further measurements easier to perform and more repeatable. To complete this step we performed a set of experiments using reactive ion etching. In comparison to, for example, widely used wet etching, a plasma treatment provided high accuracy and control over the process. We obtained highly defined and more clear minima, what increased the measurement accuracy. Also, the RIE post-processing cleaned microcavity, smoothed the side walls, evened the bottom and increased the wettability of the cavity's surface. This in turn significantly facilitated the introduction of liquids into the microcavity.

Once a surface was prepared, we verified the ability to label-free detection using a μ IMZI. We have deposited the Al_2O_3 films on the set of μ IMZIs using the atomic layer deposition method. During this experiment we have discovered that depending on the interferometer working conditions determined by the thin layer on the surface, the device can be used in two

ways. Firstly, for investigation of phenomena taking place at the surface, such as in case of specific label-free biosensing applications. Secondly, for small-volume RI analysis as required in analytical chemistry. Our studies also have shown, that the obtained signal can be tuned to a specific range, which in turn allows adjusting the location of the minimum to almost arbitrary wavelength range specific to a given interrogating system.

After completing the optical part of the project, we could conduct biological experiments. The fourth and last step of this Ph. D. project covers the surface functionalization process and finally conducting the bacteria detection experiments.

An appropriate functionalization using phages and peptide aptamers allowed detecting the pathogenic *E. coli* bacteria. Well-adjusted bioreceptor eliminated the risk of false positive output in complex environments and gives accurate and reliable results.

First, we exposed the functionalized biosensor to different concentrations of live bacteria using MS2 bacteriophages as recognition elements. The limit of detection for these real-time measurements reached 100 CFU/mL. During the next experiment, two specific peptide aptamers were selected using the Phage Display method and were successfully used as biorecognition elements immobilized on the μ IMZI surface. Up to our best knowledge, this was the first study to date, where the peptide aptamers were employed as bioreceptors on the fiber-optic sensor. We performed stable and specific label-free detection of different concentrations of heat-killed pathogenic *E. coli* O157:H7. The limit of detection of the demonstrated real-time measurements reached 10 CFU.

The surface functionalization process was well adjusted to both the μ IMZI platform as well as to the chosen bioreceptors. Thanks to that the reported device allowed for detecting even nm changes in the biolayer thickness. After each experiment, two negative controls confirmed the reliability of the functionalized sensor. Based on these results, we proved that the spectral response is caused by the phenomena taking place on the surface of the sensor, and not by the RI changes of the analyte. Due to its very high RI sensitivity, easiness of fabrication, very low-temperature sensitivity and ability to investigate sub-nanoliter volumes, the described sensor has shown superiority over the other fiber-optic platforms.

FUTURE WORK

We achieved for the first time, a label-free detection of bacteria using the microcavity in-line Mach-Zehnder interferometer. The sensor was highly specific, reached the lowest detection limit and provided a very fast response. Despite this success, some improvements are still needed, especially if the use of such biosensors needs to be expanded outside the academic laboratory. It becomes thus important to integrate this biosensor into a lab on a chip in order to have a robust, low cost, easy to use and portable device.

Many studies have demonstrated the ability to detect single molecules thanks to their high sensitivity. However, this kind of experiments is still challenging in complex environments like blood or serum. The high RI sensitivity of the μ IMZI can be useful in the future to analyse the interactions between the molecules or the kinetics of binding between them.

Considering bulk and surface sensitivity of the presented device, the combination of the sensor and nanocoating can also be explored. Deposition of appropriate material inside the microcavity will allow for adjusting and tuning its sensitivity depending on the desired biological molecule and to detect the target in sub-nanoliter volumes. Considering novel and miniature design, ability to measure picoliter volumes, and temperature insensitivity, the μ IMZI has also a great potential in biosensing as a point-of-care device.

Many bacteria strains are mutating and becoming resistant to antibiotics and other treatments. Thus, the studies and research in the field of diagnostics are developing fast. This is why the biosensing field needs to continuously improve to always provide the most sensitive, specific, robust, high resolution and fast response biosensors.

LITERATURE

1. Wong, K., Bouchard, D. & Molina, M. Relative transport of human adenovirus and MS2 in porous media. *Colloids Surfaces B Biointerfaces* **122**, 778–784 (2014).
2. Janik, M. *et al.* Sensitivity Pattern of Femtosecond Laser Mach-Zehnder Interferometers , as Applied to Small-Scale Refractive Index Sensing. *IEEE Sens. J.* **17**, 3316–3322 (2017).
3. Tripathi, S. M. *et al.* Long period grating based biosensor for the detection of Escherichia coli bacteria. *Biosens. Bioelectron.* **35**, 308–312 (2012).
4. Koba, M. *et al.* Bacteriophage adhesin-coated long-period grating-based sensor: Bacteria detection specificity. *J. Light. Technol.* **34**, 4531–4536 (2016).
5. Brzozowska, E. *et al.* Recognition of bacterial lipopolysaccharide using bacteriophage-adhesin-coated long-period gratings. *Biosens. Bioelectron.* **67**, 93–99 (2015).
6. Smietana, M. *et al.* Detection of bacteria using bacteriophages as recognition elements immobilized on long-period fiber gratings. *Opt. Express* **19**, 7971–7978 (2011).
7. Kaper, J. B., Nataro, J. P. & Mobley, H. L. T. Pathogenic Escherichia coli. *Nat. Rev. Microbiol.* **2**, 123–140 (2004).
8. Lim, J. Y., Yoon, J. W. & Hovde, C. J. A brief overview of Escherichia coli O157:H7 and its plasmid O157. *J. Microbiol. Biotechnol.* **20**, 1–10 (2010).
9. Varma, J. K. An Outbreak of Escherichia coli O157 Infection Following Exposure to a Contaminated Building. *JAMA* **290**, 2709 (2003).
10. Baker, C. A., Rubinelli, P. M., Park, S. H., Carbonero, F. & Ricke, S. C. Shiga toxin-producing Escherichia coli in food: Incidence, ecology, and detection strategies. *Food Control* **59**, 407–419 (2016).
11. Frenzen, P. D., Drake, A. & Angulo, F. J. Economic Cost of Illness Due to Escherichia coli O157 Infections in the United States. *J. Food Prot.* **68**, 2623–2630 (2005).
12. Yang, S.-C., Lin, C.-H., Aljuffali, I. A. & Fang, J.-Y. Current pathogenic Escherichia coli foodborne outbreak cases and therapy development. *Arch. Microbiol.* **199**, 811–825 (2017).
13. Saxena, T., Kaushik, P. & Krishna Mohan, M. Prevalence of E. coli O157: H7 in water sources: An overview on associated diseases, outbreaks and detection methods. *Diagn. Microbiol. Infect. Dis.* **82**, 249–264 (2015).
14. Doyle, M. E., Archer, J., Kaspar, C. W. & Weiss, R. Human Illness Caused by E. coli O157:H7 from Food and Non-food Sources. *FRI Briefings* 1–37 (2006).
15. Angus, D. C. & van der Poll, T. Severe Sepsis and Septic Shock. *N. Engl. J. Med.* **369**, 840–851 (2013).
16. Wang, X. & Wolfbeis, O. S. Fiber-Optic Chemical Sensors and Biosensors (2013 – 2015). *Anal. Chem.* **88**, 203–227 (2016).
17. Chiavaioli, F., Baldini, F., Tombelli, S., Trono, C. & Giannetti, A. Biosensing with

- optical fiber gratings. *Nanophotonics* **6**, 663–679 (2017).
18. Moran, K. L. M., Lemass, D. & Kennedy, R. O. Surface Plasmon Resonance - Based Immunoassays: Approaches, Performance, and Applications. in *Handbook of Immunoassay Technologies* 129–156 (Elsevier Inc., 2018). doi:10.1016/B978-0-12-811762-0.00006-2
 19. Chen, Y. *et al.* Recent advances in rapid pathogen detection method based on biosensors. *Eur. J. Clin. Microbiol. Infect. Dis.* **37**, 1021–1037 (2018).
 20. Liang, G. *et al.* Fiber Optic Surface Plasmon Resonance–Based Biosensor Technique: Fabrication, Advancement, and Application. *Crit. Rev. Anal. Chem.* **46**, 213–223 (2016).
 21. Arghir, I., Spasic, D., Verlinden, B. E., Delport, F. & Lammertyn, J. Improved surface plasmon resonance biosensing using silanized optical fibers. *Sensors Actuators B Chem.* **216**, 518–526 (2015).
 22. Huang, S. *et al.* Optimization of phage-based magnetoelastic biosensor performance. *Sens. Transducers J.* **3**, 87–96 (2008).
 23. Yoo, S. M. & Lee, S. Y. Optical Biosensors for the Detection of Pathogenic Microorganisms. *Trends Biotechnol.* **34**, 7–25 (2016).
 24. Vengsarkar, A. M. *et al.* Long-period fiber gratings as band-rejection filters. *J. Light. Technol.* **14**, 58–64 (1996).
 25. Śmietana, M., Koba, M., Mikulic, P. & Bock, W. J. Combined plasma-based fiber etching and diamond-like carbon nanooverlay deposition for enhancing sensitivity of long-period gratings. *J. Light. Technol.* **34**, 4615–4619 (2016).
 26. Bandara, A. B. *et al.* Detection of methicillin-resistant staphylococci by biosensor assay consisting of nanoscale films on optical fiber long-period gratings. *Biosens. Bioelectron.* **70**, 433–440 (2015).
 27. Jang, H. S. *et al.* Sensitive DNA biosensor based on a long-period grating formed on the side-polished fiber surface. *Opt. Express* **17**, 3855–3860 (2009).
 28. Pilla, P. *et al.* A protein-based biointerfacing route toward label-free immunoassays with long period gratings in transition mode. *Biosens. Bioelectron.* **31**, 486–491 (2012).
 29. Baliyan, A., Sital, S., Tiwari, U., Gupta, R. & Sharma, E. K. Long period fiber grating based sensor for the detection of triacylglycerides. *Biosens. Bioelectron.* **79**, 693–700 (2016).
 30. Gamaly, E. G., Rode, A. V., Luther-Davies, B. & Tikhonchuk, V. T. Ablation of solids by femtosecond lasers: Ablation mechanism and ablation thresholds for metals and dielectrics. *Phys. Plasmas* **9**, 949 (2002).
 31. Du, D., Liu, X., Korn, G., Squier, J. & Mourou, G. Laser-induced breakdown from 7 ns to 150 fs by impact ionization in SiO₂ with pulse widths. *Appl. Phys. Lett.* **64**, 3071–3073 (1994).
 32. Druon, F., Balembois, F. & Georges, P. New laser crystals for the generation of ultrashort pulses. *Recent Adv. Cryst. Opt.* **8**, 153–164 (2007).

33. Stuart, B. C. *et al.* Optical ablation by high-power short-pulse lasers. *J. Opt. Soc. Am. B* **13**, 459–468 (1996).
34. Schaffer, C. B., Brodeur, A. & Mazur, E. Laser-induced breakdown and damage in bulk transparent materials induced by tightly focused femtosecond laser pulses. *Meas. Sci. Technol.* **12**, 1784–1794 (2001).
35. Keldysh, L. V. Ionization in the field of a strong electromagnetic wave. *Sov. Phys. JEPT* **20**, 1307–1314 (1965).
36. Zhao, Y., Zhao, H., Lv, R. & Zhao, J. Review of optical fiber Mach–Zehnder interferometers with micro-cavity fabricated by femtosecond laser and sensing applications. *Opt. Lasers Eng.* **117**, 7–20 (2019).
37. Donlagic, D. All-fiber micromachined microcell. *Opt. Lett.* **36**, 3148–3159 (2011).
38. Pevec, S. & Donlagic, D. High resolution, all-fiber, micro-machined sensor for simultaneous measurement of refractive index and temperature. *Opt. Express* **22**, 16241 (2014).
39. Wei, T., Han, Y., Li, Y., Tsai, H. & Xiao, H. Temperature-insensitive miniaturized fiber inline Fabry-Perot interferometer for highly sensitive refractive index measurement. *Opt. Express* **16**, 5764 (2008).
40. Ran, Z. L., Rao, Y. J., Liu, W. J., Liao, X. & Chiang, K. S. Laser-micromachined Fabry-Perot optical fiber tip sensor for high-resolution temperature-independent measurement of refractive index. *Opt. Express* **16**, 2252 (2008).
41. Chen, L. X., Huang, X. G., Li, J. Y. & Zhong, Z. B. Simultaneous measurement of refractive index and temperature by integrating an external Fabry-Perot cavity with a fiber Bragg grating. *Rev. Sci. Instrum.* **83**, 053113 (2012).
42. Yuan, L. *et al.* Fiber inline Michelson interferometer fabricated by a femtosecond laser. *Opt. Lett.* **37**, 4489 (2012).
43. Hu, T. Y., Wang, Y., Liao, C. R. & Wang, D. N. Miniaturized fiber in-line Mach–Zehnder interferometer based on inner air cavity for high-temperature sensing. *Opt. Lett.* **37**, 5082 (2012).
44. Liao, C. R., Hu, T. Y. & Wang, D. N. Optical fiber Fabry-Perot interferometer cavity fabricated by femtosecond laser micromachining and fusion splicing for refractive index sensing. *Opt. Express* **20**, 1027–1029 (2012).
45. Wang, Y., Yang, M., Wang, D. N., Liu, S. & Lu, P. Fabricated By Femtosecond Laser Micromachining for Refractive Index Measurement With High Sensitivity. *J. Opt. Soc. Am. B* **27**, 370–374 (2010).
46. Hu, T. Y. & Wang, D. N. Optical fiber in-line Mach–Zehnder interferometer based on dual internal mirrors formed by a hollow sphere pair. *Opt. Lett.* **38**, 3036–3039 (2013).
47. Jiang, L., Zhao, L., Wang, S., Yang, J. & Xiao, H. Femtosecond laser fabricated all-optical fiber sensors with ultrahigh refractive index sensitivity: modeling and experiment. *Opt. Express* **19**, 17591–17598 (2011).
48. Zhao, L. *et al.* A high-quality Mach-Zehnder interferometer fiber sensor by femtosecond

- laser one-step processing. *Sensors* **11**, 54–61 (2011).
49. Sun, X. *et al.* A robust high refractive index sensitivity fiber Mach-Zehnder interferometer fabricated by femtosecond laser machining and chemical etching. *Sensors Actuators, A Phys.* **230**, 111–116 (2015).
 50. Sun, X. Y. *et al.* Highly sensitive refractive index fiber inline Mach-Zehnder interferometer fabricated by femtosecond laser micromachining and chemical etching. *Opt. Laser Technol.* **77**, 11–15 (2016).
 51. Myśliwiec, M. *et al.* Effect of wet etching of arc-induced long-period gratings on their refractive index sensitivity. *Acta Phys. Pol. A* **124**, 521–524 (2013).
 52. Śmietana, M., Koba, M., Mikulic, P. & Bock, W. J. Measurements of reactive ion etching process effect using long-period fiber gratings. *Opt. Express* **22**, 5986–5994 (2014).
 53. Tzeng, Y. & Lin, T. H. Dry Etching of Silicon Materials in SF₆ Based Plasmas. *J Electrochem Soc* **134**, 2304–2309 (1987).
 54. Mogab, C. J., Adams, A. C. & Flamm, D. L. Plasma etching of Si and SiO₂- The effect of oxygen additions to CF₄ plasmas. *J. Appl. Phys.* **49**, 3796–3803 (1978).
 55. Tsai, W. T. The decomposition products of sulfur hexafluoride (SF₆): Reviews of environmental and health risk analysis. *J. Fluor. Chem.* **128**, 1345–1352 (2007).
 56. Śmietana, M., Myśliwiec, M., Mikulic, P., Witkowski, B. S. & Bock, W. J. Capability for fine tuning of the refractive index sensing properties of long-period gratings by atomic layer deposited Al₂O₃ overlays. *Sensors (Switzerland)* **13**, 16372–16383 (2013).
 57. Smietana, M., Koba, M., Mikulic, P. & Bock, W. J. Tuning properties of long-period gratings by plasma post-processing of their diamond-like carbon nano-overlays. *Meas. Sci. Technol.* **25**, (2014).
 58. Homola, T., Matoušek, J., Kormunda, M., Wu, L. Y. L. & Černák, M. Plasma treatment of glass surfaces using diffuse coplanar surface barrier discharge in ambient air. *Plasma Chem. Plasma Process.* **33**, 881–894 (2013).
 59. Langmuir, I. The adsorption of gases on plane surfaces of glass, mica and platinum. *Verh. deut. physic. Ges* **16**, 1361–1402 (1918).
 60. Korzec, D., Kessler, T. & Engemann, J. Reactive ion beam etching of Si/SiO₂ systems using SF₆/O₂ chemistry. *Appl. Surf. Sci.* **46**, 299–305 (1990).
 61. Glass, N. R., Tjeung, R., Chan, P., Yeo, L. Y. & Friend, J. R. Organosilane deposition for microfluidic applications. *Biomicrofluidics* **5**, 1–7 (2011).
 62. Lim, K. B. & Lee, D. C. Surface modification of glass and glass fibres by plasma surface treatment. *Surf. Interface Anal.* **36**, 254–258 (2004).
 63. Hartney, M. A. Oxygen plasma etching for resist stripping and multilayer lithography. *J. Vac. Sci. Technol. B Microelectron. Nanom. Struct.* **7**, 1 (1989).
 64. Xiong, L., Chen, P. & Zhou, Q. Adhesion promotion between PDMS and glass by oxygen plasma pre-treatment. *J. Adhes. Sci. Technol.* **28**, 1046–1054 (2014).

65. d'Agostino, R. & Flamm, D. L. Plasma etching of Si and SiO₂ in SF₆–O₂ mixtures. *J. Appl. Phys.* **52**, 162–167 (1981).
66. Puech, M. & Maquin, P. Low temperature etching of Si and PR in high density plasmas. *Appl. Surf. Sci.* **100–101**, 579–582 (1996).
67. Knizikevičius, R. Simulations of Si and SiO₂ Etching in SF₆+O₂ Plasma. *Acta Phys. Pol. A* **117**, 478–483 (2010).
68. Shih, M., Lee, W. J., Tsai, C. H., Tsai, P. J. & Chen, C. Y. Decomposition of SF₆ in an RF Plasma Environment. *J. Air Waste Manag. Assoc.* **52**, 1274–1280 (2011).
69. Vivensang, C. *et al.* Surface smoothing of diamond membranes by reactive ion etching process. *Diam. Relat. Mater.* **5**, 840–844 (1996).
70. Chason, E. & Mayer, T. M. Low energy ion bombardment induced roughening and smoothing of SiO₂ surfaces. *Appl. Phys. Lett.* **62**, 363–365 (1993).
71. Lee, K. K., Lim, D. R., Kimerling, L. C., Shin, J. & Cerrina, F. Fabrication of ultralow-loss Si/SiO₂ waveguides by roughness reduction. *Opt. Lett.* **26**, 1888–1890 (2001).
72. van der Heide, P. A. M., Baan Hofman, M. J. & Ronde, H. J. Etching of thin SiO₂ layers using wet HF gas. *J. Vac. Sci. Technol. A Vacuum, Surfaces, Film.* **7**, 1719–1723 (1989).
73. Tan, S. H., Nguyen, N. T., Chua, Y. C. & Kang, T. G. Oxygen plasma treatment for reducing hydrophobicity of a sealed polydimethylsiloxane microchannel. *Biomicrofluidics* **4**, 1–8 (2010).
74. Homola, T. *et al.* Activation of poly(ethylene terephthalate) surfaces by atmospheric pressure plasma. *Polym. Degrad. Stab.* **97**, 2249–2254 (2012).
75. Liao, C. R., Wang, D. N. & Wang, Y. Microfiber in-line Mach-Zehnder interferometer for strain sensing. *Opt. Lett.* **38**, 757–9 (2013).
76. Li, Z. *et al.* Highly-sensitive gas pressure sensor using twin-core fiber based in-line Mach-Zehnder interferometer. *Opt. Express* **23**, 6673–6678 (2015).
77. Im, H., Wittenberg, N. J., Lindquist, N. C. & Oh, S. H. Atomic layer deposition: A versatile technique for plasmonics and nanobiotechnology. *J. Mater. Res.* **27**, 663–671 (2012).
78. Oh, J., Myoung, J., Bae, J. S. & Lim, S. Etch Behavior of ALD Al₂O₃ on HfSiO and HfSiON Stacks in Acidic and Basic Etchants. *J. Electrochem. Soc.* **158**, D217–D222 (2011).
79. Śmietana, M., Janik, M., Koba, M. & Bock, W. J. Transition between bulk and surface refractive index sensitivity of micro-cavity in-line Mach-Zehnder interferometer induced by thin film deposition. *Opt. Express* **25**, 26118–26123 (2017).
80. Long, F., Zhu, A. & Shi, H. Recent Advances in Optical Biosensors for Environmental Monitoring and Early Warning. *Sensors* **13**, 13928–13948 (2013).
81. Janeway, C. A., Travers, P., Walport, M. & Shlomchik, M. *Immunobiology. The Immune System in Health and Disease*. (Garland Publishing, 2001).
82. Byrne, B., Stack, E., Gilmartin, N. & O'Kennedy, R. Antibody-based sensors:

Principles, problems and potential for detection of pathogens and associated toxins. *Sensors (Switzerland)* **9**, 4407–4445 (2009).

83. Welch, N. G., Scoble, J. A., Muir, B. W. & Pigram, P. J. Orientation and characterization of immobilized antibodies for improved immunoassays (Review). *Biointerphases* **12**, 02D301 (2017).
84. Rostova, E., Adiba, C. Ben, Dietler, G. & Sekatskii, S. K. Kinetics of antibody binding to membranes of living bacteria measured by a photonic crystal-based biosensor. *Biosensors* **6**, 1–9 (2016).
85. Suo, Z. *et al.* Antibody Selection for Immobilizing Living Bacteria. *Anal. Chem.* **81**, 7571–7578 (2009).
86. Wang, W., Singh, S., Zeng, D. L., King, K. & Nema, S. Antibody structure, instability, and formulation. *J. Pharm. Sci.* **96**, 1–26 (2007).
87. Kimura, M., Jia, Z. J., Nakayama, N. & Asakawa, S. Ecology of viruses in soils: Past, present and future perspectives. *Soil Sci. Plant Nutr.* **54**, 1–32 (2008).
88. Suttle, C. A. Marine viruses - Major players in the global ecosystem. *Nat. Rev. Microbiol.* **5**, 801–812 (2007).
89. Mills, S. *et al.* Movers and shakers: Influence of bacteriophages in shaping the mammalian gut microbiota. *Gut Microbes* **4**, 4–16 (2013).
90. Chaturongakul, S. & Ounjai, P. Phage-host interplay: Examples from tailed phages and Gram-negative bacterial pathogens. *Front. Microbiol.* **5**, 1–8 (2014).
91. Singh, A., Poshtiban, S. & Evoy, S. Recent advances in bacteriophage based biosensors for food-borne pathogen detection. *Sensors (Switzerland)* **13**, 1763–1786 (2013).
92. Rossmann, M. G. & Rao, V. B. *Viral Molecular Machines*. (Springer US, 2012). doi:10.1007/978-1-4614-0980-9
93. Tok, J. B. H., Cho, J. & Rando, R. R. RNA aptamers that specifically bind to a 16S ribosomal RNA decoding region construct. *Nucleic Acids Res.* **28**, 2902–2910 (2000).
94. Alizadeh, N., Memar, M. Y., Moaddab, S. R. & Kafil, H. S. Aptamer-assisted novel technologies for detecting bacterial pathogens. *Biomed. Pharmacother.* **93**, 737–745 (2017).
95. Teng, J. *et al.* Aptamer-Based Technologies in Foodborne Pathogen Detection. *Front. Microbiol.* **7**, 1–11 (2016).
96. Lee, J. H., Yigit, M. V., Mazumdar, D. & Lu, Y. Molecular diagnostic and drug delivery agents based on aptamer-nanomaterial conjugates. *Adv. Drug Deliv. Rev.* **62**, 592–605 (2010).
97. Tombelli, S., Minunni, M. & Mascini, M. Analytical applications of aptamers. *Biosens. Bioelectron.* **20**, 2424–2434 (2005).
98. Knudsen, S. M., Robertson, M. P. & Ellington, A. D. In Vitro Selection Using Modified or Unnatural Nucleotides. in *Current Protocols in Nucleic Acid Chemistry* **9**, 9.6.1–9.6.21 (John Wiley & Sons, Inc., 2001).

99. Song, S., Wang, L., Li, J., Fan, C. & Zhao, J. Aptamer-based biosensors. *TrAC - Trends Anal. Chem.* **27**, 108–117 (2008).
100. Templier, V., Roux, A., Roupioz, Y. & Livache, T. Ligands for label-free detection of whole bacteria on biosensors: A review. *TrAC - Trends Anal. Chem.* **79**, 71–79 (2016).
101. Ohk, S. & Bhunia, A. K. Multiplex fiber optic biosensor for detection of *Listeria monocytogenes*, *Escherichia coli* O157 : H7 and *Salmonella enterica* from ready-to-eat meat samples. *Food Microbiol.* **33**, 166–171 (2013).
102. Li, J., Tan, S., Chen, X., Zhang, C.-Y. & Zhang, Y. Peptide Aptamers with Biological and Therapeutic Applications. *Curr. Med. Chem.* **18**, 4215–4222 (2011).
103. Liu, Q., Wang, J. & Boyd, B. J. Peptide-based biosensors. *Talanta* **136**, 114–127 (2015).
104. Mascini, M., Palchetti, I. & Tombelli, S. Nucleic acid and peptide aptamers: Fundamentals and bioanalytical aspects. *Angew. Chemie - Int. Ed.* **51**, 1316–1332 (2012).
105. Kuzmicheva, G. A. & Belyavskaya, V. A. Peptide phage display in biotechnology and biomedicine. *Biochem. (Moscow), Suppl. Ser. B Biomed. Chem.* **11**, 1–15 (2017).
106. Olsen, E. V. *et al.* Affinity-selected filamentous bacteriophage as a probe for acoustic wave biodetectors of *Salmonella typhimurium*. *Biosens. Bioelectron.* **21**, 1434–1442 (2006).
107. Telford, J. L., Barocchi, M. A., Margarit, I., Rappuoli, R. & Grandi, G. Pili in Gram-positive pathogens. *Nat. Rev. Microbiol.* **4**, 509–519 (2006).
108. Kogelberg, H. New structural insights into carbohydrate–protein interactions from NMR spectroscopy. *Curr. Opin. Struct. Biol.* **13**, 646–653 (2003).
109. Lindhorst, T. K. Small Molecule Ligands for Bacterial Lectins: Letters of an Antiadhesive Glycopolymer Code. in *Glycopolymer Code: Synthesis of Glycopolymers and their Applications* (eds. Becer, C. R. & Hartmann, L.) 1–16 (Royal Society of Chemistry, 2015). doi:10.1039/9781782622666
110. Yazgan, I., Noah, N. M., Toure, O., Zhang, S. & Sadik, O. A. Biosensor for selective detection of *E. coli* in spinach using the strong affinity of derivatized mannose with fimbrial lectin. *Biosens. Bioelectron.* **61**, 266–273 (2014).
111. Tait, E., Perry, J. D., Stanforth, S. P. & Dean, J. R. Bacteria detection based on the evolution of enzyme-generated volatile organic compounds: Determination of *Listeria monocytogenes* in milk samples. *Anal. Chim. Acta* **848**, 80–87 (2014).
112. Queirós, R. B., De-Los-Santos-Álvarez, N., Noronha, J. P. & Sales, M. G. F. A label-free DNA aptamer-based impedance biosensor for the detection of *E. coli* outer membrane proteins. *Sensors Actuators, B Chem.* **181**, 766–772 (2013).
113. Kuzmanovic, D. A., Elashvili, I., Wick, C., O’Connell, C. & Krueger, S. The MS2 coat protein shell is likely assembled under tension: A novel role for the MS2 bacteriophage A protein as revealed by small-angle neutron scattering. *J. Mol. Biol.* **355**, 1095–1111 (2006).
114. Dent, K. C. *et al.* The asymmetric structure of an icosahedral virus bound to its receptor

- suggests a mechanism for genome release. *Structure* **21**, 1225–1234 (2013).
115. Brewster, L., Langley, M. & Twa, D. Co-infection of C3000 Escherichia coli with Bacteriophages MS2 and , T7 or Φ X-174 Results in Differential Cell Lysis Patterns. *J. Exp. Microbiol. Immunol.* **16**, 1–5 (2012).
 116. Kuzmanovic, D. A., Elashvili, I., Wick, C., O’Connell, C. & Krueger, S. Bacteriophage MS2: Molecular weight and spatial distribution of the protein and RNA components by small-angle neutron scattering and virus counting. *Structure* **11**, 1339–1348 (2003).
 117. Toropova, K., Basnak, G., Twarock, R., Stockley, P. G. & Ranson, N. A. The Three-dimensional Structure of Genomic RNA in Bacteriophage MS2: Implications for Assembly. *J. Mol. Biol.* **375**, 824–836 (2008).
 118. Gunda, N. S. K., Singh, M., Norman, L., Kaur, K. & Mitra, S. K. Optimization and characterization of biomolecule immobilization on silicon substrates using (3-aminopropyl)triethoxysilane (APTES) and glutaraldehyde linker. *Appl. Surf. Sci.* **305**, 522–530 (2014).
 119. Balch, W. M. *et al.* Light scattering by viral suspensions. *Limnol. Ocean.* **45**, 492–498 (2000).
 120. Rodrigues, D. F. & Elimelech, M. Role of type 1 fimbriae and mannose in the development of Escherichia coli K12 biofilm: From initial cell adhesion to biofilm formation. *Biofouling* **25**, 401–411 (2009).
 121. Liu, P. Y. *et al.* An optofluidic imaging system to measure the biophysical signature of single waterborne bacteria. *Lab Chip* **14**, 4237–4243 (2014).
 122. Srinivasan, R., Umesh, S., Murali, S., Asokan, S. & Siva Gorthi, S. Bare fiber Bragg grating immunosensor for real-time detection of Escherichia coli bacteria. *J. Biophotonics* **10**, 224–230 (2017).
 123. Li, Y. *et al.* Immobilized optical fiber microprobe for selective and sensitive Escherichia coli detection. *J. Biophotonics* **28**, e201700162 (2017).
 124. Wandemur, G. *et al.* Plastic optical fiber-based biosensor platform for rapid cell detection. *Biosens. Bioelectron.* **54**, 661–666 (2014).
 125. Bharadwaj, R. *et al.* Evanescent wave absorbance based fiber optic biosensor for label-free detection of E. coli at 280nm wavelength. *Biosens. Bioelectron.* **26**, 3367–3370 (2011).
 126. Smith, G. Filamentous fusion phage: novel expression vectors that display cloned antigens on the virion surface. *Science* (80-.). **228**, 1315–1317 (1985).
 127. Wu, C. H., Liu, I. J., Lu, R. M. & Wu, H. C. Advancement and applications of peptide phage display technology in biomedical science. *J. Biomed. Sci.* **23**, 1–14 (2016).
 128. Wang, Y. *et al.* Phage-displayed peptide that mimics aflatoxins and its application in immunoassay. *J. Agric. Food Chem.* **61**, 2426–2433 (2013).
 129. Soykut, E. A., Dudak, F. C. & Boyaci, I. H. Selection of staphylococcal enterotoxin B (SEB)-binding peptide using phage display technology. *Biochem. Biophys. Res. Commun.* **370**, 104–108 (2008).

130. Rao, S. S. *et al.* Peptides panned from a phage-displayed random peptide library are useful for the detection of *Bacillus anthracis* surrogates *B. cereus* 4342 and *B. anthracis* Sterne. *Biochem. Biophys. Res. Commun.* **395**, 93–98 (2010).
131. Carnazza, S., Foti, C., Giofrè, G., Felici, F. & Guglielmino, S. Specific and selective probes for *Pseudomonas aeruginosa* from phage-displayed random peptide libraries. *Biosens. Bioelectron.* **23**, 1137–1144 (2008).
132. Agrawal, S., Kulabhusan, P. K., Joshi, M., Bodas, D. & Paknikar, K. M. A high affinity phage-displayed peptide as a recognition probe for the detection of *Salmonella* Typhimurium. *J. Biotechnol.* **231**, 40–45 (2016).
133. Liu, P., Han, L., Wang, F., Petrenko, V. A. & Liu, A. Gold nanoprobe functionalized with specific fusion protein selection from phage display and its application in rapid, selective and sensitive colorimetric biosensing of *Staphylococcus aureus*. *Biosens. Bioelectron.* **82**, 195–203 (2016).
134. Rao, S. S., Mohan, K. V. K., Gao, Y. & Atreya, C. D. Identification and evaluation of a novel peptide binding to the cell surface of *Staphylococcus aureus*. *Microbiol. Res.* **168**, 106–112 (2013).
135. Shen, Y., Maupetit, J., Derreumaux, P. & Tuffery, P. Improved PEP-FOLD Approach for Peptide and Miniprotein Structure Prediction. *J. Chem. Theory Comput.* **10**, 4745–4758 (2014).
136. Zeng, X., Xu, G., Gao, Y. & An, Y. Surface wettability of (3-Aminopropyl)triethoxysilane self-assembled Monolayers. *J. Phys. Chem. B* **115**, 450–454 (2011).
137. Cebrián, G., Condón, S. & Mañas, P. Physiology of the Inactivation of Vegetative Bacteria by Thermal Treatments: Mode of Action, Influence of Environmental Factors and Inactivation Kinetics. *Foods* **6**, 107 (2017).
138. Mackey, B. M. Changes in antibiotic sensitivity and cell surface hydrophobicity in *Escherichia coli* injured by heating, freezing, drying or gamma radiation. *FEMS Microbiol. Lett.* **20**, 395–399 (1983).
139. Tsuchido, T., Katsui, N., Takeuchi, A., Takano, M. & Shibasaki, I. Destruction of the outer membrane permeability barrier of *Escherichia coli* by heat treatment. *Appl. Environ. Microbiol.* **50**, 298–303 (1985).
140. Kramer, B. & Thielmann, J. Monitoring the live to dead transition of bacteria during thermal stress by a multi-method approach. *J. Microbiol. Methods* **123**, 24–30 (2016).
141. Marcén, M., Ruiz, V., Serrano, M. J., Condón, S. & Mañas, P. Oxidative stress in *E. coli* cells upon exposure to heat treatments. *Int. J. Food Microbiol.* **241**, 198–205 (2017).
142. Cras, J. J., Rowe-Taitt, C. A., Nivens, D. A. & Ligler, F. S. Comparison of chemical cleaning methods of glass in preparation for silanization. *Biosens. Bioelectron.* **14**, 683–688 (1999).
143. Ebner, A., Hinterdorfer, P. & Gruber, H. J. Comparison of different aminofunctionalization strategies for attachment of single antibodies to AFM cantilevers. *Ultramicroscopy* **107**, 922–927 (2007).

144. Gopinath, S. C. B. *et al.* Surface functionalization chemistries on highly sensitive silica-based sensor chips. *Analyst* **137**, 3520 (2012).

APPENDIX A

The bacteria strains: *E. coli* C3000, *E. coli* O157:H7, *B. Thailandensis* as well as the MS2 bacteriophages used in the experiments were obtained from the INRS-Institute Armand-Frappier Research Center.

E. coli ER2738 and M13 phages were part of Phage Display Peptide Library Kit (New England BioLabs Inc.)

Peptide aptamers were selected at Ludwik Hirszweld Institute of Immunology and Experimental Therapy, Polish Academy of Science in Wrocław under supervision of dr. Ewa Brzozowska. The sequencing of the chosen peptides was performed by the Genomed company. The synthesis of the chosen peptides was performed by the Bio Basic Inc.

Preparation of the bioreceptors

AMPLIFICATION AND QUANTIFICATION OF THE MS2 BACTERIOPHAGES

Amplification of the MS2 phage was performed by adding 10 mL of LB Broth (Lennox) (LB), 300 µl of strain C3000, and 300 µl of MS2 phage stock. Amplifications were incubated aerobically with shaking overnight at 37°C. Next, lysates were centrifuged for 3 minutes at 8500 rpm, filtered (through a 0.22 µm Millipore HAWP filter), and stored at 4°C. Plaque assays were used to quantify the stock solutions as described below. Amplifications were repeated until phage titers reach 10⁸ plaque-forming units (PFU)/mL.

The phages were prepared and quantified by the double-agar layer method of a plaque assay. *E. coli* C3000 bacteria were grown in LB media until the optical density (OD)₆₀₀ = 0.5. The LB media for the top and bottom layers used in the plaque assays contained 0.7% and 1.5% agar, respectively. The Petri dishes with the bottom agar were pre-warmed to 37°C. The top agar was melted to a liquid state and maintained at 45°C until plating, while cells were growing. Amounts of 150 µl of bacteria strain and 150 µl of tenfold dilutions of phage solution were added to 3 mL of 0.7% overlay and mixed before plating. The inoculated overlay was then poured onto solidified 1.5% LB agar plates. The inoculated plates were incubated overnight at 37°C. The number of plaques were then observed.

Screening of the premade library consisting of linear heptapeptides expressed on the minor phage coat protein pIII of M13 bacteriophage (New England BioLabs Inc.) was performed using three rounds of affinity selection. Selection was performed by incubating 10 μ l of 10^{14} PFU phages from the library with approximately 10^8 CFU *E. coli* O157:H7 whole cells ($OD_{600} = 0.1$) in phosphate-buffered saline (PBS; 1 ml) for 60 min at room temperature with gentle agitation. Bacteria and phages were pelleted by spinning for 3 min at 14,000 rpm, and the pellet was washed 10 times with PBS–Tween 0.1% in the first round of selection, and with PBS–Tween 0.5% in subsequent rounds. Bound phages were pelleted with cells and eluted non-specifically with 1 ml of 0.2 M glycine-HCl (pH 2.2) with gentle shaking at room temperature for 5 min, followed by neutralization with 150 μ l of 1 M Tris-HCl (pH 9.0). A quantity of 100 μ l of eluted phages were used to infect 25 ml of exponentially growing ER2738 *E. coli* host cells for 4.5 h with vigorous shaking at 37°C. After infection, 25 μ l of chloroform was added and mixed for 2 min by vigorous shaking. Next, the culture was transferred to a centrifuge tube and spun for 10 min at 12,000 x g at 4°C. The supernatant was transferred to a fresh tube and re-spun. The phages were concentrated by precipitation with 20% PEG 8000/2.5 M NaCl and resuspended in 1 ml of PBS. Phage preparation and further panning were repeated as previously described.

Between each panning round the M13 phages were quantified by the Blue-White screening procedure. The ER2738 *E. coli* host was inoculated in LB media and incubated till mid-log phase ($OD_{600} = 0.5$). Meanwhile, the Top Agar was melted and dispensed into sterile culture tubes, which were maintained at 45°C. One hour before plating the LB/IPTG/Xgal plates were pre-warmed at 37°C. Next, 200 μ l of bacteria strain and 200 μ l of tenfold dilutions of phage solution were added to 3 mL of 0.7% overlay and mixed before plating. The infected cells were transferred into the tubes containing 45°C Top Agar. The culture was vortexed briefly and immediately poured onto a pre-warmed LB/IPTG/Xgal plate. After cooling-down, the inoculated plates were inverted and incubated overnight at 37°C. The number of plaques was then observed.

APPENDIX B

Preparations of bacteria

BACTERIA CULTURING

The following procedure has been applied to the *E. coli* O157:H7 strain.

Frozen stock was seeded at LB media overnight. Next, 2.0 ml of the sample from overnight culture was heated to 100°C for 15 minutes. Heat-killed bacteria were then pelletized at 10,000 rpm for 5 min, followed by washing in PBS buffer.

Procedure described below has been applied to the other strains of bacteria.

In order to obtain appropriate bacteria dilution, frozen stock of appropriate strain was seeded at LB media overnight at first. Then bacteria were collected by centrifuging at 10,000 rpm for 5 min, followed by washing in PBS buffer.

BACTERIA QUANTIFICATION

100 µl of the tenfold dilutions of the overnight culture (procedure 3.5.1) were plated on the LB agar to determine the titer, expressed in CFU. The dilutions appropriate for the measurements were made in the PBS buffer from prepared bacterial stock.

APPENDIX C

Functionalization of the μ IMZI surface

In the first step of the functionalization of the surface, the cavity was cleaned with a mixture of hydrochloric acid and methanol (1:1, v/v) (Sigma-Aldrich) for 30 minutes and then in sulfuric acid (Sigma-Aldrich) (30 minutes) to remove contaminations and to enhance the density of superficial hydroxyl groups (Si-OH)¹⁴². This step was completed by extensive rinsing with water and vacuum drying. In the next step, the silanization process was carried out from the (3-Aminopropyl) triethoxysilane (APTES) (Sigma-Aldrich) gas phase according to the modified procedure presented in¹⁴³. The effectiveness of the process was controlled by the exposure time or the amount of the precursor. The silanization was performed in a small vacuum desiccator filled with argon. Two trays of an amount of 30 μ l of APTES and 10 μ l of triethylamine (Sigma-Aldrich) (a sol-gel process catalyst) were placed in the desiccator chamber. The trays were left inside for 30 minutes, or for 2 hours in case of MS2/E. coli C3000 experiment, and peptide aptamers/E. coli O157:H7 experiment respectively. The vials were then removed and the cavity was kept in an argon atmosphere for 48 hours for curing¹⁴⁴. Next, the deposited amine groups were activated by the homo-bifunctional cross-linking agent glutaraldehyde (GLU) (Sigma-Aldrich) through immersion in 2.5% GLU solution in PBS for 30 minutes. The obtained surface was very sensitive to amine groups at the capsid of the bacteriophages or peptide's amine group. For the conjugation, the sensor was incubated in a bioreceptor (aptamers/phages) solution for 1 hour. It was followed by immersion in 2 mg/mL BSA solution in PBS (for MS2 phages), or in 2.5% Glycine (GLY) (pH = 9.2) (for peptide aptamers) for 30 minutes in order to block the non-specific interactions. In the last step, the sensor was exposed to the bacteria for 30 minutes.

AUTHOR'S RELATED PUBLICATIONS

Publications

1. **M. Janik**, M. Koba, A. Celebańska, W. J. Bock and M. Śmietana, "Label-free detection of live *E. coli* bacteria using a microcavity in-line Mach-Zehnder interferometer." *Scientific Reports* 8, 17176 (2018) IF: 4,847 – first author
2. **M. Janik**, M. Koba, A. Celebańska, W. J. Bock and M. Śmietana, "Sensing properties of micro-cavity in-line Mach-Zehnder interferometer enhanced by reactive ion etching." *Journal of Optics and Laser Technology*, 103, 260-266 (2018) IF: 3.671 – first author
3. M. Śmietana, **M. Janik**, M. Koba, and W. J. Bock, "Transition between bulk and surface refractive index sensitivity of micro-cavity in-line Mach-Zehnder interferometer induced by thin film deposition," *Opt. Express* 25, 26118-26123 (2017) IF: 3.307 – corresponding author
4. **M. Janik**, A. K. Myśliwiec, M. Koba, A. Celebańska, W. J. Bock and M. Śmietana, "Sensitivity Pattern of Femtosecond Laser Micromachined and Plasma-Processed In-Fiber Mach-Zehnder Interferometers, as Applied to Small-Scale Refractive Index Sensing," *IEEE Sens. J.* 17, 11, 3316-3322 (2017) IF: 2.512 – first author

Proceedings

1. **M. Janik**, M. Koba, W. J. Bock, and M. Śmietana, "Tuning refractive index sensing properties of micro-cavity in-line Mach-Zehnder interferometer with plasma etching," *Proc. SPIE* 10323, 25th International Conference on Optical Fiber Sensors, 103238M (23 April 2017) – first author
2. **M. Janik**, M. Koba, W. J. Bock, M. Śmietana, "Influence of the size of a micro-cavity fabricated in an optical fiber using the femtosecond laser in a form of in-line Mach-Zehnder interferometer on its refractive index sensitivity," *Proc. SPIE* 10175, Electron Technology Conference 2016, 101750P (22 December 2016) – first author
3. A. K. Debowska, M. Dominik, M. Koba, **M. Janik**, W. Bock, M. Śmietana, "Effect of oxygen plasma modification on refractive index sensing with micro-cavity in-line Mach-Zehnder interferometer," *Proc. SPIE* 10175, Electron Technology Conference 2016, 101750N (22 December 2016);